

PROBE EFFECTS DURING CONCENTRATION DETERMINATION IN SCANNING
ELECTROCHEMICAL MICROSCOPY

By

Alex Mirabal

A DISSERTATION

Submitted to
Michigan State University
in partial fulfillment of the requirements
for the degree of

Chemical Engineering – Doctor of Philosophy

2022

ABSTRACT

PROBE EFFECTS DURING CONCENTRATION DETERMINATION IN SCANNING
ELECTROCHEMICAL MICROSCOPY

By

Alex Mirabal

Efficient, sustainable chemical reactions will play a large role in addressing many growing issues, including alternative energy production, greenhouse gas conversion, and pharmaceuticals. Electrochemical reactions are attractive due to their relatively mild reaction conditions and direct use of electricity. The understanding and design of the local liquid-solid interface will guide future progress in electrocatalytic reactions.

Nature has evolved many highly efficient enzymatic reactions. These long-studied catalysts provide complex reaction environments that: 1) enhance interaction with reactants, 2) protect intermediates from side reactions, 3) increase the rates of reactions, and 4) selectively react to a specific product. The overarching lesson to be learned is that the local reaction environment plays a large role in the catalyst's reactivity, selectivity, and efficiency. One way to characterize the local environment is through scanning electrochemical microscopy (SECM), in which a small electrochemical probe is rastered over an interface. A quantitative correlation of the probe response to concentration provides a direct measurement of the local environment.

The presence of the SECM probe itself can induce changes in the local environment. Comparing the changed local environment (*in situ*) to what it would be without the probe present (*operando*), shows large differences of up to 120% under specific operating conditions. A few physical parameters such as the surface site geometry are shown to have an impact on how significant the probe effects are. Additional parameters such as the tip geometry and tip-surface separation are also to have an impact.

A finite element method (FEM) simulation informed by experiments is used to examine the above-mentioned tip effects. Fitting responses to other frequently used electrochemical measurements, such as approach curves and CVs, to parameterize the model appropriately describes experimental SECM results. We first apply this method to study platinum nanoparticles, where a ~50 nm resolution is the highest resolution to our knowledge for AFM-SECM. Through statistical analysis of the surface, an isolated nanoparticle SECM response is correlated with a concentration profile. It is found that the concentration profile has minimal probe effects due to the use of a conical electrode.

Applying a similar approach, we study the probe effects in pH detection during hydrogen evolution and CO₂ reduction. We match experimental results to parameterize the system. It's shown that the pH increases up to ~7 pH units beneath the probe due to hindered diffusion. Even with these large differences, the probes are still able to reflect the trends seen without the probe present. Moreover, it is shown that the physical parameters have correlated responses, indicating that hindered diffusion is controlled by the insulation radius and tip-surface separation.

Finally, the importance of the analyte is discussed regarding its interaction with the tip. In addition to the concentration impact on the response signal, the compatibility with the tip need be considered. Degradation of the tip and/or the redox couple will detrimentally affect the ability to examine the local interface. We show that, of the redox couples examined, ferrocene-based compounds appear to best satisfy the crucial factors of stability and mild redox potentials.

Overall, this work studies and removes the impact of the probe for local concentration detection using SECM. This work acts as a guide to quantitatively study the local environment of electrocatalyzed reactions. This is realized through a combined experimental-FEM approach where an informed simulation is representative of the experimental environment.

Copyright by
ALEX MIRABAL
2022

ACKNOWLEDGMENTS

I want to thank my advisor, Dr. Scott Calabrese Barton, for his guidance and encouragement throughout my Ph.D. journey. He has encouraged creativity and curiosity. He led by example with passion and consistent pursuit of exemplary research by striving to interpret results at a fundamental concept level. His guidance in writing and presenting will undoubtedly continue to help me improve as I continue moving forward. Our similar passion for alternative sustainable chemistry has been a common passion for my entire time here. I cannot thank him enough for his encouragement in mentoring and volunteering younger engineers/future engineers.

I thank all my Ph.D. committee members, Dr. Greg Swain, Dr. Lawrence T. Drzal, and Dr. Robert Ofoli who provided me their invaluable feedback and constant encouragement throughout my entire time in graduate school. I am extremely grateful for the funding support from Army research office MURI (#W911NF1410263) via Dr. Shelly Minter at the University of Utah. I am thankful to our collaborators, Dr. Mariana Monteiro, Dr. Marc Koper, Dr. Leon Jacobse, and Dr. Katharina Doblhoff-Dier from Leiden university. Their frequent exchange of ideas helped shape my research and open new opportunities for growth and passion.

I express my sincere thanks to all of my groupmates, current and past— Kanchan, Manali, Yan, Mindy, Jim, Christina, Brandon, Yunlu, Yuanchao, and Erica, and all the members of the Chemical Engineering and Material Science department at Michigan State University. To the undergraduate research assistants who have helped me grow as much as I hoped to have helped them, I thank you — Carolina, Nick, Beryl, and Fiona.

I could not have accomplished this without my ChEMS friends— Hongkang, Sabyasachi, Natalia, David, Neda, Iman, Chauncey, Lexi, Mary, and many more. I'm very thankful and lucky to have amazing friends who kept me sane (ish) during my time at MSU.

Most importantly, I would like to thank my family and friends back home who have supported me from afar and helped make me into the person I am today. Their countless words of encouragement and empathy as well as their willingness to share in their joys have truly meant the world to me. I would not have accomplished this without you, thank you for everything!

TABLE OF CONTENTS

LIST OF TABLES	x
LIST OF FIGURES	xi
Chapter 1 INTRODUCTION.....	1
1.1 Local Electrochemical Measurements	1
1.2 Experimental concentration quantification	3
1.2.1 Optical Microscopy Concentration Measurements.....	5
1.2.2 Electrochemical Concentration Measurements.....	6
1.3 Scanning Electrochemical Microscopy	9
1.3.1 Continuum Modeling	18
1.3.1.1 Probe Effects	20
1.4 Catalyst Cascades	21
1.4.1 Natural Substrate Channeling Mechanisms in Catalyst Cascades	22
1.4.2 Recent Developments	23
1.5 Carbon Dioxide Reduction	24
1.5.1 Recent Developments	29
1.5.2 Probe Effects	32
1.6 Redox Couples	33
1.7 Overview of work	37
Chapter 2 Numerical Correction of In Situ AFM-SECM Measurements [†]	39
2.1 Introduction.....	39
2.2 Experimental	41
2.2.1 Materials	41
2.2.2 SECM.....	41
2.2.3 SEM	42
2.2.4 Finite Element Model	42
2.2.5 Analytical Approach Curve Expressions	45
2.2.6 Non-Linear Regression	46
2.2.7 Calculation of Concentration Profiles.....	47
2.2.8 3D Nanoparticle Surface Response	47
2.2.9 Particle Distribution	48
2.3 Results.....	49
2.3.1 Parameter Estimation	49
2.3.2 SECM Concentration Profile Correlation	53

2.3.3 Concentration Profile Distortions	57
2.3.4 Kinetically limited tip in situ vs. operando response.....	61
2.4 Conclusions.....	65
Chapter 3 Tip Effects in pH Probe Measurements During CO ₂ Reduction [‡]	66
3.1 Introduction.....	66
3.2 Methods	68
3.2.1 Finite Element Method (FEM) simulation.....	68
3.3 Results.....	71
3.3.1 pH Sensor Synthesis and Calibration.....	71
3.3.2 Finite Element Simulations.....	75
3.3.2.1 Hydrogen evolution reaction kinetics	75
3.3.2.2 CO ₂ reduction reaction kinetics:	79
3.3.2.3 Finite Element Method (FEM) simulations	81
3.4 Conclusions.....	85
Chapter 4 Tip Effects in pH Probe Measurements During CO ₂ Reduction.....	87
4.1 Introduction:.....	87
4.2 Experimental.....	88
4.2.1 Finite Element Method (FEM) simulations	88
4.3 Results and Discussion:	89
4.4 Conclusions:.....	100
Chapter 5 Redox Couples in Aqueous AFM-SECM	101
5.1 Introduction.....	101
5.2 Experimental	102
5.2.1 Materials	102
5.2.2 Cyclic voltammetry.....	103
5.2.3 SECM.....	103
5.2.4 SECM Probe Cleaning	103
5.2.4.1 Plasma Cleaning.....	103
5.2.4.2 Warm Water	103
5.3 Results and Discussion:	104
5.3.1 AFM-SECM.....	104
5.3.2 RDE CV decay studies.....	104
5.3.3 Cleaning of AFM-SECM electrodes.....	107
5.4 Conclusions.....	108
Chapter 6 Conclusions and Future Directions	109

BIBLIOGRAPHY	114
--------------------	-----

LIST OF TABLES

Table 1-1: Aqueous analytical techniques for concentration determination at small spatial resolutions.	4
Table 1-2: Electrochemical CO ₂ reduction and hydrogen evolution reactions and their formal potentials. [239]	26
Table 1-3: Aqueous Redox couples used in SECM within a range of 0-0.8 V vs. NHE (pH = 7). Adapted with permission from [299].	35
Table 2-1: Geometric AFM-SECM tip parameters.	43
Table 2-2: Fit parameters using simultaneous fitting of positive and negative feedback approach curves.	52
Table 3-1: Geometric parameters.....	68
Table 3-2: Kinetic parameters estimated by fit to the Tafel plot (Figure 3-5), the cyclic voltammogram (Figure 3-4), or the pH-V relation (see Figure 3-9a). Values that were fixed and not fitted are marked with a star (*).	77
Table 3-3: FEM system parameters. Values for proton reduction and water reduction are given in Table 3-2.	80
Table 5-1: Redox couple comparison in aqueous solutions.....	106

LIST OF FIGURES

Figure 1-1: Concentration profiles surrounding active sites for varied k/D values. Reprinted with permission from Wheeldon et al.: Nature Chemistry [37].	3
Figure 1-2: Physical confinement effect on local pH. (a) SEM image of a Cu gas diffusion electrode. (b) High-resolution SEM image of a Cu gas diffusion electrode with an overlay of the Cu EDS signal (red shading). (c) Measured pH as a function of average trench width. (d, e) pH maps obtained from two representative at 8 μm below the electrode surface. Reprinted with permission from [38].	5
Figure 1-3: SECM Modes: A) Generation Consumption, B) Feedback, C) Hindered Diffusion, and D) Hemispherical Diffusion. Adapted from [75].	9
Figure 1-4: SECM tip geometry for pseudo-cone and planar tip electrodes and correlation to particle radius. Cone geometry has a hemispherical apex.	9
Figure 1-5: Hybrid SECM techniques for surface tracking using AFM [102] (a), shear-force [115] (b), and tape-stripping [125] (c).	12
Figure 1-6: Positive approach curve feedback responses as a function of the surface kinetics, with the standard rate constant k_0 and overpotential η for $RG \leq 2$ Adapted with permission from [73].	12
Figure 1-7: Simulated approach curves in feedback mode for varied RG values (1.5, 5, 10, and 1000) on a planar electrode. Reprinted with permission from [148].	14
Figure 1-8: Normalized current (I) vs tip-surface separation (L). Tip geometry effects on approach curve responses over conductive (A) and insulating (B) surfaces. $\kappa = H\text{tip}/a$ Reprinted with permission from Elsevier. [149].	15
Figure 1-9: Effect of tip-surface separation over gold mesh electrode imaged with a $\text{Ru}(\text{NH}_3)_6$ redox couple. Reproduced with permission. [158]	15
Figure 1-10: Constant separation tip trajectories for varied tip geometries with a base radius $1/2$ the radius of the hemispherical nanoparticle. Adapted with permission from [325].	16
Figure 1-11: Interaction of tip side with a nanoparticle. Adapted with permission from [325].	16
Figure 1-12: Multi-step reaction synthetic schemes: multi-pot synthesis, where individual reactions take place in separate reactors; one-pot synthesis, where all reactions take place in a single reactor; and cascade channeling where the intermediate transport is guided from one active site to the sequential active site. [189]	22
Figure 1-13: Keeling Curve showing CO_2 atmospheric concentration over time. Reproduced with permission from [238].	24

Figure 1-14: Potential CO ₂ carbon cycle schematic. [239].....	25
Figure 1-15: Faradaic selectivity of the gaseous products after 10 min of bulk electrolysis at a constant potential of 0.95 V vs. RHE. Insets include the SEM images of the surface after reaction. Adapted with permission [264]......	27
Figure 1-16: Periodic table depicting the primary reduction products in CO ₂ -saturated aqueous electrolytes on various electrodes based on data from Hori et al. [245] Reprinted with permission from [268]	28
Figure 1-17: Overview of presented work. a) Tip effects during concentration measurements over a single nanoparticle, b) tip effects during CO ₂ R pH measurements,	37
Figure 2-1: Bruker AFM-SECM Tip Dimensions. Insulating surfaces are indicated in solid purple, and electroactive surfaces in solid grey.	43
Figure 2-2: Experimental averaged approach curve responses (red dots) for (a) positive feedback over a gold macro electrode and (b) negative feedback over PTFE. Analytical approximations (dashed lines) were used for initial parameterization of the inverse solution (blue line). Shaded regions represent 1 standard deviation. The tip electrode was held at 0.3 V vs. AgQRE. The surface electrode in (a) was held at 0 V AgQRE, while held at open circuit in (b)......	49
Figure 2-3: Cyclic voltammetric bulk responses of the AFM-SECM Pt tip in 1 mM FcMeOH. Cyclic Voltammograms were acquired at 20 mV/s before (blue) and after (orange) AFM-SECM imaging of a HOPG surface with Pt nanoparticles.	50
Figure 2-4: SEM of AFM-SECM tip before (a) and after (b) SECM imaging of Pt nanoparticle surface. This is compared to before (c) and after (d) SECM imaging of Pt nanoparticle surface with exclusively KCl electrolyte (no redox species is present).	51
Figure 2-5: a) AFM liquid PeakForce tapping image of Pt nanoparticles deposited on HOPG in an aqueous solution. b) Experimental positive feedback SECM and overlaid AFM images of Pt nanoparticles on HOPG. (2mM FcMeOH, 0.1 M KCl) Topographical outlines of Pt nanoparticles are illustrated in white with the SECM tip current depicted by color. The tip and surface electrodes were held at 0.0 and 0.3 V vs. AgQRE respectively. Cutline current used in Fig. 2-6a is depicted by a white dashed line.....	53
Figure 2-6: Watershed analysis nanoparticle identification of AFM image, Fig. 2-5a. Boxed nanoparticle is the nanoparticle for analysis in Fig. 2-7. Numbered nanoparticles 1 and 2 are analyzed for separation from the particle of choice.	54
Figure 2-7: Nanoparticle size distribution from watershed analysis of AFM image, Fig. 5a.....	55
Figure 2-8: a) Experimental (blue) and FEM (Red & Green) SECM scan response over 75 nm Pt nanoparticle at 50 nm separation. b) In situ (solid) CO concentration profiles 25 nm from the tip apex (dot-dashed), and operando CO concentration profiles (dashed) over the 75 nm nanoparticle, represented by the black dotted hemisphere. The dot-dashed lines represent the concentration 25 nm (Rapex) below the apex of the tip electrode. Red curves represent	

simulations under kinetic limitations (KL), while green curves represent mass-transfer limited conditions (MTL) at both electrodes..... 55

Figure 2-9: In situ C₂O concentration profile distribution due to the presence of the tip for cone (a) and disk (c) shaped tip electrodes in comparison to operando case with tip absent (b). Electrode active areas are indicated by blue shading, while grey shading indicates zero-flux insulated surfaces. 58

Figure 2-10: Maximum percent difference in C₂O concentration, (in situ – operando)/operando, for a cone electrode at L=1 over a planar surface electrode, for varying electrode radius ratio and cone aspect ratio, κ , at mass transfer limited conditions. Grey dotted lines represent unity for each axis. The light grey dotted line indicates $aR_{surf} = 12$, used in Fig. 2-7..... 59

Figure 2-11: *In situ* (solid) vs. *operando* (dashed) CO concentration profile comparison for conical, disk, and hemispherical electrodes over mesh, nanoparticle, and planar surfaces (a-l). Responses were compared at normalized separations of L= 1, 2, and 4, represented by blue, green and red respectively. The *in situ* response is calculated from the tip flux. The tip trajectory and surface topography are depicted in the bottom row (m-p) for each surface site and tip geometry. The active region of the surface is highlighted in bold. Tip and surface electrode fluxes are mass transfer limited. 59

Figure 2-12: *In situ* (solid) vs. *operando* (dashed) CO concentration profile comparison for conical (a-d), hemispherical (e-h), and disk (i-l) electrodes over mesh, nanoparticle, and planar surfaces that are kinetically limited. The *in situ* response is calculated from the tip flux. The tip trajectory and surface topography are depicted in the bottom row (m-p) for each surface site and tip geometry. The active region of the surface is highlighted in bold. 60

Figure 2-13: Enlarged subset of fig. 2-11l (inset) *In situ* (solid) CO concentration profile comparison for a disk electrode over a planar surface under mass transfer limited conditions. .. 61

Figure 3-1: Geometric description of the experimental system with simulation boundary conditions used for hydrogen evolution and CO₂ reduction..... 68

Figure 3-2: SECM pH sensor synthesis and calibration. (a) Voltammogram of the functionalized Au-UME showing the conversion of 4-nitrothiophenol (4-NTP) to the pH sensitive redox couple 4-hydroxylaminothiophenol (4-HATP)/4-nitrosothiophenol(4-NTP); (b) pH sensor voltammetry in 0.1 M Li₂SO₄ solutions adjusted to different pH, taken at 200 mV s⁻¹; (c) Calibration curves of the modified Au-UME pH sensor in different gaseous atmospheres. The calibration curves from our collaborator's previous work [305] are also shown for comparison. 71

Figure 3-3: Chronoamperometric surface electrode (gold) current over 100s as a function of the surface electrode potential under argon (a) and CO₂ (b) gas sparging in 0.1 M Li₂SO₄. The applied surface potential is stepwise controlled as a function of time (grey dotted line). The corresponding peak potentials at the tip pH electrode follow (c-d)..... 73

Figure 3-4: 100 mV/s cyclic voltammogram on the gold surface electrode under argon saturation in 0.1 M Li₂SO₄. Experimental results (black) are compared to FEM simulation results (blue)

with the proton reduction rate constant fit to the 3rd cycle (blue line) with a 95% confidence interval. 75

Figure 3-5: Tafel slope for HER at pH 3 extracted from the chronoamperometry (Fig3-2a) experiment using the 4 lowest overpotential values. 76

Figure 3-6: Calculated contributions of the local chronoamperometric current density at the gold electrode and beneath the SECM tip ($x=0 \rightarrow a$), due to proton (blue) and water (red) reduction. Current density is calculated from average flux of each species over 25 μm (a) from the center of the surface electrode, which is below the SECM tip electrode..... 78

Figure 3-7: pH profile near the electrode surface during HER a) with and b) without the SECM tip present. Sample potential applied -0.8 V vs. Ag/AgCl in 0.1 M Li_2SO_4 82

Figure 3-8: H^+ (solid) and OH^- (dashed) vertical concentration profiles during HER under argon saturation as the boundary layer approaches the tip position (dotted grey line). Surface electrode potentials of -0.850 V (blue) and -0.8625 V (red) vs. Ag/AgCl demonstrate growth of the boundary layer beyond the position of the tip electrode..... 83

Figure 3-9: Effect of the probe on the local pH response under a) argon and b) CO_2 as a function of the surface potential. pH–potential comparisons of experimental results in argon (black dots) and FEM simulation results (blue line) for $L=3.4$ (close to the surface), compared to the pH at $z/a=3.4$ when the tip is far from the surface ($L = 50$, blue dashed line). The simulated pH ‘without tip’ is obtained from a cross section at 80 μm from the surface with the tip removed to 1.25 mm from the surface ($L = 50$); L is the normalized tip-surface separation (see Experimental Section). b) Similarly, experimental (red dots) and simulation (dark red line) pH under CO_2 reduction for $L = 3.4$, is compared to simulated $L = 50$ (dark red dashed line). Bulk CO_2 concentration was fixed at 10 mM..... 84

Figure 3-10: Minimization of tip effects by decreasing the insulation radius. Comparison is made for the experiment in argon, using the results from Figure 3-9a, and simulations decreasing the insulation radii, with a constant a . The bottom tip insulation radius is maintained at $\frac{1}{2} R_{\text{ins}}$ (see Figure 3-1 in the Experimental Section). (0.1 M Li_2SO_4 , $L=3.4$, and $R_{\text{surf}} = 5\text{mm}$). 85

Figure 4-1: Time dependent pH at the tip electrode with a surface electrode potential of -0.9 V vs. Ag|AgCl. ($a = 25 \mu\text{m}$, $L = 3.2$, $R_{\text{surf}} = 100$, $R_G = 10$, 0.1 M KHCO_3 , 32 mM CO_2)... 89

Figure 4-2: Insulation radius (R_G) impact on pH-potential relations as detected at the pH probe 80 μm from the surface. ($a = 25 \mu\text{m}$, $L = 3.2$, $R_{\text{surf}} = 100$, 0.1 M KHCO_3 , 32 mM CO_2)... 90

Figure 4-3: Vertical pH profile beneath the tip electrode at varied potentials. b) Vertical pH profile in the absence of the probe for different surface overpotentials. Grey dotted line correlates to the tip position. ($a = 25 \mu\text{m}$, $L = 3.2$, $R_{\text{surf}} = 100$, $R_G = 10$, 0.1 M KHCO_3 , 32 mM CO_2). 90

Figure 4-4: Vertical concentration profiles over the surface electrode at $E_{\text{surf}} = -0.9 \text{ V vs. Ag|AgCl}$. ($a = 25 \mu\text{m}$, $L = 3.2$, $R_{\text{surf}} = 100$, $R_G = 10$, 0.1 M KHCO_3 , 32 mM CO_2). 91

Figure 4-5: Horizontal concentration profiles at the surface electrode ($Z=0$) and at the tip electrode ($Z = L = 80\mu m$) at a potential of $-0.9V$ vs. $Ag AgCl$. ($a = 25\mu m$, $L = 3.2$, $R_{surf} = 100$, $R_G = 10$, 0.1 M KHCO_3 , 32 mM CO_2).	92
Figure 4-6: Horizontal pH profile at two different positions, at the surface electrode ($Z=0$) and at the tip electrode ($Z=L=80\mu m$). The surface electrode potential is varied vs $Ag AgCl$. The insulation radius, R_G , is indicated by the dotted line. ($a = 25\mu m$, $L = 3.2$, $R_{surf} = 100$, $R_G = 10$, 0.1 M KHCO_3 , 32 mM CO_2).	92
Figure 4-7: local pH during pulsed chronoamperometry as a function of tip-surface separation (L). ($a = 25\mu m$, $R_{surf} = 100$, $R_G = 10$, 0.1 M KHCO_3 , 32 mM CO_2 , $\nabla E = 10\text{ mV}$).	94
Figure 4-8: Potential dependent local pH as a function of the tip-surface separation (L), the insulation radius (R_G), and the surface electrode potential (E_{sub}). Varied R_G , at constant L , is differentiated by color (a) and shading/marker (b). The surface potential, indicated on the plot (-0.75 , -0.8 , and $-0.9\text{ V vs. Ag AgCl}$) are separated by color in b.	95
Figure 4-9: a) Local pH response as a function of surface electrode radius for a range of surface electrode potentials ($L = 3.2$). b) pH potential dependence at different tip-surface separation for a surface electrode radius of $R_{surf} = 2$. ($a = 25\mu m$, $L = 3.2$ (a), $R_G = 10$, 0.1 M KHCO_3 , 32 mM CO_2 , $\nabla E = 10\text{ mV}$).	96
Figure 4-10: Horizontal pH profiles for varied surface electrode radii across the surface (dashed) and at the height of the tip (solid) at -0.9 V vs Ag AgCl and $100s$. ($a = 25\mu m$, $L = 3.2$, $R_{surf} = 100$, $R_G = 10$, 0.1 M KHCO_3 , 32 mM CO_2).	97
Figure 4-11: Vertical concentration profile of four species, H^+ , CO_2 , HCO_3^- , CO_3^{2-} as a function of bulk CO_2 concentration. The surface potential is held at $-0.9\text{ V vs. Ag AgCl}$ for $100s$. ($a = 25\mu m$, $L = 3.2$, $R_{surf} = 100$, $R_G = 10$, 0.1 M KHCO_3).	98
Figure 4-12: pH profiles versus surface potential for a) varied bulk CO_2 concentration. $L=3.2$ and $R_G=10$ for the tip electrode with an electrolyte concentration of 0.1 M . The buffered electrolyte in (a) is compared to an unbuffered electrolyte from fig. 3-8 at $[CO_2] = 10\text{ mM}$. ($a = 25\mu m$, $L = 3.2$, $R_{surf} = 100$, $R_G = 10$, 0.1 M KHCO_3 (a), $\nabla E = 10\text{ mV}$).	98
Figure 4-13: Potential dependent pH response for varied electrolyte ($KHCO_3$) concentrations. $L=3.2$ and $R_G=10$ for the tip electrode with a CO_2 concentration of 32 mM . ($a = 25\mu m$, $L = 3.2$, $R_{surf} = 100$, $R_G = 10$, 32 mM CO_2 , $\nabla E = 10\text{ mV}$).	99
Figure 5-1: AFM-SECM probe before (a) and after (b) SECM measurements in $10\text{ mM Ru(NH}_3)_6$ and 0.1 M KCl	104
Figure 5-2: AFM-SECM tip CV in $10\text{ mM Ru(NH}_3)_6$ and 0.1 M KCl before and after SECM imaging.	104
Figure 5-3: 20 cycle CV on a 5 mm Pt RDE in 0.1 M KCl with $10\text{ mM Ru(NH}_3)_6$. The rotation was held at 1600 rpm	105

Figure 5-4: Redox couple decay rates from CV studies at 1600 rpm in 0.1 M KCl.....	105
Figure 5-5: CV at 50 mV/s over a Pt wire in the SECM cell comparing the initial response (black) to after use (red), and the two cleaning methods of plasma (blue) and warm water (green). (20 mV/s, 2 mM FcMeOH, 0.1 M KCl).....	107

Chapter 1

INTRODUCTION

1.1 Local Electrochemical Measurements

Electrode reactions are chemical reactions that involve the transfer of charged species across an interface.¹ These reactions directly connect to chemistry to electricity through the transfer of electrons. Electrochemical reactions are typically heterogeneous. Therefore, understanding of these reactions requires the knowledge of the location in which the reaction occurs.² It follows that these reactions are dependent on the electrode materials, solution chemical species, and the microstructure of the electrode interface.^{2–10} This is most relevantly apparent in the study of electrochemical catalysis.^{11–13} There are additional differences in properties as the size of the electrode active sites approaches the nanoscale, including melting points, and optical and electronic properties.¹⁴

Physicochemical properties have been shown to be critical in the fields of catalysis,^{13,15–21} corrosion,^{22–26} energy storage,^{3–6,27,28} sensing,^{29–35} and more.^{36,37} These properties include, but are not limited to; composition^{22–24,27}, porosity^{17,36,38}, morphology^{13,23,27}, local concentration^{17,20,21,24,25,29,33–35}, and local transport mechanisms^{18,28,36,37} and the correlation between them. The properties have been shown to not only be related to the increased surface area, but also to other tunable properties.^{12,14} It has been shown that the catalytic properties of gold, among other metals, for CO₂ reduction varies across different exposed faces.^{19,39,40} Local pH has been shown to have a larger influence on reactivity compared to the bulk value.^{21,32,38,41} Additionally, the effect of the microstructure influences the above two examples.^{3,5,41,42}

The deepened understanding of the influence of local properties on the electrochemical response has coincided with the development of techniques to isolate individual responses. The

invention of scanning tunneling microscopy (STM) by Binnig and Rohrer was instrumental in the distinction of local behavior.⁴³ Additionally, the invention of the atomic force microscopy (AFM) extended the capability to insulating surfaces.⁴⁴ Since then, these techniques and their derivatives have been used to image, and modify surfaces on the nanoscale using different force transducers, such as magnetic, thermal, electronic, and physical forces.⁴⁵ The group of techniques in which a physical probe is used is termed scanning probe microscopy (SPM). SPM is limited by the size of the probe itself and can operate under ambient conditions, both of which are attractive analytical features.^{46,47}

Another SPM technique invented by Bard and Mirkin in the late 1980's is Scanning Electrochemical Microscopy (SECM), which measures the electrochemical response at the probe.⁴⁸ Short distances achieved by SECM enhance mass transport. This allows study of systems with high kinetic rates, while not in diffusion limited conditions.⁴⁹ This technique is increasingly applied to image interfaces and correlate these images to various properties such as topography,^{50–52} reaction rate,^{53–57} pH,^{58,59} and transport.^{16,60–63} The study of complex kinetics is of particular interest. Multi-step reactions in which one/multiple intermediate/s are formed can have complex environments. Probe techniques enable the detection of these species that may only exist in significant quantities near the electrode surface.^{15–19,57,60,64–69} In this dissertation we aim to develop and apply a combined experimental and simulation approach for detection of small concentrations for quantitative analysis at the nanoscale.

1.2 Experimental concentration quantification

It is of broad interest to detect local concentration at interfaces, including during heterogeneous catalysis^{53,70,71} and transport.^{16,61,61–63,67,72} The detection of concentrations have been used to analytically study heterogeneous catalysis kinetics.^{16–19,53,56,57,64–67,69–71,73–80} The detection of species on one side of a membrane can similarly be used to measure the transport rate, such as the efflux of molecules from a cell.^{61,67,81,82}

Calculations of concentration profiles surrounding active sites in Figure 1-1 suggests that diffusion alone is not enough for an appreciable increase in the local intermediate concentration for typical enzymes ($k = 10 \text{ s}^{-1}$). For a typical system ($\frac{k}{D} = 0.01 \mu\text{m}^2$) the concentration profile is uniform, suggesting that proximity alone is not responsible for an increased kinetic response.³⁷ There have been numerous indirect ways to measure concentration, such as gas chromatography, mass spectrometry⁸³, fluorescence⁸⁴, and side product concentration.⁸⁵ Although there have yet to be direct measurements of channeled intermediates, there are several techniques that, for other systems, have been used to detect local species in solution. Local measurements techniques include infrared spectroscopy (IR)⁸⁶, Raman spectroscopy^{87–90}, electrochemical measurement^{56,57,80,91}, and fluorescence spectroscopy.^{32,92,93}

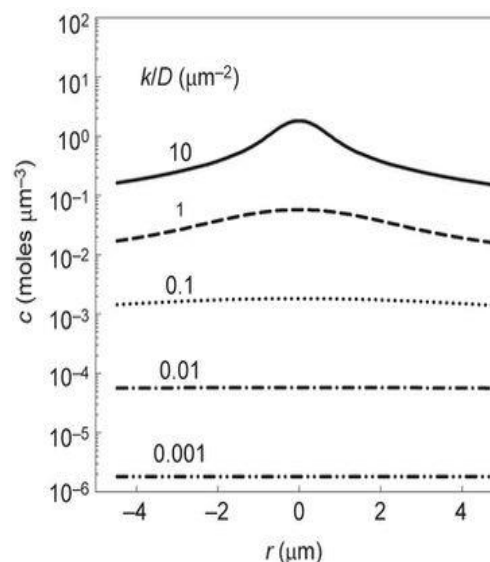


Figure 1-1: Concentration profiles surrounding active sites for varied k/D values. Reprinted with permission from Wheeldon et al.: Nature Chemistry [37]

The solid-liquid interface is difficult to interrogate by surface sensitive techniques that require particles for analysis, such as electrons, ions, and atoms. It is difficult due to the high

density of the two condensed phases.⁹⁴ As the sites of interest decrease in size, or as the desired resolution increases, the techniques become more limited, particularly for liquid systems in which the transport processes are faster than solid systems, but the solvent density often limits the resolution as compared to gas phase and vacuum systems. Optical techniques such as infrared and raman spectroscopy are limited in resolution by the spot size of the laser, $\sim 1\mu\text{m}$ and ~ 500 nm respectively. While surface or tip enhanced signaling can increase the detection limit, the spatial resolution is still a limiting factor.^{94, 94,95} Particularly, nanoscale resolution chemical concentration diagnosis at interfaces has only recently been available through techniques such as, surface enhanced raman^{87–89,96} or infrared spectroscopy.^{86,97,98} Creative design of experimental setups is required for analysis of individual or unique active sites. Aqueous environment nanoscale chemical detection has been typically limited to tip enhanced measurements^{53,87,99–103} and optical techniques.^{86–89,93,96–98} Fluorescence microscopy has developed chemical spatial resolution of ~ 20 nm⁹³, while tip enhanced Raman spectroscopy (TERS) has a spatial resolution of 20–30 nm⁹⁹, where the tip increases the resolution and signal through local plasmon resonance. Nanoelectrodes as small as 3 nm have been used experimentally in SECM.^{104,105} The above techniques are summarized in Table 1-1 and described in further detail below.

Table 1-1: Aqueous analytical techniques for concentration determination at small spatial resolutions.

TECHNIQUE	ABREV.	RESOLUTION	RESPONSE	REFERENCES
Surface enhanced Raman Spectroscopy	SERS	500 nm	Qualitative Concentration	88
Tip Enhanced Raman Spectroscopy	TERS	20 nm	Qualitative Concentration	110,87
Scanning Electrochemical Microscopy	SECM	50 nm	current	120-119
Fluorescence Microscopy	FM	20 nm	Fluorescence	93

Table 1-1 (cont'd)

Attenuated total reflectance surface enhanced infrared adsorption spectroscopy	ATR-SEIRAS	20 nm	Qualitative Concentration	110
Rotating ring-disk electrode	RRDE	Disk radius	Current	33

1.2.1 Optical Microscopy Concentration Measurements

One of the most common concentration measurements is pH monitoring. Optical techniques for monitoring the probe offers a non-invasive option for local pH monitoring. Fluorescence microscopy uses fluorophores that are sensitive to the molecule of interest. Requirement of fluorogenic species can limit substrate analysis.^{32,94} In general, the resolution is limited to ~250 nm (wavelength of greenlight). Use of a confocal laser

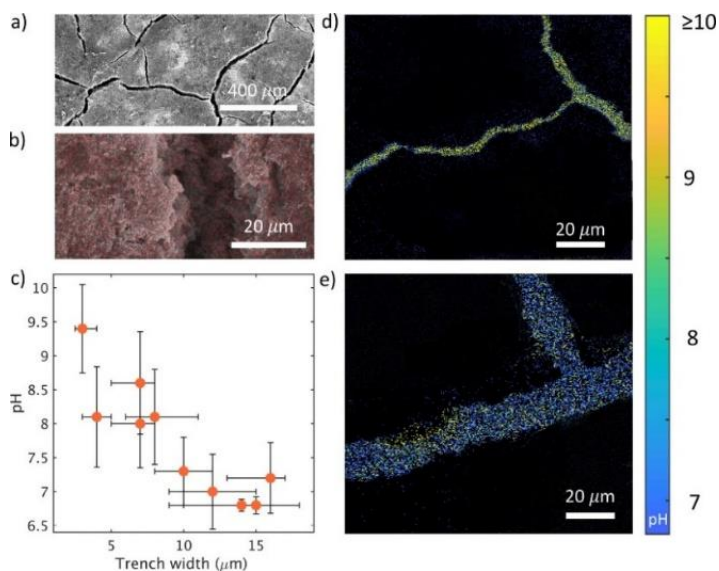


Figure 1-2: Physical confinement effect on local pH. (a) SEM image of a Cu gas diffusion electrode. (b) High-resolution SEM image of a Cu gas diffusion electrode with an overlay of the Cu EDS signal (red shading). (c) Measured pH as a function of average trench width. (d, e) pH maps obtained from two representative at 8 μm below the electrode surface. Reprinted with permission from [38]

microscopy allows for z direction mapping through different focus planes and increases the XY resolution by eliminating out-of-focus light and increases the resolution to ~20 nm.^{38,106} Figure 1-2 demonstrates the pH variance in trenches of varied width during CO₂R and the local pH change due to these varied widths³⁸. At increasingly narrow widths, it is shown that the pH increases. Additionally, the pH is found to vary vertically in relation to these trenches as well by

varying the focus depth of the confocal microscope. This enables 3D concentration mapping in relation to surface morphology.³⁸

Surface enhanced Raman Spectroscopy (SERS) is capable of analyzing biological samples including enzymes.⁸⁸ Analysis in liquids causes diffraction of the light and decreases the resolution. TERS can mitigate this through local enhancement with metal tips, however, the enhancement is lower than that of SERS. Additionally, low laser irradiation required for biological samples requires a higher enhancement than is currently available with TERS.⁸⁷ The Gewirth group has recently shown that the pH has impact on the local carbonate species concentration, and therefore the reactivity. To do this, they analyze SERS data and monitor copper carbonate. SERS, as used in previous studies¹⁰⁷, is limited to ~500 nm spot size. The different behavior of nanoparticles as compared to their bulk counterparts¹³ indicates it would therefore be advantageous to analyze the local pH using a technique with the appropriate resolution. A gold nanoelectrode (provided the sealing with the glass insulation is good) could increase the resolution beyond SERS.⁹¹ Another technique, attenuated total reflectance surface-enhanced infrared absorption spectroscopy (ATR-SEIRAS), uses infrared that penetrates the interface and measures the local pH dependent species. While the spatial resolution is limited, the use of a tip for scattered responses can increase the resolution in SEIRAS measurement to ~20 nm.¹⁰⁸ During CO_2R , HCO_3^- and CO_3^{2-} are measured and the ratio between them is related to OH^- concentration through equilibrium relations.⁶⁵ In order for penetration into solution, thin films are often required, limiting catalysts that can be analyzed to thin films.¹⁰⁹

1.2.2 Electrochemical Concentration Measurements

Scanning electrochemical microscopy (SECM) involves the electrochemical detection of species at a rastering tip. Current spatial resolution of ~50 nm is only slightly larger than a few of

the highest resolution techniques mentioned above. However, SECM studies of enzymatic systems expands its applicability beyond others that require nanometallic enhanced responses.^{78,110–115} Other scanning probe techniques and fabrications also have the potential for nanometer resolution, dependent on the tip geometry. Potentiometric probes monitor the shift in potential as it relates to the pH at the probe. The probes are typically metal or metal/oxides and have a longer (few seconds) time scale. The success rate of electrode preparation is reportedly low, however easy to use.³² Long time scales complicate pH mapping over an interface. Similarly, scanning ion-selective electrode technique (SIET) uses an ion-selective membrane in a micropipette.¹¹⁶ These probes often have a low stability range and still suffer from a longer time scale. Scanning ion conductance microscopy (SICM) uses a micropipette filled with electrolyte, which, when measured against an external reference counter electrode, generates ion conductance current to control the positioning. Using a double barrel pipette allows for simultaneous control of the positioning and pH monitoring.¹¹⁷ However, as one might expect synthesis of a nanoscale double barrel pipette electrode with a quasi-reference counter electrode is challenging.

pH monitoring with Scanning Electrochemical Microscopy (SECM) allows for spatial resolution limited by the tip dimensions. The pH probe used determines the time scale of the response. pH probes are often unstable due to the CO₂ reduction reaction environment. Noble metals, often used as potentiometric pH sensors, strongly interact with CO, potentially altering the open circuit potential.¹¹⁸ For a potentiometric response, this limits the applicability to measure pH during CO₂R.

Collection of products at the back of a gas diffusion electrode can mitigate CO contact with the electrode. Dieckenhöfer et al. used a Pt electrode operating at high current densities in

an alkaline environment to avoid CO contact with the SECM Pt tip.³⁵ The high alkalinity required for this probe only occurs during high turnover at the interface, limiting analysis to highly porous electrodes or high overpotential analysis. Monteiro et al. have recently developed a highly stable, selective and sensitive SECM pH probe based on the functionalization of gold ultramicroelectrodes (Au-UMEs) with a 4-nitrothiophenol self-assembled monolayer.⁹¹ This voltammetric pH probe provides a high temporal resolution with a stable pH response over a large pH range.

A rotating ring disk electrode (RRDE) uses two electrodes in which a central disk electrode is used to drive a reaction. A second, ring electrode surrounding the disk electrode, monitors the pH.³³ Rotation of the electrode drive convection from the bulk to the center of the RRDE. It then flows outward toward the ring electrode. In this way, the mass transport is controlled. However, this also prevents mapping of a local response, and rather provides an average response of the entire disk electrode.

As discussed above, the use of a probe can increase the spatial resolution depending on the size of the probe. The smaller the probe, the higher achievable spatial resolution. Additionally, the response, integrated over the surface of the probe, can have reduced error due to minimized averaging. However, the decreased probe size leads to a decrease electrochemical response. A response, limited by the probe and interface, must be above the relative noise and detection limit of the technique practically. To address this, often the probe is brought closer to the interface. However, the presence of the probe can alter the environment it is analyzing, particularly near the interface. Tip enhanced techniques confine local diffusion to cylindrical coordinate radial diffusion, rather than hemispherical or linear perpendicular diffusion. Correlation of experimental and *operando* results requires the removal of these tip effects.¹¹⁹

Additionally, electrochemical tips induce migration due to applied potentials that must also be considered. Consumption of the species can cause shifting concentration gradients impeding concentration correlation. Correlation of results with a continuum model is one approach for removing these tip effects.

1.3 Scanning Electrochemical Microscopy

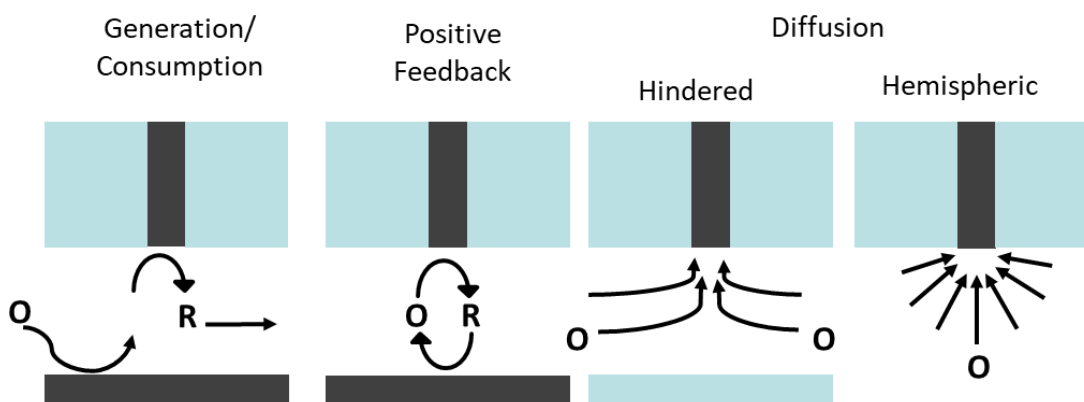


Figure 1-3: SECM Modes: A) Generation Consumption, B) Feedback, C) Hindered Diffusion, and D) Hemispherical Diffusion. Adapted from [75].

SECM is a technique that is increasingly applied to image interfaces and correlate these images to various properties such as topography,^{50–52} reaction rate,^{53–55} and pH.^{58,59} This technique involves rastering an electrode in 3 dimensions over an interface. A position-

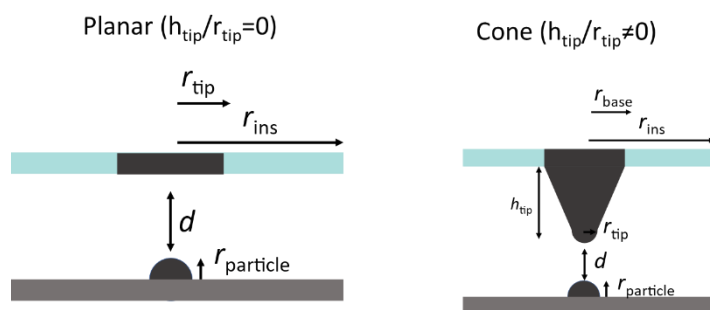


Figure 1-4: SECM tip geometry for pseudo-cone and planar tip electrodes and correlation to particle radius. Cone geometry has a hemispherical apex.

r_{tip}	Tip Radius
r_{base}	Tip Base Radius
r_{ins}	Insulation radius
r_{particle}	Particle Radius
h_{tip}	Tip Height
d	Tip-Surface Separation

dependent tip current is recorded, allowing for property mapping over an interface.^{50,55} Over the last 30 years, there have been numerous methods to control position of the tip electrode, including but not limited to tape-SECM, scanning ion conductance microscopy (SICM-SECM), Constant

height SECM, Atomic force microscopy (AFM-SECM), and shear force SECM.⁷⁵ Generally, these techniques vary by how they detect and track the surface.

SECM uses constant height while rastering over an interface. The separation is measured at a single point and the height of the probe is unvaried, regardless of the surface topography. However, subsequent add-on techniques use constant separation surface tracking through techniques such as conductance for SICM-SECM and surface interaction with AFM-SECM,^{101,119,120} shear force SECM,^{114,121} and tape stripping-SECM.¹²² For a technique in which mass transport is affected by the separation between the tip and the interface^{49,123}, a constant separation removes the vertical mass transfer effect on SECM mapping results.

The probing of interfaces provides unique conditions in which the response can be influenced by spatial separation, so called hindered diffusion.¹²⁴ Hindered diffusion is impacted by physical parameters of the probe, including geometry and probe-surface separation. In general, the physical geometry in close proximity to the probe causes behavior like a thin layer cell.⁷⁴ Diffusion into and out of this region is restricted by the presence of the probe. This causes an enhanced response in positive feedback mode due to the local regeneration of species with minimized loss to the bulk. A negative feedback response, a response solely due to hindered diffusion, has a maximum change from the bulk with a maximized amount of hindered diffusion (see Figure 1-3, Figure 1-7, and Figure 1-8).

Scanning ion conductance microscopy (SICM) tracks the surface uses ionic current to monitor the separation between the surface and a microcapillary filled with electrolyte solution.¹²⁵ Flux of the ions is dependent on the topography near the surface. A constant ionic current is therefore used to track the topography. Simultaneous topographical and electrochemical analysis of the surface requires a multifunctional electrode, either a concentric

electrode and capillary or double-barrel electrode.^{52,126} The double barrel electrode can also be adapted such that the only SECM barrel contains the analyte and the reaction only takes places where the barrel is over the surface, scanning electrochemical cell microscopy (SECCM). These electrodes often have complex synthesis procedures that have limited the resolution to 100nm that can be further reduced by wetting properties by up to ~10-20%.¹²⁷

The use of a physical surface tracking mechanism can simplify the electrode response and has a straightforward mechanism of tracking the surface, through the physical interaction of the probe with the surface (Figure 1-5). As such the topographical resolution is limited by the electrode size directly. Tape-SECM uses the dragging of a soft electrode over an interface, where the angle caused by the dragging itself maintains a constant separation for the tip electrode. The challenges with this approach include the non-perpendicular tip electrode and the need for a soft electrode.¹²² Shear force SECM uses a horizontally vibrating flexible needle that is dampened near the surface. Schuhmann et al. have shown the capability to maintain a constant separation of ~100nm over the surface.¹²⁸ However the tip-surface separation dependent measurements are dependent on the needle stiffness.¹²⁹ AFM-SECM uses the interaction force monitored by the tip deflection close to the surface to monitor the topography.¹¹¹ The increased structural information available from AFM provides a unique capability to correlate electrochemical responses with additional structural properties.¹³⁰ AFM uses a laser diode, which is reflected off the back of a flexible cantilever, which hosts the probe. As the tip interacts with the surface, the cantilever is deflected, causing the laser reflection to shift. This shift is used to monitor the interaction force between the surface and the tip.¹³¹ The type of interaction is not limited to physical interactions, has been extended to magnetic, electronic and biological interactions dependent on the tip material and operational procedures.^{131–133} The physical interaction can be minimized by

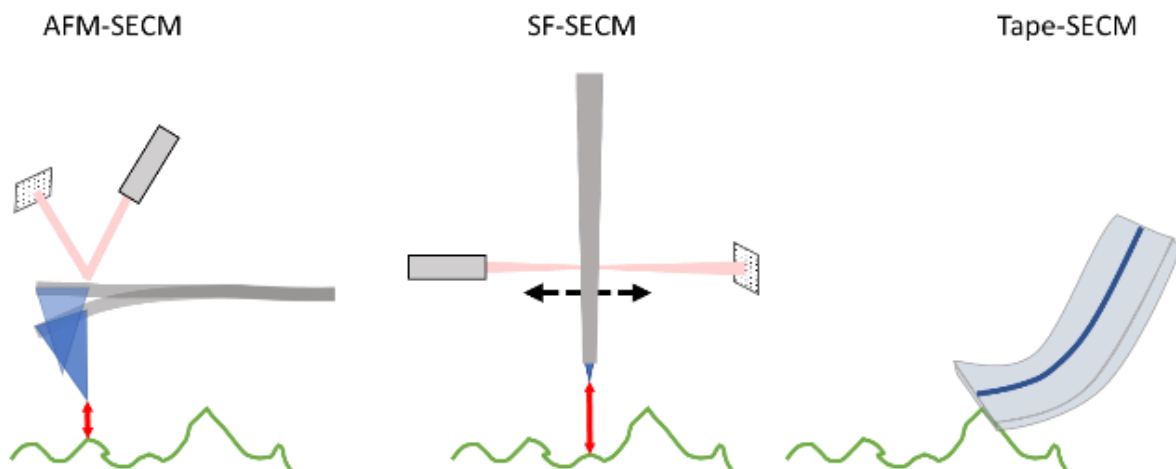


Figure 1-5: Hybrid SECM techniques for surface tracking using AFM [102] (a), shear-force [115] (b), and tape-stripping [125] (c).

periodically (at each and every position) interacting with the surface. By analyzing the force at each position, position-dependent mechanical information can be attained simultaneously to topographical mapping.¹³⁴

The increasing capability of SECM to examine nanoscale phenomena has enabled the experimental interrogation of nanoscale interfacial features,^{50,105,135,136} enabling nanoscale current mapping and local property identification.^{53,61,67,72,137–139} In order to localize SECM

response to the area of the surface feature, the SECM tip size should be equal to, or smaller than, the surface feature.¹⁴⁰ Recent advances in combined SECM techniques, such as AFM-SECM,^{141,142} in addition to nanoelectrodes and

instrumentation,^{50,52,136,138,143–145} have satisfied this requirement.

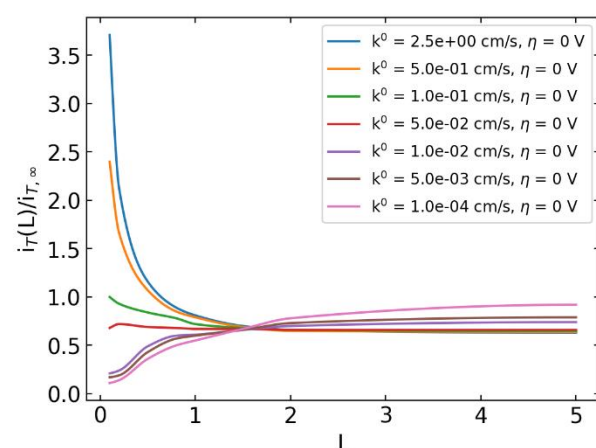


Figure 1-6: Positive approach curve feedback responses as a function of the surface kinetics, with the standard rate constant k^0 and overpotential η for $RG \leq 2$ Adapted with permission from [73].

A surface that regenerates the species analyzed at the tip generates positive feedback (Figure 1-3). These surfaces are called conductive surfaces, and insulating surfaces generate negative feedback due to lack of regeneration of analyte.^{49,146,147} For positive and negative approach curves the tip-surface separation is varied and the electrochemical response is recorded as a function of these variations.^{148,149} Analytical approximations of disk electrode approach curves yield dependence on the kinetic rate of the surface electrode (Figure 1-6).¹⁴⁰ Early equations that varied kinetic parameters as well as accounted for the tip insulation thickness^{123,148} are summarized below:

$$\frac{i_{tip}(E,L)}{i_{tip,\infty}} = \frac{k_1(RG) + \frac{k_2(RG)}{L} + k_3(RG) \exp\left[\frac{k_4(RG)}{L}\right]}{\theta + \frac{1}{\kappa}} \quad (1-1)$$

$$\frac{i_{tip}(L)}{i_{tip,\infty}} = \frac{1}{k_1(RG) + \frac{k_2(RG)}{L} + k_3(RG) \exp\left[\frac{k_4(RG)}{L}\right]} \quad (1-2)$$

Where $L = \frac{d}{r_{tip}}$, the tip-surface separation, and the constants are a function of the insulation radius, $k_{1-4} = f(RG)$. The kinetic variable

$$\kappa = \frac{k^0 \exp(-\alpha n f(E - E^{0'}))}{m_0} \quad (1-3)$$

where the mass transfer coefficient¹²³,

$$m_0 = \frac{4D_0\left(k_1(RG) + \frac{k_2(RG)}{L} + k_3(RG) \exp\left[\frac{k_4(RG)}{L}\right]\right)}{\pi r_{tip}} \quad (1-4)$$

and⁷³

$$\theta = 1 + \exp(\eta f(E - E^{0'})) \frac{D_O}{D_R} \quad (1-5)$$

Hindered diffusion causes a deviation from bulk response at larger separations due to the electrochemical reactant source diffusion scale due to insulation. The critical length of the system is defined as the radius of the tip electrode, r_{tip} . The insulation radius is often normalized by the radius of the tip electrode, $RG = \frac{r_{ins}}{r_{tip}}$ (Figure 1-4).

The use of a planar disk electrode in Figure 1-7 shows an increased effect of hindered diffusion as the insulation radius increases. The positive feedback response is minimally affected as most of the current is due to feedback from the surface electrode. Additionally, the positive feedback response is detected as far as 4 critical lengths (tip radii) away. When the surface electrode reaction is turned off, the negative feedback shows significant dependence on RG , where an increasing RG

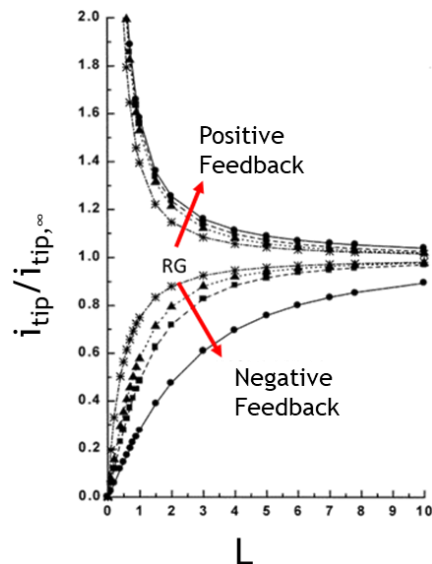


Figure 1-7: Simulated approach curves in feedback mode for varied RG values (1.5, 5, 10, and 1000) on a planar electrode. Reprinted with permission from [148].

increases hindered diffusion. Hindered diffusion can be partially mitigated with a cone electrode. In Figure 1-8, Mirkin et al. used varying aspect ratio conical electrodes to demonstrate a decreased positive and negative feedback response as the aspect ratio increased.¹⁴⁹ Additionally, the kinetic rate at the surface largely controls the extent to which feedback responses occur.

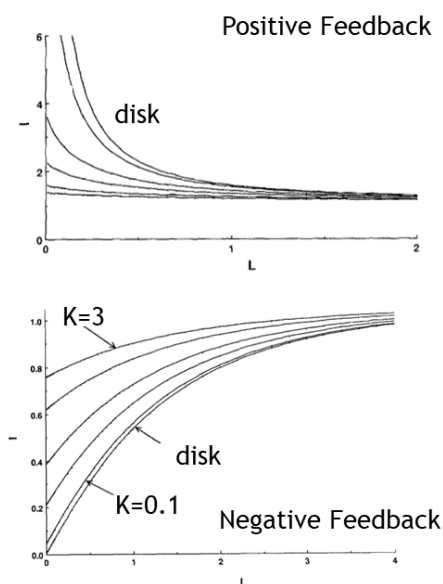


Figure 1-8: Normalized current (I) vs tip-surface separation (L). Tip geometry effects on approach curve responses over conductive (A) and insulating (B) surfaces. $\kappa = H_{tip}/a$ Reprinted with permission from Elsevier. [149]

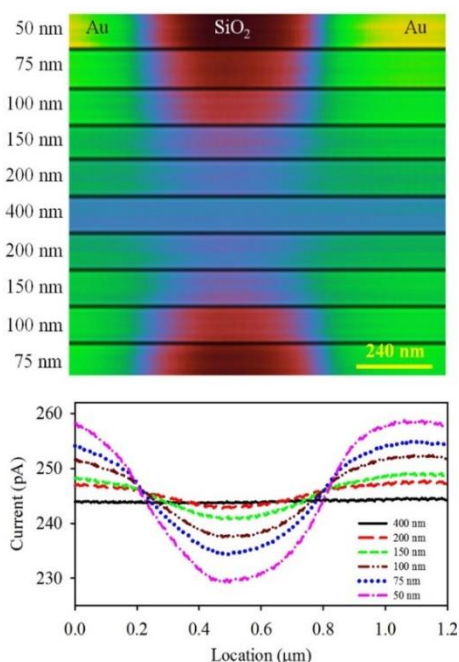


Figure 1-9: Effect of tip-surface separation over gold mesh electrode imaged with a $\text{Ru}(\text{NH}_3)_6$ redox couple. Reproduced with permission. [158]

Mirkin et al. varied the surface kinetics from irreversible to completely reversible by varying the Damköhler number, $D_a = \frac{\kappa a}{D}$ in Figure 1-6. Irreversible kinetics resemble negative feedback responses, where the species is likely to diffuse away before it can react at the surface. At high kinetic rates, the reaction is largely reversible, and the positive feedback response is maximized.

Experimental quantitative descriptions of nanoscale intermediate transport for *in situ* analysis of aqueous systems can be achieved by scanning electrochemical microscopy.⁵³ Platinum (Pt)

nanoparticles have recently been imaged with electrochemical resolution of ~ 50 nm.⁵³ As the analysis size approaches the tip and tip-surface separation, the effects of the tip can have large effects on the electrochemical response.^{55,73,104,141,149} Figure 1-9 shows a gold mesh surface electrode with SiO_2 holes, where the tip-surface separation was varied. The electrochemical mesh radius varies with the tip-surface separation.¹⁴¹ This variation in electrochemical feature sizes as a function of tip-surface separation for planar gold mesh increases for non-planar active sites.

The effects of tip-surface separation can be exacerbated when particle sizes, $r_{particle}$, approach the separation distance, d (Figure 1-4), where $r_{particle}$ is a substitute for r_{surf} . In this case, the distance for

diffusion is minimized from the particle to the side of the

tip in non-apex positions. This is particularly true for non-planar tip electrodes imaging non-

planar surface sites, which is qualitatively illustrated in Figure 1-11 . This can cause an error of

the position dependent electrochemical response by as much as the base radius of the tip (~ 125 nm).¹⁴¹ As discussed above, the transition from a planar to hemispherical tip and further towards

a conical tip electrode shows minimized effects of hindered diffusion. Additionally, the

separation dependent response can influence the response. As such, a constant separation is

desirable.^{101,112,120} However, the trajectory of the probe varies dependent on the mechanism of

tracking the surface, i.e. physical interactions in AFM, and the tip geometry. Example tip

trajectories for three different tip

geometries, disk, hemisphere, and

cone, are illustrated in Figure 1-10. It

is shown that dependent on the

relative aspect ratio of the surface

and tip electrodes, the trajectory

varies significantly. The trajectory

can also induce probe effects

compared to *operando* (when the tip is not present), particularly for low aspect ratio tips. Mirkin

et al., when examining approach curves with tips of different geometries, first introduced the

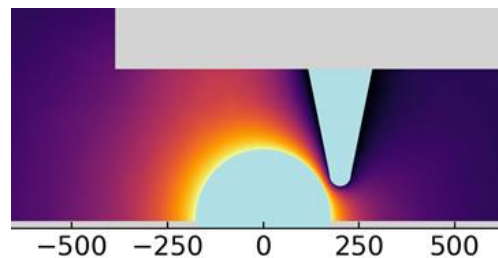


Figure 1-11: Interaction of tip side with a nanoparticle. Adapted with permission from [325].

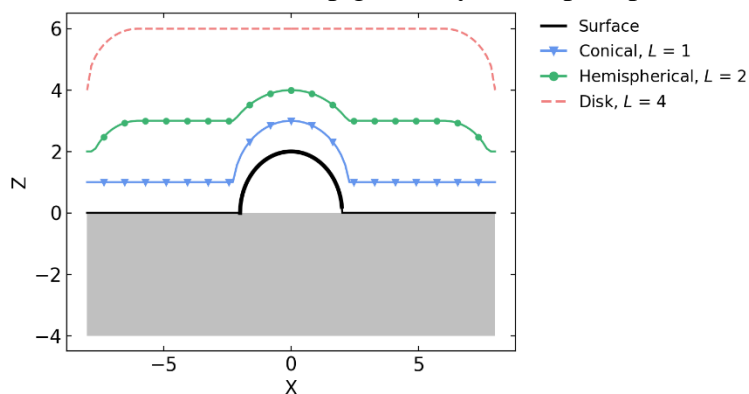


Figure 1-10: Constant separation tip trajectories for varied tip geometries with a base radius 1/2 the radius of the hemispherical nanoparticle. Adapted with permission from [325].

effects of the probe.¹⁴⁹ The changing tip geometry resulted in a demonstrably different approach curve response.

Currently, there has been no study of the removal of these effects. Generally, the literature has been satisfied with electrochemical current images and refrained from correlation to *operando* concentration results due to the known probe effects. Critelli et al. provide the single recent study in which the probe effects are suggested to be minimized in a stationary measurement by moving further from the surface.¹⁵⁰ Additionally, they study the transient effects of a growing boundary layer and find that local pH increases beyond neutrality at large overpotentials. This dictates the need to account for water reduction as well as proton reduction for hydrogen evolution.¹⁵⁰ In this study, Critelli et al. computationally controlled the proton reduction rate, through constant flux simulations. Water reduction flux is separately varied only at large proton reduction rates. They show that the pH at the probe does not grow beyond neutrality without water reduction occurring. Using a buffer, they see a maximum pH difference of 1 due to the probe without water reduction. This is at large flux values for proton reduction when the probe is relatively close to the surface.¹⁵⁰ Moving the probe further from the surface will directly impact the electrochemical resolution of the probe and limit the electrodes available for analysis.

Understanding the effects that these *in situ* phenomena (hindered diffusion, tip geometry, kinetic consumption/generation, migration, and imaging with non-apex regions of the tip) (Figure 1-11) have on the SECM response can lead to an understanding of what the system might look like when no tip is present (*operando*), and, therefore in environments that will more closely represent operational environments. Here, *in situ* is defined as the collection of data under conditions relevant to practical operation.¹⁵¹ Practically we use this to define when a

surface is under operational conditions and is being studied by SPM. We then define *operando* as under identical surface conditions when the probe is not present, where *operando* is defined *in situ* data collection under a “real” operating environment.¹⁵¹ Use of a model to match experimental results, followed by operation when the tip is no longer present near the surface is proposed for visualizing *operando* active site responses.

Mathematical descriptions of nanoscale catalytic systems to remove the effects of the tip is a necessary development for quantitative descriptions of *operando* molecular channeling. Finite element modeling to understand and remove effects due to tip proximity to surface features and nanoscale detection of enzymes will provide the tools needed to detect and analyze relatively small concentration profiles. Individual cascades will have small concentration fields, requiring previously mentioned techniques to describe concentration profiles and describe the channeling of intermediates between sites.

1.3.1 Continuum Modeling

Continuum modeling uses bulk chemical properties rather than observing molecular or atomic-scale interactions. Such simulations are highly useful for simulating large volumes of solutions on experimentally relevant time scales. Partial differential governing equations can be solved numerically using techniques such as the finite difference method (FDM) and finite element method (FEM). In these methods the simulated geometry is divided into small finite elements, which are interconnected at nodes.¹⁵² Each element is independently defined by the mathematical governing partial differential equations (PDEs).¹⁵³ The governing PDEs are approximated by a polynomial; most typically a linear function is used. Each node acts as a bridge between elements, in which the solutions are equivalent. By using enough simplified

elements, an accurate approximation of real physical phenomena is solved in a piece-wise manner. Given a set of boundary conditions, every PDE is solved simultaneously.¹⁵⁴

Different from FDM, FEM interpolates along a given element, between nodes. This allows for solutions to be applied across the entire sample space, rather than only at nodes. To accomplish this, the weak form (integral form) of the governing equation is used. Where the integral of the approximation is continuous as compared to the derivative form which may not be. The numerical approximation is highly dependent on user input functions. It allows variation of parameters that may otherwise be impractical. As such, an experimentally informed model can provide insight into parametric dependence.¹⁵⁵

The ability of FEM to study complex surface geometries and their correlation with kinetics and mass transport provides a unique advantage in studying electrochemical reactions. There has been numerous numerical studies of SECM systems.^{16,49,74,77,137,156–164} Most closely to the work presented here, Stephens et al. studied altered spatial resolution of SECM responses due to complex tips.^{165,166} The models have progressed from simple ultra-microelectrode (UME) responses to increasing kinetic and geometric complexity.^{161,162,165} Carneiro-Neto also studied the pH change during hydrogen evolution, incorporating varied reaction mechanisms to compare to experimental results.¹⁶⁷ The diffusion in a nanoporous gold electrode was studied by Haensch et al.¹⁶ where a complex surface geometry with an SECM probe is simulated to determine porosity. Additionally, continuum modeling has been applied to transport studies that SECM could potentially provide unique experimental insight. Two different types of cascade channeling, electrostatic^{168,169} and physical confinement¹⁷⁰ channeling, have been studied.

1.3.1.1 Probe Effects

Quantitative analysis of experimental results typically involves the correlation of tip current with properties and/or substrate concentration. The interference of electrochemical probe has been previously characterized by continuum modeling using considerations such as hindered diffusion¹⁵⁰ and positive feedback.¹⁷¹ The electrochemical effects of the probe in SECM are introduced in early literature⁴⁹ and discussed above. However, the consideration of these effects on the mapping response and concentration correlation has only recently been discussed.^{21,119,150,165,166} Due to the transport of species, there is a generally smearing of electrochemical response in comparison to their correlated physical sites.

With the increasingly widespread use of nanoscale tip electrodes,^{70,101,104,158,172–175} consideration of probe effects is a critical phenomenon for nanoscale surface sites. The small gap between the tip and surface restricts vertical diffusion, without restricting radial diffusion remains in a cylindrical coordinate system. Hindered diffusion also can spread out the electrochemical response signal beyond its complementary physical feature. This can be exacerbated by geometric factors such as the presence of an insulating layer on the SECM tip.^{176,177} Conical electrodes, having a large ratio of base diameter to tip height, can potentially minimize hindered diffusion. Such electrodes may be employed in combined AFM-SECM systems, which utilize the tip-surface interaction force to track surface topology.^{141,149,176} Correlation of a tip current map with an analytical or computational model is one way to derive site specific properties about the system.^{53,136,178}

In this thesis, while we show that there can be significant impact due to the presence of the probe, we also show that important conclusions can also still be drawn from experimental results. We show that accounting for the effects of the probe can have a vast improvement on the

resulting interpretation. The use of FEM can numerically remove the tip effects after the experiment has been completed, while proactive consideration of probe effects can allow for modification of the tip geometry to mitigate these effects *a priori*.

1.4 Catalyst Cascades

Multi-step catalytic reactions are exploited to drive energy conversion/storage,^{179,180} chemical sensing,^{181–185} and chemical synthesis.^{186,187} Conventionally, this is achieved in successive batch reactors and/or continuous reactors with intermediate purification steps. Separation of the intermediate often is costly and necessary for maximum efficiency. To minimize separation costs, a single reactor synthesis method is preferred.^{180,188–191} This decreases the potential for side reactions at the catalysts, consumption of the intermediates, and contamination of catalytic sites.¹⁹²

One-pot catalysis for multi-step reactions often makes use of multifunctional,^{188,193–195} and tandem^{179,180,188–192} catalysts. Multifunctional catalysts have multiple distinct catalytic sites on a single catalyst. Tandem catalysts complete multiple distinct chemical transformations in succession. There are several examples of one-pot catalysis,^{180,186,187} including the oxidation of ethylene to acetaldehyde.¹⁹⁶ However, a significant portion of these are done in a batch reactor. These processes can be further optimized through control of the intermediate between active sites.^{37,197–204} Preventing unstable intermediates from interacting with the bulk solution could further enhance the overall efficiency. Figure 1-12 illustrates the difference in multi-pot synthesis, one-pot synthesis, and cascade channeling, where cascade channeling is a subset of one-pot synthesis in which the intermediate is transported directly to the second active site.

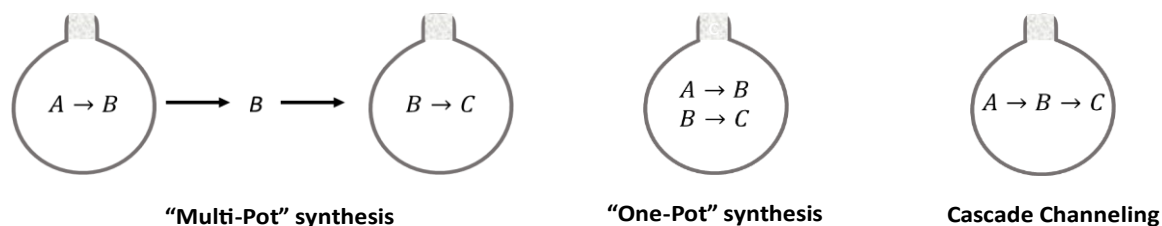


Figure 1-12: Multi-step reaction synthetic schemes: multi-pot synthesis, where individual reactions take place in separate reactors; one-pot synthesis, where all reactions take place in a single reactor; and cascade channeling where the intermediate transport is guided from one active site to the sequential active site. [189]

The design of a transport mechanism for these intermediates presents a significant design challenge. An efficient transport mechanism that prevents loss of intermediate to the bulk, stabilizing the intermediate, while also allowing rapid transport between active sites. The detection of these phenomena experimentally presents another formidable challenge.

1.4.1 Natural Substrate Channeling Mechanisms in Catalyst Cascades

Nature uses catalyst cascades to sequentially convert chemicals efficiently. The intermediate between sequential steps is transported between active sites through a guided transport mechanism.³⁷ These transport mechanisms include electrostatic channeling,²⁰⁵ chemical swing-arm,²⁰⁶ and confinement of the intermediate.²⁰⁷ Using nature as a guide, it is intriguing to work towards efficient one pot synthesis of multi-step reactions through the use of artificial cascades. However, the diagnosis of intermediates and the transport efficiency can be challenging. The ~10 nm length scale of transport provides a unique challenge for measurement in aqueous systems. At this scale, the use of a physical probe will undoubtedly influence the surrounding concentration profile; therefore, accounting for the effect of the probe is necessary.

Molecular tunneling confines the intermediate in a space in which it traverses, separate from the bulk species to the second active site.^{206,208–215} A cleaved amine group is transferred through a tunnel and used in the formation of phosphoribosylamine and pyrophosphate.²¹¹

Electrostatic channeling is the transport of a charged species through interactions with an oppositely charged interface.^{200,201,205,216–221} It takes advantage of charged “highways” and the fact that many intermediates are highly reactive due to instabilities, manifesting in a charge imbalance. Negatively charged indole interacts with a positively charged “highway” connected the α and β subunits on tryptophan synthase, directly transferring for tryptophan production in the β subunit.²¹⁸ Mechanical transport mechanisms, such as a swing arm can chemically bind an intermediate and move it from one location to another, before releasing it at the second active site.^{207,222–226} During the oxidative decarboxylation of pyruvate to acetyl coenzyme A (acetyl-CoA), an acetyl group is transferred from the initial site to a second active site.²²⁶ Spatial-sequential organization of enzymes has been shown to be effective at sub-nanometer separations.^{227–234} Channeling mechanisms show an order of magnitude increase in diffusion length while still effectively transporting the intermediate.³⁷

1.4.2 Recent Developments

Current mechanistic descriptions are primarily multi-scale models.^{197,201,235–237} Continuum and kinetic Monte Carlo analysis require physical parameters to be input,^{197,235} while molecular and Brownian dynamics can derive individual parameters, but struggle to simulate the entire cascade. Kinetic Monte Carlo has been combined with molecular dynamics to sample enzyme kinetics with turnover frequencies of $\sim 100 \text{ s}^{-1}$.¹⁹⁷

Atomistic to mesoscale modeling of intermediate channeling suggests it's a source of increased efficiency in cascades,^{197,201,237} but there was no experimental evidence of channeling¹⁹⁹ until Elcock et al.²⁰⁰ and others recently.^{197,198} Experimental analysis of cascade intermediates has been limited to indirect analysis, in which the response of a cascade is disturbed, and the change is monitored. Isotope enrichment or depletion, resistance to side

reactions, active site inhibition, and transient time analysis have all been used for indirect measurement of cascade intermediates.^{198,200} The presence of products from competitive side reactions are indications of intermediate presence in the bulk. Similarly, competitive inhibition of a reaction involving a channeled intermediate probes channeling. The degree of inhibition varies with the relative concentration of intermediate surrounding the active site.¹⁹⁸ Enzymes cascades with coupled cofactor (e.g. NAD⁺/NADH) channeling can be examined by isotope changes in concentration. The time to reach steady state can be used to express the degree of channeling.^{198,200} Comparison of the time to reach steady state^{197,198,200} for competitive enzyme reactions of oxaloacetate allows for evaluation of channeled oxaloacetate. Channeled oxaloacetate is not exposed to the bulk, and therefore, competitive enzyme aspartate aminotransferase decreases activity in the event of channeling.¹⁹⁸ To the authors knowledge, there is no current experimental results for direct measurement of cascade channeling.¹⁹⁸

1.5 Carbon Dioxide Reduction

The amount of greenhouse gases in the atmosphere continues to increase. The Keeling Curve in Figure 1-13, which monitors the atmospheric CO₂ concentration shows an accelerating accumulation from the 1960's till present day.²³⁸ The continued increase has been followed by an increasing global average

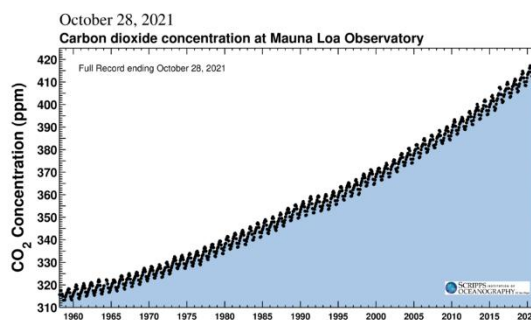


Figure 1-13: Keeling Curve showing CO₂ atmospheric concentration over time. Reproduced with permission from [238].

temperature and increasingly chaotic weather events. Efforts to curb the production of greenhouse gases must be complimented by the removal of these gasses from the atmosphere. One method is to take greenhouse gases and turn them into value added products. In this way it

is often discussed as closing the carbon cycle, in which the carbon emitted from various processes can be used to regenerate chemicals. This is represented in Figure 1-14, where CO₂ from the atmosphere and directly from emission sources would be captured and purified.²³⁹ The CO₂ would then be converted to value added chemicals and fuels.²⁴⁰

However, the stability of CO₂ necessitates the use of catalysis and/or energy input to initiate conversion.²⁴¹ Use of non-renewable energy sources to drive these reactions is counterproductive. Electrochemical CO₂ reduction provides a straightforward path for the use of alternative energy sources to drive CO₂ conversion.²⁴⁰ Generation of

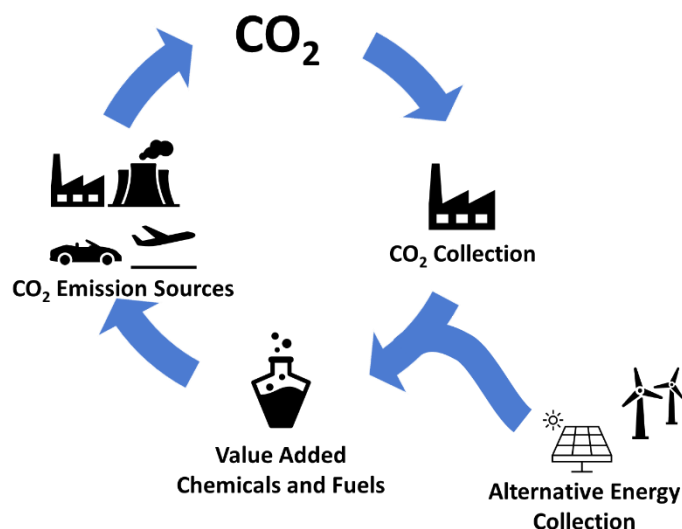


Figure 1-14: Potential CO₂ carbon cycle schematic. [239]

fuels from sustainable energy sources such as wind and solar can help relieve the intermittency of these sources. It also can be directly incorporated into the existing electrical grid.^{242–244} Reduction of CO₂ on metal and metal oxides have been found to be able to produce C₁, C₂, and/or C₃ compounds depending on the catalyst used. Some of the primary species electrochemically formed have been shown to be carbon monoxide, formic acid, formaldehyde, methane, methanol, ethylene, ethanol, acetate and n-propanol.^{240,241}

Work by Hori et al. in 1994 showed that there are certain metals such as copper that have a tendency for catalysis towards generation of C₂₊ species from CO₂.²⁴⁵ Recently the complexity

of these systems have only begun to unfurl the controlling factors. The important factors controlling the products for CO₂ electroreduction are not limited to: electrolyte species^{246–248}, pH^{19,21,91,249,250}, potential^{241,249}, catalyst^{251,252}, temperature^{253–258}, pressure^{256,258}, and reactor type²⁵⁹. Many of these factors are often related to each other and therefore it is hard to decouple the effects of specific factors.

Table 1-2: Electrochemical CO₂ reduction and hydrogen evolution reactions and their formal potentials. [239]

Reaction	E^0 V vs. RHE
$CO_2 + 2H^+ + 2e^- \leftrightarrow CO + H_2O$	-0.10
$CO_2 + 2H^+ + 2e^- \leftrightarrow HCOOH$	-0.20 (pH<4) -0.20+0.059V*[pH-4] (pH>4)
$CO_2 + 4H^+ + 4e^- \leftrightarrow HCHO + H_2O$	-0.07
$CO_2 + 6H^+ + 6e^- \leftrightarrow CH_3OH + H_2O$	0.02
$CO_2 + 8H^+ + 8e^- \leftrightarrow CH_4 + 2H_2O$	0.17
$2CO_2 + 12H^+ + 12e^- \leftrightarrow CH_3CH_2OH + 3H_2O$	0.09
$2CO_2 + 12H^+ + 12e^- \leftrightarrow C_2H_4 + 4H_2O$	0.08
$2CO_2 + 2H^+ + 2e^- \leftrightarrow C_2O_4^{2-}$	-0.59
$2H^+ + 2e^- \leftrightarrow H_2$	0.00 (pH <7)
$2H_2O + 2e^- \leftrightarrow 2OH^- + H_2$	0.00 (pH >7)

The lack of hydrogen atoms in CO₂ as compared to the organic products hints at the importance of pH in CO₂ reduction (CO₂R) as shown in Table 1-2. Particularly for C₂+ molecules, which have differing pH behavior. Up till date, the full dependence of these reactions on pH has yet to be fully understood. Local pH is thought to be a more accurate metric rather than bulk pH. However, time and physical resolution have limited the understanding.^{19,21,64,107,260,261} Different potential mechanistic rate limiting steps have a dependence on pH, resulting in changes in the expected tafel slope.²⁶² The proposed first electron transfer step of CO₂ adsorption on the surface electrode has a derived tafel slope of 116 mV/dec.²⁶² CO forming electrodes such as Ag and Au have been shown to be independent of pH. Tafel analysis indicate that the CO₂ adsorption step is rate limiting.²⁶² The onset potentials for hydrogen evolution (HER) and CO₂ reduction (CO₂R) are close (Table 1-2). HER has high activity on metals. The competition between these two sets of reactions and pH dependence for proton reduction (PR) suggests that minimizing PR can increase CO₂R. Increasing electrode thickness of porous metal oxides have been shown to increase the CO₂R activity. It is suggested that this is due to a local increase in pH.²⁶³

Electrolytes not only control the pH but are thought to impact the stability of surface species. Varela et al., have shown that the use of different halides in the electrolyte impact the product distribution, specifically for CO and CH₄ in the presence of Br⁻ and I⁻ respectively.²⁶⁴ Figure 1-15 shows an increase in methane formation when I⁻ is present compared to when it is not. They conclude that

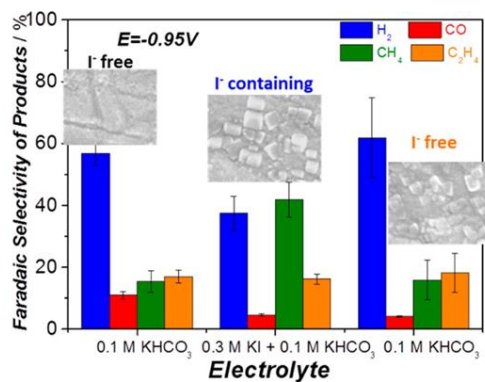


Figure 1-15: Faradaic selectivity of the gaseous products after 10 min of bulk electrolysis at a constant potential of 0.95 V vs. RHE. Insets include the SEM images of the surface after reaction. Adapted with permission [264].

it is due to a change in the electronic structure from the I^- interacting with the copper electrode. Hori et al. showed the dependence on cationic species. It was argued that the hydration of the cations affected the local pH, and therefore the product distribution.²⁴⁷ Additionally, it has been shown that there is a dependence on buffering capacity of the electrolyte species as well. The local pH increases due to a lack of buffering in some electrolyte, lowering hydrogen evolution. It also affects the C_1/C_2 ratio.^{265–267}

White et al. have neatly displayed the activity and selectivity of CO_2R for various metals studied by Hori et al.¹⁰ results over a periodic table in Figure 1-16.²⁶⁸ Metals^{245,269} and metal oxides^{263,270–273} have primarily been the focus of bulk electrode materials, with recent studies on nanoparticle^{241,271,272} and dispersed metal sites^{41,274–283}. It has been found in aqueous electrolytes that formate is the primary product for CO_2 reduction on Pb, In, Sn, and Hg electrodes. CO is the formed at high selectivity for Au, Ag, and Ga, while also being formed with Zn and Pd electrodes. Interestingly, Cu and copper alloys have been found to form hydrocarbons.^{10,245} A

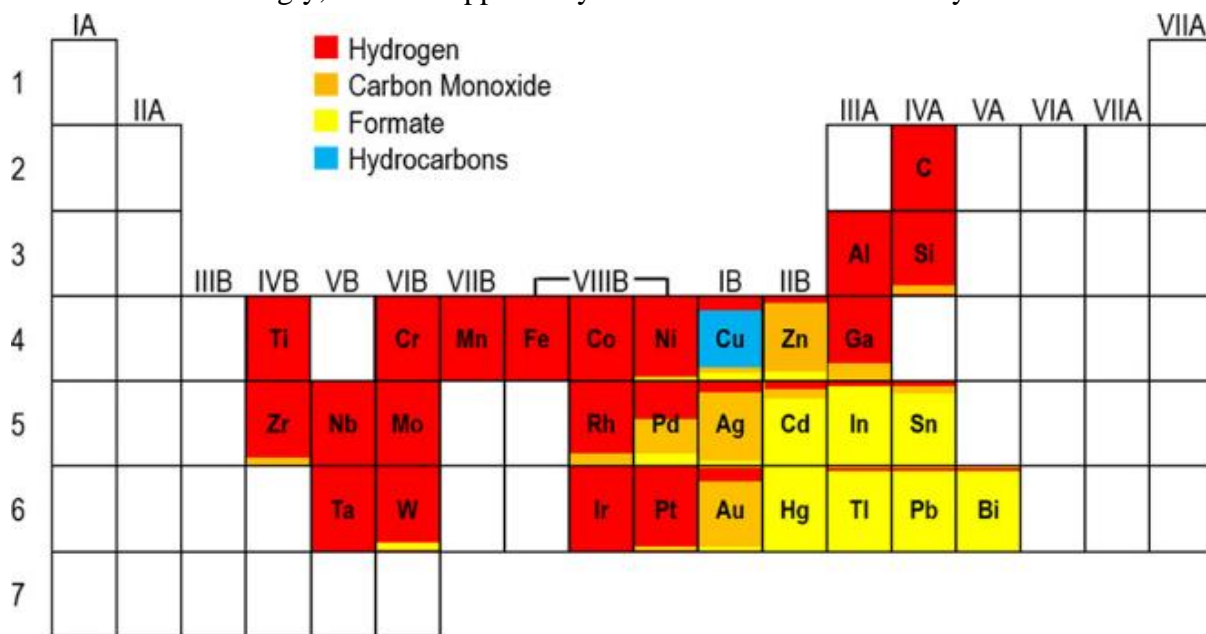


Figure 1-16: Periodic table depicting the primary reduction products in CO_2 -saturated aqueous electrolytes on various electrodes based on data from Hori et al. [245] Reprinted with permission from [268]

primary factor in the product differentiation has been determined to be the binding energy of intermediate CO on the electrode surface. Too strong of binding results in CO poisoning, and too weak of binding results in CO desorption upon formation. Copper has been found to have a medium binding energy for CO allowing further reaction to hydrocarbons.²⁶⁹

A decrease in temperature has been found to increase the selectivity for methane formation on copper while also decreasing the HER competitive reaction.^{253,254,284} Maier et al. showed that at elevated temperatures over Pt, formate ions are formed.²⁸⁵ The effect of temperature and pressure on nickel electrodes was found to have a positive correlation with hydrocarbon formation by Kudo et al.²⁸⁶ As the pressure increases, the CO₂ in solution increases. For C1 reactions it has been shown to have a linear dependence.²⁵⁶

Electrochemistry has a rich history in proton detection. Using an electrochemical probe can be a way to address the limitation for local pH diagnosis. The presence of the probe is found to have a large effect on the detected pH. Therefore, accounting for the probe will allow for better understanding of the reactions occurring.

1.5.1 Recent Developments

Previous measurements have shown the importance of local pH on CO₂ reactivity.^{19,21,64,66,261,287} In 2005 Gupta et al.²⁶¹ modeled the local pH as compared to the bulk in CO₂R. Combined with early work by Hori et al. showing pH dependence for product selectivity, the local pH is determined to be an important parameter. Quantifying the pH gradients formed in the diffusion layer during CO₂R is crucial to gain a better understanding of the reaction. Even though various techniques are available for measuring local pH in electrochemistry³², directly measuring the pH in the diffusion layer during CO₂ reduction is challenging. This is due to the

complex reaction environment, and the fact that, the signal and stability of the pH probe should not be affected by the reactants, products, or the electrolyte identity.

To date, pH measurements during CO₂ reduction under stationary conditions have been mainly achieved using spectroscopic techniques. Yang et al.²⁸⁸, for instance, used surface enhanced infrared absorption spectroscopy (SEIRAS) to determine the pH near the surface during CO₂R on sputtered copper thin films by monitoring the change in signal intensity of the species composing the phosphate buffer used (H₂PO₄⁻/ HPO₄²⁻/ PO₄³⁻). Results showed that even in strongly buffered electrolyte, the pH near the surface differs from the bulk at current densities lower than 10 mA cm⁻². Ayemoba et al.²⁸⁹ probed the pH during CO₂R on gold thin films using surface-enhanced infrared absorption spectroscopy in the attenuated total reflection mode (ATR-SEIRAS). In this case, the ratio between the integrated absorbance of the CO₂ and HCO₃⁻ bands was used to estimate the pH near the surface. Similar measurements, were recently reported in a flow cell using Raman spectroscopy.²⁹⁰

Although, in general, these spectroscopic techniques can provide valuable information about the concentration of species in the first few nanometres above the surface, the signal obtained is averaged over a large surface area. Furthermore, these measurements require having infrared or Raman active species in solution, and the pH is measured indirectly – by monitoring species whose signal is a function of the proton concentration. If these species are also affected by other variables of the reaction environment, the signal might be a convolution thereof. Therefore, spectroscopic techniques can be limited in terms of electrode materials and electrolytes that can be employed.

As an alternative to spectroscopy, Zhang et al.³³ have recently used the rotating ring-disc electrode technique to measure changes in pH during CO₂ reduction on gold under mass

transport control. In this case, a correlation between potentiometric pH measurements with IrOx and shifts in the CO oxidation peak detected with a Pt ring were used to determine the disc pH. Even though this allows for pH measurements under mass transport control, the method is limited in terms of temporal (when IrOx is used) and spatial resolution (similarly to spectroscopic techniques). Additionally, even though the CO signal on platinum is used as pH probe, it is known that this reaction is not only affected by pH²⁹¹, but also cation identity²⁹² or surface structure.²⁹³ Billy et al. demonstrated a peak shift of CO oxidation at the ring electrode is a quantitative description of the local pH during CO₂ reduction at the gold disk electrode.²⁹⁴ Dunwell et al. found that selectivity can be improved at higher current densities and sufficient CO₂ transport to the surface.⁶⁵ The ability of flow cells to maintain alkaline conditions under high current densities for CO₂R was demonstrated by Henckel et al. using SERS.¹⁰⁷ The 3D pH profile during CO₂R over a morphologically non-uniform surface was examined by Welch et al. The catalytic activity in narrow regions were observed to have an increased activity, correlating with an increase in the local pH.³⁸ Monteiro et al. have shown a stable pH probe for a wide range of pH with high temporal resolution. The local pH was shown to vary up to 7 pH units with potential.²¹

Detecting the local pH during CO₂R is challenging because it requires control of the proximity to the catalyst and the variety of species in solution. Recent work on detected local pH has been correlated to selectivity.^{19,33,38,65,66,265,289,294,295} This was also initially done by Gupta et al.²⁶¹ who correlated simulated local pH with current efficiency data from Hori et al.²⁶⁵ The main analytical tools recently used are RRDE,²⁹⁴ ATR-SEIRAS,⁶⁵ SERS,¹⁰⁷ confocal fluorescence,³⁸ and SECM.²¹

Simulations on the probe effect, particularly under HER, have been instrumental in understanding the mechanisms controlling the local pH changes. Gupta et al. showed that the local pH in unbuffered, somewhat buffered, and buffered solutions during CO₂R is impacted by the diffusion layer thickness. Unbuffered solutions were demonstrated to have the largest difference in local vs bulk pH. Additionally, the pH during CO₂R have been simulated as well.²⁶¹ Singh et al. used a multiscale simulation approach to validate the CO₂R reaction mechanism on a Ag (110) cathode, including the current density, to match experimental results. The simulations account for local pH changes allowing for good agreement between simulation and experiments.¹⁹ Ringe et al. differentiated tafel slopes, and therefore assumed mechanisms, for CO₂R. They show potential dependent pH results, where the bicarbonate was eliminated as a possible source for reactant CO₂ in CO₂R.²⁹⁶ The local pH change during HER using FEM was simulated by Carneiro-Neto et al. They demonstrated large pH range from local to bulk pH where the local pH became alkaline while the bulk pH was acidic.¹⁶⁷ The effect of the probe (pg. 18) has been simulated by Critelli et al., where they simulated probe effects for HER on an IrO₂ potentiometric electrode.¹⁵⁰ They focus on distances greater than typical analysis seen in SECM with RG=10 and conclude that larger separation minimizes the effect of the probe.

1.5.2 Probe Effects

During CO₂R in an aqueous solution, hindered diffusion beneath the probe minimizes proton diffusion, causing an increased depletion of protons. This causes an increased pH beyond the local pH increase expected on the surface electrode in general. The buffering from carbonate species will also change due to the proton consumption. When studying the effect of pH during CO₂ reduction it becomes important to remove the effects of the probe. The increased complexity makes this a non-trivial task and complicates the response further.

Typical UME pH measurements have thus far been with a stationary electrode.^{91,150,261,297,298} Instead the logarithmically varying concentration (pH) is transient and spatially dependent.²¹ The pH at the probe, due to hindered diffusion, is a function of the probe geometry and position. The probe shape (disk, cone, hemisphere, etc.) can be shown to have a varied probe effect. This is due to a differing amount of hindered diffusion.¹¹⁹ The probe size will impact the amount of hindered diffusion as well. Additionally, the closer the probe is to the surface, the more effect it will have on the probe response. As the surface electrode changes, one would also expect the pH probe effects to change as well. This means that the kinetics and surface electrode geometry and size will all impact the effect of the probe.

1.6 Redox Couples

Analysis of SECM using feedback mode necessitates the use of a redox couple. As the size of the electrodes decrease, a large current density is preferred to differentiate from noise. As such, the response should not be limited by a kinetically slow redox couple. Therefore, the ideal redox couple is a fast heterogeneous electron transfer redox couple. Often this favors outer sphere reactions in which adsorption is not required. The potential window should also be optimized such that there are no competing electrochemical reactions. In aqueous electrolytes, the redox couple should be within the stability region of water and a given electrolyte. Additionally, SECM reactions are typically longer electrochemical experiments and the stability of the redox couple is also crucial.

Photo- and thermal stability, toxicity, and solubility are important factors when choosing redox couples. Polcari et al. have neatly summed up 133 molecules that have been amperometrically detected in SECM. Of these, 102 have been used for feedback mode analysis. These couples can be further down selected for aqueous redox couples (62) that have been used

for kinetic analysis (17).²⁹⁹ This list is not meant to be exhaustive, but rather instructive of what has been used previously. Transition metal-based couples are more common due to the increased number of oxidation states and relatively low electronegativity. A low electronegativity indicates the standard potential, the relative potential required to drive a specific reaction, for the redox couple will likely be lower as compared to redox couples with stronger electronegativity. Aqueous redox couples used in SECM are listed in Table 1-3. The extensive list assembled by Polcari et al.²⁹⁹ was narrowed down to a potential region of ~0-0.8 V vs. NHE (pH=7) considering the use of a Pt electrode in an aqueous solution.¹⁴⁵ Hexamineruthenium(II) ($Ru(NH_3)_6$) and hexacyanoiridate ($Ir(CN)_6$) are common kinetic analysis redox couples. However, they are both toxic and photosensitive. Iron based redox couples have also been commonly used with relatively mild overpotentials for aqueous systems. Pure ferrocene, a sandwich molecule with two cyclopentadienyl rings surrounding an iron center is not soluble in water, however the addition of certain ligands increases its solubility and standard potential.

Just as the stability is important, the cleanliness of electrodes has an important impact on the response and interpretation of the response. Amperometric studies are not specific and will catalyze any side reactions available. Specifically, Pt group metals are highly active for a wide variety of reactions at comparatively mild conditions.³⁰⁰ For ultramicroelectrodes (<25 μm), there is increased mass transport, and therefore an increased potential for contamination. Additionally, traditional flame sealing and polishing are not available for these small electrodes.³⁰¹ Cleaning through electrochemical cycling (CV) in sulfuric acid is known to clean platinum.³⁰² However, the stability of the AFM-SECM epoxy-glass protective encapsulation is decreased due to the use of the acid. Maintaining strong stability of the redox couple becomes increasingly important.

Table 1-3: Aqueous Redox couples used in SECM within a range of 0-0.8 V vs. NHE (pH = 7). Adapted with permission from [299].

MEDIATOR	REDOX REACTION	E0 (V VS NHE)
methylene blue	$MeB + + 2H + + 2e^- \leftrightarrow MeBH_2$	-0.08
hexaammineruthenium(II)	$[Ru(NH_3)_6]^{3+} + e^- \leftrightarrow [Ru(NH_3)_6]^{2+}$	-0.06
menadione/menadiol	$MD + 2H + + 2e^- \leftrightarrow MDH$	-0.05
1,4-naphthoquinone	$NQ + 2H + + 2e^- \leftrightarrow NQH$	-0.05
hydrogen	$2H + + 2e^- \leftrightarrow H_2$	0.00
tris(1,2-bis-dimethyl-phosphino ethane) rhenium(I)	$[Re(dmpe)_3]^{2+} + e^- \leftrightarrow [Re(dmpe)_3]^+$	0.04
pyocyanin	$PYO + + 2H + + 2e^- \leftrightarrow PYO$	0.04
vanadium	$V^{3+} + e^- \leftrightarrow V^{2+}$	0.07
1,2-naphthoquinone	$NQ + 2H + + 2e^- \leftrightarrow NQH$	0.08
1-methoxy-5-methyl phenazine methosulfate	$M - NMP + + H + + 2e^- \leftrightarrow M - NMPH$	0.10
benzoquinone/hydroquinone	$BQ + 2H + + 2e^- \leftrightarrow HQ$	0.10
N-methyl phenazine methosulfate	$NMP + + H + + 2e^- \leftrightarrow NMPH$	0.11
meldola blue	$MB + + 2H + + 2e^- \leftrightarrow MBH_2$	0.12
iron(III) ethylenediamine tetraacetic acid	$[Fe(EDTA)]^- + e^- \leftrightarrow [Fe(EDTA)]^{2-}$	0.12
4-(3-nitrosophenyl)-2,6-dimethyl-3,5-diisopropiloxycarbonyl-1,4-dihydropyridine	$R - NO + 2H + + 2e^- \leftrightarrow RNHOH$	0.16
tetramethyl-p-phenylenediamine	$TMPD + + e^- \leftrightarrow TMPD$	0.26
N,N-dimethyl-p-phenylenediamine	$DMPPD + + H + + 2e^- \leftrightarrow DMPPD$	0.30
tris(4,4'-bipyridine)cobalt(II) chloride	$[Co(bpy)_3]^{3+} + e^- \leftrightarrow [Co(bpy)_3]^{2+}$	0.30
tetracyanoquinodimethane	$TCNQ + e^- \leftrightarrow TCNQ^{\bullet -}$	0.36
tetramethylbenzidine/tetramethylbenzidine diimine	$TMBD + 2H + + 2e^- \leftrightarrow TMB$	0.42
ferrocenedimethanol	$[Fc(MeOH)_2]^+ + e^- \leftrightarrow Fc(MeOH)_2$	0.46
hexacyanoferrate(III)	$[Fe(CN)_6]^{4+} + e^- \leftrightarrow [Fe(CN)_6]^{3+}$	0.49
ferrocenemethanol	$[FcMeOH]^+ + e^- \leftrightarrow FcMeOH$	0.50
iodide	$I_2 + 2e^- \leftrightarrow 2I^-$	0.53
ferrocenecarboxylic acid	$[FcCOOH]^+ + e^- \leftrightarrow FcCOOH$	0.54
dimethylamino-methylferrocene	$[DMAMFc]^+ + e^- \leftrightarrow DMAMFc$	0.55
tris(1,10-phenanthroline)cobalt(II)	$[Co(phen)_3]^{3+} + e^- \leftrightarrow [Co(phen)_3]^{2+}$	0.59
octacyanotungstate(IV)	$[W(CN)_8]^{3-} + e^- \leftrightarrow [W(CN)_8]^{4-}$	0.61
ferrocenedicarboxylic acid	$[Fc(COOH)_2]^+ + e^- \leftrightarrow Fc(COOH)_2$	0.65
ferrocenylmethyl trimethylammonium	$[FcTMA]^+ + e^- \leftrightarrow FcTMA$	0.65

Table 1-3 (cont'd)

2,2,6,6-tetramethylpiperidine 1-oxyl	$TEMPO \bullet + + e^- \leftrightarrow TEMPO$	0.67
tetramethyl- <i>p</i> -phenylenediamine	$TMPD2 + + e^- \leftrightarrow TMPD +$	0.67
hydrogen peroxide	$O_2 + 2H + + 2e^- \leftrightarrow H_2O_2$	0.67
2,2'-azino-bis(3-ethylbenzothiazoline-6-sulfonate)	$ABTS \bullet^- + e^- \leftrightarrow ABTS2^-$	0.70
ascorbic acid/dehydroascorbic acid	$DHAA + 2H + + 2e^- \leftrightarrow AA$	0.71
octacyanomolybdate(IV)	$[Mo(CN)_8]^{3-} + e^- \leftrightarrow [Mo(CN)_8]^{4-}$	0.76
Os(2,2'-bipyridine)-2-(4-formylpyridine)	$[Os(bpy)_2fpy]^{2+} + e^- \leftrightarrow [Os(bpy)_2fpy] +$	0.76
iron	$Fe^{3+} + e^- \leftrightarrow Fe^{2+}$	0.77

1.7 Overview of work

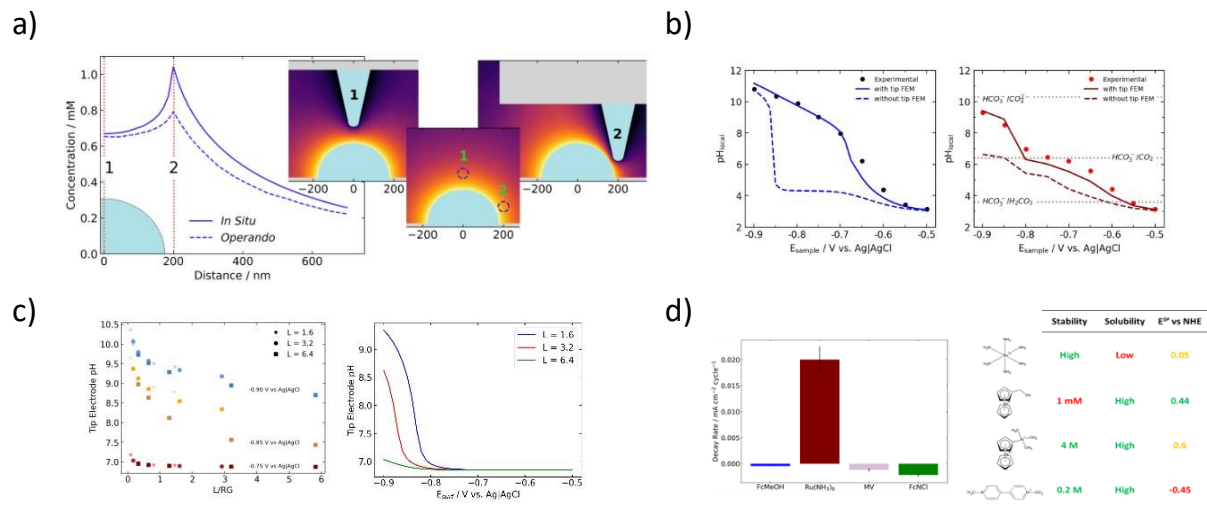


Figure 1-17: Overview of presented work. a) Tip effects during concentration measurements over a single nanoparticle, b) tip effects during CO₂R pH measurements,

This work aims to: 1) Understand and remove tip effects from SECM electrochemical responses through a combined experimental simulation approach and 2) Obtain nanoscale catalytic SECM data correlated to concentration profiles with the tip effects removed.

In Chapter 2, tip effects in AFM-SECM electrochemical responses are studied via a combined experimental-finite element method approach. The effects of tip geometry, spacing and hindered diffusion were analyzed for a fast, outer-sphere electron transfer redox couple via Butler-Volmer kinetics¹⁴⁵:

$$i = F A k_0 [C_O(0, t) e^{-\alpha f (E - E^{0'})} = C_R(0, t) e^{1 - \alpha f (E - E^{0'})}] \quad [1-6]$$

Where $f = \frac{nF}{RT}$ for the number of electrons (n), Faraday's constant (F), ideal gas constant (R) and the temperature (T). k_0 is defined as the standard heterogeneous rate constant, E is the applied electrode potential, $E^{0'}$ is the formal potential, and A is the electrode surface area. The results indicate that, for quantitative concentration mapping, it is required to account for the effects of the probe. We show that, for concentration profile correlation, conical electrodes have the least

amount of hindered diffusion, and therefore minimize the difference in the *operando* and *in situ* responses (Figure 1-17a).

In Chapter 3 the effects of the probe during pH studies are investigated. The pH is shown to be highly dependent on the probe effects, particularly at relatively medium overpotentials ($\eta = E - E^{0'}$). We demonstrate that the experimental results capture the phenomena that occurs, but hindered diffusion alters the potential dependence of this response. This effect is shown under two different reaction environments to study the effects of pH for CO₂R (Figure 1-17b). We also suggest one method for removing such tip effects.

In Chapter 4, we use simulations to proactively suggest ways in which the probe effect can be understood and/or mitigated experimentally or used advantageously (Figure 1-17c). The study of CO₂R to CO on silver is used to illustrate the combined effects of the growing pH boundary layer with the buffering from carbonate species.

In Chapter 5, we aim to identify an appropriate redox couple for kinetic analysis. We report the degradation rate of various redox couples (Figure 1-17d). We also show that the purification of as received FcMeOH improves the stability. Likely indicating the impurities are contaminating the SECM electrode.

Chapter 2

Numerical Correction of In Situ AFM-SECM Measurements[†]

2.1 Introduction

Hinderance effects due to tip geometry are typically described by current-distance relationships, or so called approach curves.^{149,176} Depending on the tip shape, more specifically the aspect ratio of tip height to base size, the measured current changes due to various forms of hindered diffusion.^{49,149,303} Tip current at positions within ~ 3 tip radii of the surface varies strongly with position, tip geometry, and the rate of chemical reactions at both the tip and the surface. Fast reactions maximize the variations observed in approach curves, and fast reactions at the tip are usually desired so that surface phenomena or transport properties are rate limiting.^{147,304} The continued interest in diagnostics near surface sites using SECM increases the need to quantitatively account for the effect of the tip in nanoscale chemical systems.^{1305,306}

Approach curves and stationary UME responses have been approximated by analytical functions fit to 2D axisymmetric models.^{49,307} Previous FEM studies by Zoski et al.¹⁷⁷ and analytical studies by Fan et al.¹⁴⁹ have shown the tip response dependence on the tip geometry. There have also been numerous studies on approach curves with varied kinetics.^{75–77,140,303} Such models typically ignore three-dimensional effects and non-ideal tip geometry. For example, analytical models of conical tips typically neglect the tip apex radius. In contrast, 3D simulations are able to account for these factors.^{165,308} The effect of non-symmetric probes on SECM responses has been discussed for non-disk shaped electrodes.^{165,309} Lack of symmetry due to the

[†] Reprinted with permission from Mirabal, A.; Calabrese Barton, S.. *Anal. Chem.* 2021, 93 (37), 12495-12503. <https://doi.org/10.1021/acs.analchem.1c00110>.
Copyright 2021 American Chemical Society

scanning of the tip electrode can induce imprecise kinetic mapping.¹⁶⁵ Surface mapping is useful for concentration determination, such as membrane transport⁶⁰ and local kinetics.^{305,310} AFM-SECM, complicated by increasingly complex tip geometries,^{311–313} can be supplemented and interpreted by FEM.^{104,141,165,309,310,314–317} A few initial FEM studies showed the effects of hindered diffusion^{147,308,318–320} and imaging of large surface electrodes.^{309,310} To our knowledge, the computational simulation of AFM-SECM systems remains sparse and the specific imaging of surface sites of the same order of magnitude as the tip size for AFM-SECM remains unexamined.³²¹

In this chapter, we focus on deriving *operando* concentration profiles from *in situ* SECM responses. This is achieved by removing *in situ* SECM tip effects through FEM, where the tip parameters are derived simultaneously by non-linear regression of a 2D FEM model for both positive and negative approach curves. These derived parameters can then be used to correct 3D, *in situ*, SECM-derived concentration profiles to estimate *operando* concentration surrounding an active surface feature, in this case a catalytic nanoparticle. We show that the response distortion is largest when the scale of surface feature is similar to that of the SECM tip electrode for low aspect ratio tips. When this distortion is significant, the response cannot be considered *operando*, but rather an *in situ* response. Additionally, we describe the concentration profile differences between *in situ* and *operando* operating conditions for a range of different tip and surface geometries. When feature sizes of the surface and tip closely match, concentration profile distortion due to the presence of the tip electrode is maximized.

2.2 Experimental

2.2.1 Materials

Platinum nanoparticles were electrochemically grown on highly-oriented pyrolytic graphite (HOPG, 2PSI) using 2 mM potassium hexachloroplatinate (K_2PtCl_6 , Sigma Aldrich) in 0.5 M sulfuric acid. A Pt counter electrode was used with a Ag|AgCl electrode. For all SECM experiments, 2 mM ferrocene methanol reference (FcMeOH, Alfa Aesar) was used as a redox couple in 0.1 M KCl aqueous electrolyte (Sigma Aldrich). The FcMeOH was purified by sublimation.³²² Positive approach curves were acquired over a gold coated silicon wafer (Electron Microscopy Sciences). Polytetrafluoroethylene (PTFE, Sigma-Aldrich, 2mm thickness) was used as the negative surface. A silver wire quasi-Ag/AgCl reference electrode (AgQRE) was used with a Pt counter electrode.

2.2.2 SECM

A Bruker Dimension Icon AFM-SECM was used for all measurements. The tip electrode was a Pt coated silicon oxide AFM-SECM tip with a reflective gold backing.³¹⁴ The base cell was a Bruker model sandwich cell of 2.3 mL volume, with polytetrafluoroethylene (PTFE) inner linings. The surface was tracked using PeakForce tapping, with a fixed force threshold of 0.135 V. Approach curve ramp rates were 0.01 Hz with a ramp distance of 2 μm , for an approach rate of 40 nm s^{-1} .

Positive approach curves were acquired over a gold surface electrode held at a fixed, mass transfer limited potential of 0 V vs. AgQRE. Negative approach curves were acquired over a PTFE inert surface. A single SECM tip was used to obtain 10 positive approach curves, and an additional tip was used to obtain 10 negative approach curves. The average of the positive and negative curves, along with 1 standard deviation are presented within this study. Sixteen data

points at exponentially increasing distances starting at $L = 0.3$ were chosen for analysis, to provide increased resolution at low tip-surface separation and avoiding snap-to-contact effects.³²³

Pt nanoparticles were deposited for 7 voltammetric cycles in the potential range -0.25 to 0.9 V vs. Ag/AgCl in 0.5 M H₂SO₄ at 10 mV/s. Topographical images of the nanoparticles were acquired using PeakForce tapping simultaneously to electrochemical mapping in solution. Watershed analysis for particle size and location determination allowed for identification of isolated particles around 100 nm in size.³²⁴

Experimental SECM mapping was conducted over an HOPG substrate with electrodeposited Pt nanoparticles. For each scan line, topography was obtained using PeakForce tapping, minimizing tip surface interactions. The same line is subsequently scanned using SECM in constant separation mode (*i.e.*, lift mode), following the previously measured topography at 50 nm separation. The next scan line was then characterized using the same procedure.

2.2.3 SEM

Scanning Electron Microscope (SEM) imaging of the SECM tip electrodes was done in a JEOL JSM-7500F Field Emission SEM. Gentle beam mode was used with a landing voltage of 1 kV. Images were acquired preceding and succeeding AFM-SECM surface imaging of Pt nanoparticles on HOPG.

2.2.4 Finite Element Model

Simulations of the experimental SECM responses are governed by the steady state Nernst-Planck mass conservation equation for each species, i , assuming no convection:

$$0 = D_i \nabla^2 C_i + z_i u_i C_i F \nabla^2 \phi \quad [2-1]$$

where C_i is the concentration of species i , D_i is the species diffusivity, z_i is the species charge, F is Faraday's constant, and ϕ represents the potential. Four ionic species were considered: potassium and chloride from supporting electrolyte, and the oxidized and reduced forms of ferrocene methanol. The species mobility, u_i , is defined by the Nernst-Einstein relation $u_i = \frac{D_i}{RT}$, where R is the gas constant and T is absolute temperature. In addition to Eq. 1, overall electroneutrality is enforced as $0 = \sum z_i C_i$.

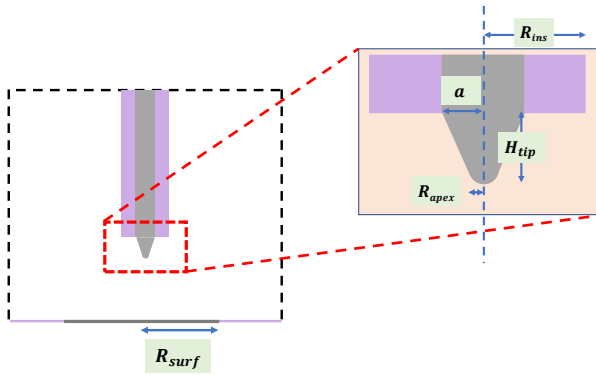


Figure 2-1: Bruker AFM-SECM Tip Dimensions. Insulating surfaces are indicated in solid purple, and electroactive surfaces in solid grey.

Table 2-1: Geometric AFM-SECM tip parameters.

Geometric Parameter	Symbol	Value (nm)
Insulation radius	R_{ins}	~390
Tip Base Radius	a	~88
Tip Radius	R_{apex}	~25
Tip Height	H_{tip}	~215

At electrode boundaries, a reversible, single electron, electrochemical reaction is assumed: ^{49,178,325}



$$-D_i \nabla C_i + u_i n f \nabla \phi = k C_i \quad [2-3]$$

$$k_A = k_0 \exp [\alpha_A f (V - \phi - E^{0'})] \quad [2-4]$$

$$k_C = k_0 \exp [\alpha_C f (V - \phi - E^{0'})] \quad [2-5]$$

where the redox reaction of the reduced species (C_R , FcMeOH) and oxidized species (C_O , FcMeOH⁺) are controlled by potential dependent elementary rate laws as seen in Eq. 2-2. The anodic and cathodic rate constants, k_A and k_C , are defined by a standard rate constant, k_0 , and potential dependency through Butler-Volmer kinetics in Eq. 2-4 and 2-5.^{140,178,325} Here, $f = \frac{F}{RT}$, the charge transfer coefficients, α_A and α_C are assumed to be 0.5, V is the electrode potential and $E^{0'}$ is the formal potential.

At insulating surfaces (Fig. 2-1), a zero flux condition is applied; at other boundaries, concentrations of all species are set to their bulk values. For negative feedback, the kinetic rate at the surface electrode, $k_{0,sub}$, is set to 0, and is used as a fitting parameter for positive feedback. k_0 is increased to 100 m/s to approximate mass transfer conditions at the electrodes.

Conical SECM tip electrode geometry is described by four parameters, a , H_{tip} , R_{ins} , and R_{apex} , defined in Fig. 2-1 and Table 2-1.¹⁴¹ In the model, the cone tip is approximated by a hemisphere of radius R_{apex} .¹⁴¹ The geometry is described by the tip height to base radius aspect ratio, $\kappa = \frac{H_{tip}}{a}$, and relative insulation radius $RG = \frac{R_{ins}}{a}$.^{149,177} Disk and hemispherical tips can be similarly described, with $\kappa = 0$ and 1 respectively. Conical probes may be used for both AFM and SECM studies, operating in constant separation mode. For the purposes of this study, however, we describe these probes as “conical SECM tip electrodes”.

Approach curve responses are modeled using a 2D axisymmetric finite element model. The simulation space boundary radius, R_{bound} , is set to 10 times that of the surface electrode radius, R_{surf} .^{75,82} The planar surface electrode radius, R_{surf} , is 10 times larger than the tip insulation radius, R_{ins} , representing a macroelectrode for positive feedback.⁴⁹

Similarly, for SECM imaging responses in which the horizontal position of the tip varies, a 3D simulation is defined. When scanning the surface with the tip, the system is asymmetrical, necessitating a 3D geometry. The tip position, L and X , are defined according to the surface.

All finite element simulations were conducted in COMSOL Multiphysics using the steady-state coefficient mode package. Example calculations are available.³²⁶

2.2.5 Analytical Approach Curve Expressions

There exists a rich literature of theoretically derived analytical approach curve functions to relate tip current to vertical position for a range of operating conditions.^{49,75,123,149,176,303,327}

Mirkin et al. have previously described analytical functions of negative and positive approach curves accounting for separation, L , and either conical tip geometry¹⁴⁹ (tip aspect ratio, κ) or the surface kinetics.¹²³ For this study, an analytical model must consider the conical AFM-SECM tip as well as reaction kinetics at both the surface and tip. A combination of previous equations for conical electrodes¹⁴⁹ and kinetic dependence^{123,149} provide initial parameterization of the approach curve responses. For a disk electrode, the positive approach curve tip current response,

$\frac{I_{disk}(L)}{I_{disk}^{\infty}}$, under mass-transfer control and with an insulation radius, $RG = 10$, was numerically approximated as:⁴⁹

$$\frac{I_{disk}(L)}{I_{disk}^{\infty}} = 0.68 + \frac{0.78377}{L} + 0.3315 \exp\left(-\frac{1.6702}{L}\right) \quad [2-6]$$

where L is the tip radius normalized tip-surface separation. For negative approach curves, Mirkin et al. propose the following correlation for current to a mass-transfer limited disk electrode with $RG = 10$:

$$\frac{I_{disk}(L)}{I_{disk}^{\infty}} = \frac{1}{0.15 + \frac{1.5385}{L} + 0.58 \exp\left(-\frac{1.14}{L}\right) + 0.0908 \exp\left(\frac{L-6.3}{1.017L}\right)} \quad [2-7]$$

where the disk current density, I_{disk} , dependent on position, L , is normalized to the value at infinite separation, I_{disk}^{∞} .

An analytical expression for the conical electrode can be developed by integrating the disk electrode expression, Eq. S2, over the height of a cone:¹⁴⁹

$$\frac{I_T(L)}{I_T^{\infty}} = \frac{2}{\kappa^2} \int_0^{\kappa} \frac{I_{disk}(L)}{I_{disk}^{\infty}} z dz \quad [2-8]$$

where I_T is the conical tip current, I_T^{∞} is its bulk value, and κ is the tip cone aspect ratio.

2.2.6 Non-Linear Regression

Parameter values were derived from experimental approach curves using a conical electrode simulation. A nonlinear least squares regression of the 2D model was conducted using COMSOL with MATLAB for positive and negative approach curves. The finite element model, described above, was solved for varying L using three adjustable parameters: the insulation thickness, RG , the tip rate constant, $k_{0,tip}$, and the tip aspect ratio, κ . Exponentially increasing values of L are used to increase the goodness-of-fit near the surface, where tip-surface feedback is prevalent. Averaged tip currents for approaches with negative and positive feedback responses were considered. The normalized tip current is compared to experimental results at the corresponding heights and the sum of the square residuals is minimized. The data was weighted

by the standard deviation of the experimental approach curves at each position, L . Initial parameter values were derived based upon analytical approach curve functions (Eq. S2-4).

2.2.7 Calculation of Concentration Profiles

Calculation of concentration through mass transfer limited relations for ultra-micro electrodes (UMEs) has been previously discussed in literature.⁶⁰ The *in situ* concentration measured at the tip electrode is calculated from steady-state current density, i_{ss} , using a corrected mass transfer limited tip current:¹⁷⁷

$$I_{ss} = nFAm_0C_0^* \quad [2-9]$$

The mass transfer coefficient, m_0 , is defined as $\frac{4D}{\pi r}$ and $\frac{D}{r}$ for the disk and hemispherical tip electrodes, respectively. C_0^* is the bulk concentration and n is the number of stoichiometric electrons in the reaction. For conical electrodes, the relation of Zoski, et al. is applied:¹⁷⁷

$$Am_0 = [A_1 + B_1(RG - C_1)^{D_1}]4aD \quad [2-10]$$

where the constants A_1 , B_1 , C_1 and D_1 are functions of κ .¹⁷⁷ Concentration profiles can be calculated using the FEM simulation with the SECM either present (*in situ*) or absent (*operando*). The *operando* case may be approximated by placing the tip 50 tip radii away from the surface.^{49,147} A selection of axisymmetric surfaces based upon literature reports^{136,141} were simulated to show the effects of different surface and tip geometries have on calculated concentration profiles.

2.2.8 3D Nanoparticle Surface Response

Pt nanoparticle surface electrodes were prepared by electrodeposition on highly ordered pyrolytic graphite (HOPG).³²⁸ HOPG was cycled at 10 mV/s between potentials of -0.3 – 1.0 V vs. RHE for 7 cycles. After thorough rinsing, this surface electrode is simultaneously

topographically and electrochemically imaged in a 1 mM FcMeOH solution, held under a constant potential of 0.0 V vs AgQRE. Concentration profile comparisons were done over a single particle. A single particle was found using watershed analysis in python.³²⁴ A cutline of tip current was taken from an SECM scan over a nanoparticle.

2.2.9 Particle Distribution

Watershed analysis (Fig. 2-7) is used to identify and analyze the nanoparticles in the AFM image (Fig. 2-5a). Watershed analysis is a region-based image analysis algorithm that segments the image based upon local topographical minima (or inverse maxima) such that an imaginative water droplet would flow to a given minima.³²⁹ For the particle of interest, the particle separation, d_i , is more than 8 particle radii from its nearest neighbor. Using an approach curve relation for a conical electrode with an aspect ratio of 3.3, we would expect a 95% recovery of the bulk current behavior.⁸⁴ Additionally, the steady-state, dimensionless diffusion field $C'(r')$ near a nanoparticle can be shown by solution of Fick's law to be:

$$C' = 1 - 1/r' \quad [2-11]$$

Where the dimensionless variables are given by $C' = \frac{C}{C^*}$ and $r' = \frac{r}{R_{np}}$, with bulk current, C^* , and nanoparticle radius, R_{np} . Here, mass-transfer limited conditions are assumed, with $C'(0) = 0$ and $C'(\infty) = 1$. From this solution, we obtain 88% concentration recovery at $r' = 8$. Based on these considerations, we assume that the particle chosen is sufficiently isolated such that its local concentration field is minimally affected by its neighbors.

2.3 Results

2.3.1 Parameter Estimation

Matching a parameterized model to the electrochemical response of an experimental AFM-SECM scan result allows for quantitative analysis of experimental results. We equate the electrochemical response of the AFM-SECM scan to a constant separation SECM scan for the

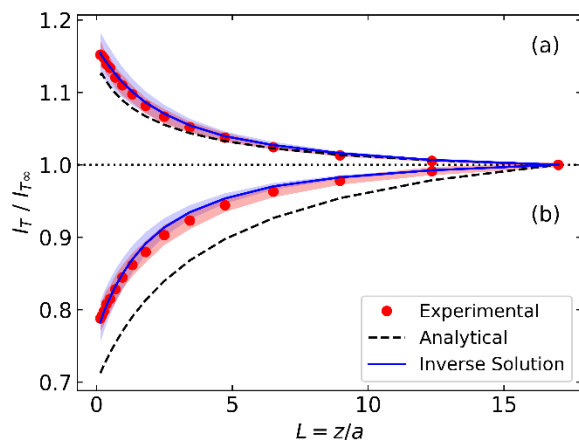


Figure 2-2: Experimental averaged approach curve responses (red dots) for (a) positive feedback over a gold macro electrode and (b) negative feedback over PTFE. Analytical approximations (dashed lines) were used for initial parameterization of the inverse solution (blue line). Shaded regions represent 1 standard deviation. The tip electrode was held at 0.3 V vs. AgQRE. The surface electrode in (a) was held at 0 V AgQRE, while held at open circuit in (b).

in nanoscale geometry between nominally equivalent tips can lead to variations in overall bulk current.

purpose of the simulation analysis. A numerical model of a scanning, conical SECM tip¹⁷⁷ goes beyond analytical approaches to account for factors such as 3D asymmetry and nonzero apex radius. To fit the approach curve current with non-standard tip geometry such as conical tips, the finite element model was solved for varying dimensionless tip-surface separation distance, L , and fit to experimental results of normalized tip current. While fitting to the unnormalized current can provide additional sensitivity, particularly close to the surface, slight variations

Here, we apply a 2D axisymmetric model to estimate geometric parameters of a conical tip using approach curves in both positive and negative feedback modes. In positive feedback mode, the tip is poised at 0.3 V vs.

AgQRE, and oxidizes ferrocene methanol at diffusion-limited current, as shown by cyclic voltammetry in bulk solution (Figure 2-3). The surface electrode, poised at 0 V/AgQRE, reduces ferrocene methanol from the tip, amplifying the tip current. Ten experimental approach curves were acquired in positive feedback mode over

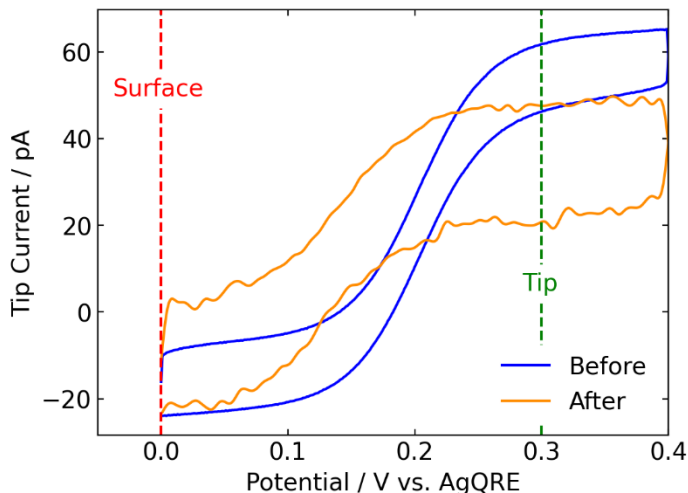


Figure 2-3: Cyclic voltammetric bulk responses of the AFM-SECM Pt tip in 1 mM FcMeOH. Cyclic Voltammograms were acquired at 20 mV/s before (blue) and after (orange) AFM-SECM imaging of a HOPG surface with Pt nanoparticles.

a gold surface macroelectrode and averaged to yield tip current as a function of tip-surface separation. For negative feedback, the same procedure was followed using a PTFE surface, which does not reduce ferrocene methanol from the tip. Mixed feedback current during approach curves (positive and negative) were avoided by using PTFE as an inert surface. The mixed feedback current is attributed to local deviations from open circuit potential. Potential average and standard deviation of responses in both experimental modes are displayed in Figure 2-2.

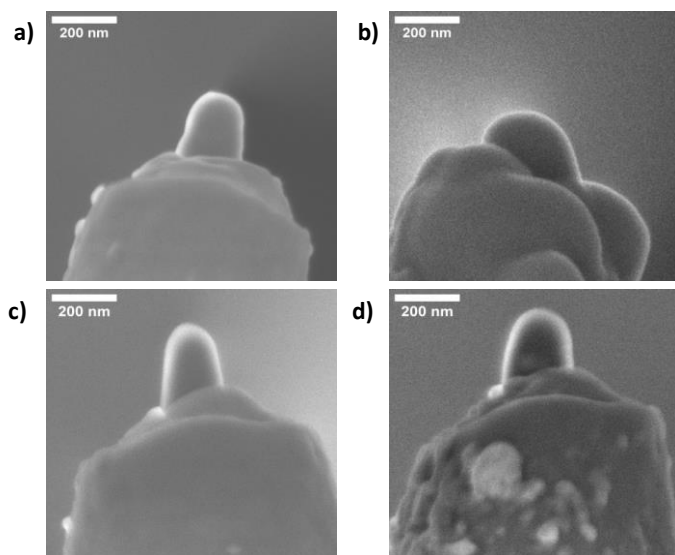


Figure 2-4: SEM of AFM-SECM tip before (a) and after (b) SECM imaging of Pt nanoparticle surface. This is compared to before (c) and after (d) SECM imaging of Pt nanoparticle surface with exclusively KCl electrolyte (no redox species is present).

For *in situ* FEM calculations, the averaged experimental data in Fig. 2-2 was simplified to 16 points at exponentially increasing tip-surface separations for both positive and negative feedback. This gives a higher point density close to the surface, where the feedback current and hindered diffusion have a larger effect. The standard deviation from the averaged currents (red shading) and

the confidence interval of the fitted FEM simulation approach curve (blue shading) are shown to be largely overlapping. The analytical approximation of the approach curve (black dashed line) largely overestimates the negative feedback current effect and underestimates the positive feedback current. The error in the analytical approximation can be attributed to a lack of consideration of the insulation radius and a simplified conical shape with no apex smoothing. By accounting for these parameters, the regressed FEM model shows an increased agreement with experiment. The simultaneous fit to both approach curves yields a coefficient of determination $R^2 = 0.998$.

Table 2-2: Fit parameters using simultaneous fitting of positive and negative feedback approach curves.

Parameter	Fit Value	SEM	Literature Value
Insulation Radius, $RG = R_{\text{ins}}/a$	6.7 ± 0.4	6.4 ± 0.6	4.5^{141}
Tip Aspect Ratio, $\kappa = H_{\text{tip}}/a$	3.3 ± 0.1	3.2 ± 0.3	2.3^{141}
Tip Rate Constant, $k_{0,\text{tip}} / \text{cm s}^{-1}$	12 ± 0.9	-	$4 - 10^{304}$

The resulting fitted parameter values and uncertainties are listed in Table 2. The geometric parameters for the tip, RG and κ , are within 1 standard deviation of values obtained by SEM observations (Figure 2-4a). The fitted value for the tip rate constant, $k_{0,\text{tip}}$, is somewhat higher but close to the range of values reported by Sun et al.³⁰⁴ In the following sections, these parameter values will be used to produce *operando* results using the FEM model.

2.3.2 SECM Concentration Profile Correlation

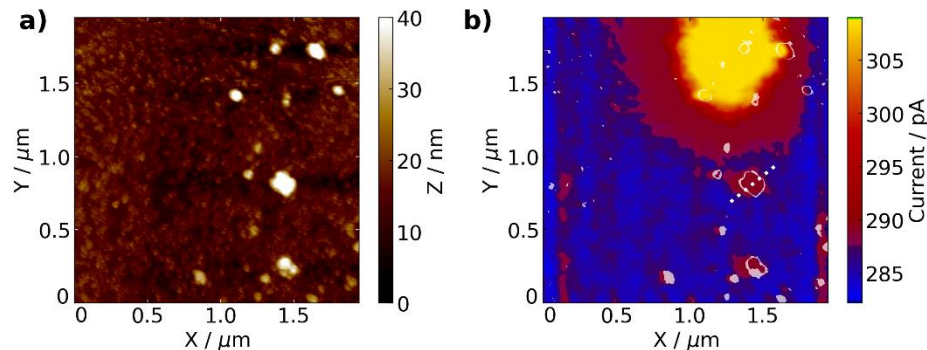


Figure 2-5: a) AFM liquid PeakForce tapping image of Pt nanoparticles deposited on HOPG in an aqueous solution. b) Experimental positive feedback SECM and overlaid AFM images of Pt nanoparticles on HOPG. (2mM FcMeOH, 0.1 M KCl) Topographical outlines of Pt nanoparticles are illustrated in white with the SECM tip current depicted by color. The tip and surface electrodes were held at 0.0 and 0.3 V vs. AgQRE respectively. Cutline current used in Fig. 2-6a is depicted by a white dashed line.

A $2 \times 2 \mu\text{m}$ region of Pt nanoparticles on HOPG was simultaneously imaged topographically by AFM, and by positive feedback from the FcMeOH couple (Figure 2-5). The tip is held at the oxidizing potential of 0.3 V vs. AgQRE. The surface is held at the reducing potential of 0 V vs. AgQRE, where the Pt nanoparticles reduce the $\text{Fc}^{3+}\text{MeOH}$ produced by oxidation at the tip. The topographical AFM image is displayed in Fig. 2-5a, with particle outlines displayed in white in Fig. 2-5b. An AFM-SECM scan operated in constant separation mode was used to record the positive-feedback tip current at a normalized tip-surface separation of $L = 0.91$. As shown in Fig. 2-5b, increasing current over the nanoparticles is indicative of positive feedback response due to surface reduction of the redox species. The higher current region in the upper right portion of Fig. 2-5b is attributed HOPG defect site activity and nanoparticles of size less than ~ 10 , which is the physical resolution of the AFM tip.

An individual nanoparticle, highlighted with a white dotted line in Fig. 2-5b., was selected after watershed analysis of AFM topography (Fig. 2-6) for particle size (Fig. 2-7) and

separation. The separation of the surrounding nanoparticles is determined to be 8 radii away, sufficient to minimize the interference in the response of the selected nanoparticle. This particle was used to generate a cross section image of the tip current, displayed in Figure 2-8a. The calculated average particle radius is 75 nm.

Cyclic voltammograms and SEM images of the SECM tip before and after electrochemical imaging of the surface (Figs. 2- 3 and 2-4, respectively) indicate alteration of the tip during imaging. The cyclic voltammograms (Fig. 2-3) show an increased capacitive current and a reduction of the overall oxidative current, indicating a change in the tip electrode. This is further confirmed by SEM before and after AFM-SECM imaging, showing a large alteration to the tip (Fig. 2-4b).

Cyclic voltammetry of the tip electrode was performed before and after AFM-SECM imaging of the Pt nanoparticle-covered HOPG surface electrode. Initially, the tip capacitive current was ~14 pA, comparable to literature values of ~10 pA.¹³⁴ Following imaging,

capacitive current increased from 14 to 25 pA and the mass transfer limited current at oxidizing potentials decreased from 64 to 48 pA. These changes are evidence of tip alteration, further supported by SEM images taken before and after AFM-SECM imaging under identical conditions (Fig. 2-4a-b). The Pt apex radius, aspect ratio, and insulation radius of the tip electrode after imaging in Fig. 2-4b are different as compared to before imaging in Fig. 2-4a.

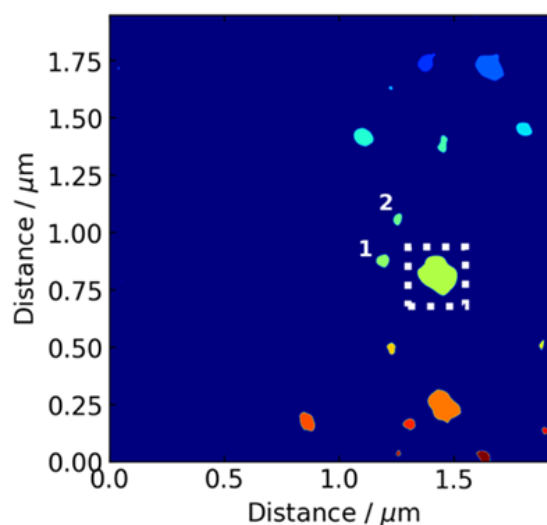


Figure 2-6: Watershed analysis nanoparticle identification of AFM image, Fig. 2-5a. Boxed nanoparticle is the nanoparticle for analysis in Fig. 2-7. Numbered nanoparticles 1 and 2 are analyzed for separation from the particle of choice.

When imaging is conducted in the absence of the ferrocene methanol redox species, with only electrolyte present, alteration is significantly reduced. As shown by the SEM images of Fig. 2-4c-d, the geometric features of the tip are largely maintained during SECM scanning. The tip in Fig. 2-4d shows slight morphological change that is within ~10% of the original geometric values.

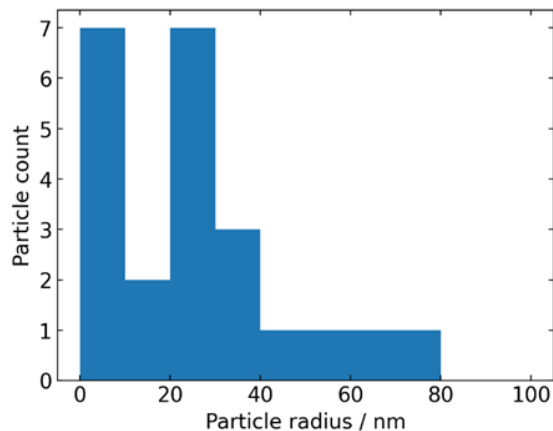


Figure 2-7: Nanoparticle size distribution from watershed analysis of AFM image, Fig. 5a.

These results suggest that tip alteration during SECM scanning is due to contamination by the redox species, ferrocene methanol.

SEM images before and after imaging without a redox couple (Fig. 2-4a-b) suggests that the alteration is primarily due to deposition of redox couple reaction products on the tip electrode.

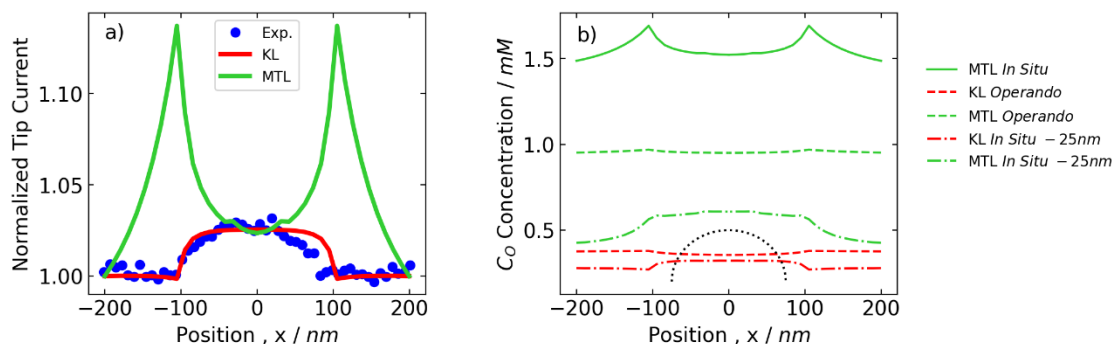


Figure 2-8: a) Experimental (blue) and FEM (Red & Green) SECM scan response over 75 nm Pt nanoparticle at 50 nm separation. b) In situ (solid) C_O concentration profiles 25 nm from the tip apex (dot-dashed), and operando C_O concentration profiles (dashed) over the 75 nm nanoparticle, represented by the black dotted hemisphere. The dot-dashed lines represent the concentration 25 nm (R_{apex}) below the apex of the tip electrode. Red curves represent simulations under kinetic limitations (KL), while green curves represent mass-transfer limited conditions (MTL) at both electrodes.

However, this change in the tip is not considered in this study as we only consider a cutline over

a single nanoparticle. We assume the degradation of the tip is relatively constant over this portion, which represents 12% of the entire scan.

The normalized current is overlaid with 3D FEM model results of SECM tip response for a scan over an idealized 75 nm radius hemispherical nanoparticle. This hemispherical particle has spherical symmetry, and so a 2D traversal is representative of the overall 3D response.

Two cases were considered: In the first case, the rate constant at the nanoparticle surface was set equal to that of the tip, or $k_{0,\text{surf}} = k_{0,\text{tip}}$, to account for kinetic limitations. In the second case, the value of the surface rate constant was set to be much greater than that of the tip, or $k_{0,\text{surf}} \gg k_{0,\text{tip}}$, to approximate mass-transfer-limited conditions. In both cases, the rate on the surrounding HOPG surface was set to 0.1 cm/s, similar to the activity of HOPG for other ferrocene compounds.³³⁰ In Fig. 2-4a, the normalized current profiles obtained from experiment (blue dots) and calculation (red line), agree well, indicating that the kinetics at the platinum nanoparticle surface are likely similar to that of the tip electrode. Moreover, good agreement is obtained between simulation and experiment without adjustment of parameters, and notwithstanding the tip degradation discussed above (Fig. 2-4). One interpretation of these results is that the observed changes in tip morphology do not substantially affect the reaction kinetics at the SECM tip.

The mass transfer approximated surface kinetics generate horn-like features at the edges of the nanoparticle where an increased portion of the tip electrode surface area is exposed to the side of the nanoparticle.

In Fig. 2-8b, calculated C_0 concentration profiles are shown for both *in situ* (tip electrode present) and *operando* (tip electrode absent) conditions, with the distinction being the change in the local environment of the surface site. The electrodes are assumed to be under either the

kinetically limited (KL, red) or mass-transfer limited (MTL, green) cases. Equation 6 is used as a MTL relation for the tip current to *in situ* concentration (solid green line). Due to the mass-transfer limitation of eq. 6, an additional *in situ* concentration, 25 nm below the apex of the tip electrode apex (Fig. 2-4b, dot-dash) was considered. The mass-transfer limited case produces a large deviation between the *in situ* and *operando* concentration profiles. Under mass transfer limited conditions, the *in situ* concentration profile has peaks at the edge of the nanoparticles due to the increased positive feedback with the sides of the conical tip, illustrated in the table of contents artwork. The *in situ* concentration 25 nm from the tip underestimates the *operando* concentration, where the mass transfer limited concentration, approximately halfway between the two active sites, is close to half the bulk concentration. The *in situ* concentration 25 nm from the surface is closer to the *operando* concentration, but is once again under representative due to the distance from the tip and nanoparticle.

2.3.3 Concentration Profile Distortions

A parameterized FEM model of the experimental system can be used to generate 2D and 3D concentration fields that describe the interaction of an SECM probe with active surfaces. In this way, we can understand how the probe affects the concentration fields surrounding surface active sites and how this might affect the surface active site response. Qualitative demonstration of concentration field distortions by the SECM probe can be observed visually in Figure 2-9, which represents mass-transfer limited conditions at both the tip and surface electrode for conical and disk tip geometries. For a conical electrode (Fig. 2-9a), the *in situ* concentration field is distorted in the vertical direction near the tip, as compared to the *operando* field (Fig. 2-9b) calculated with no tip present. Far from the tip axis ($x > 200$) less distortion is observed. In contrast, the close proximity of the insulation layer of the disk electrode (Fig. 2-9c) demonstrably

expands the *in situ* concentration field horizontally, as compared to Fig. 2-9b, due to hindered diffusion of reactant.

Fig. 2-9 clearly demonstrates one advantage of conical SECM electrodes in minimizing hindered diffusion. Removing these tip effects, through correlation of the tip current to a modeled response, allows for the analysis of true *operando* conditions. This becomes increasingly important as the surface and tip electrodes approach similar dimensions, causing their concentration fields to significantly interact. The effect of tip size can be characterized by the relative deviation in concentration for *in situ* as compared to *operando* conditions under mass transport control (Figure 2-10). For a series of conical tips of varying κ and with $R_{\text{apex}} = 0$, the effect of the relative tip size, $\frac{a}{R_{\text{surf}}}$, was studied at a constant separation, $L = 1$, and aligned axes of symmetry of the two electrodes. For a disk tip ($\kappa = 0$) and small aspect ratio cone tip ($\kappa = 3.3$), the maximum concentration difference is observed when the surface and tip electrodes are similar in size ($a/R_{\text{surf}} \approx 1$). This is due to a higher production of C_0 at the surface from positive feedback as compared to loss by diffusion. Lower κ increases hindered diffusion of C_R into the thin gap. At relatively small tip electrode radii, the difference in calculated C_0

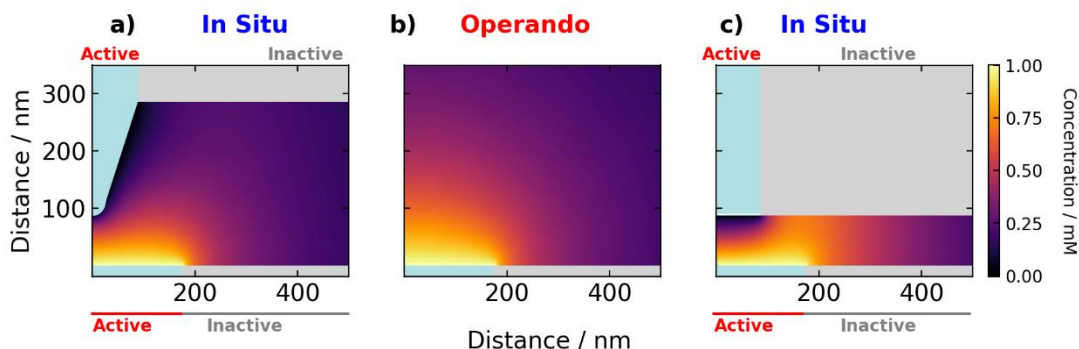


Figure 2-9: In situ C_0 concentration profile distribution due to the presence of the tip for cone (a) and disk (c) shaped tip electrodes in comparison to operando case with tip absent (b). Electrode active areas are indicated by blue shading, while grey shading indicates zero-flux insulated surfaces.

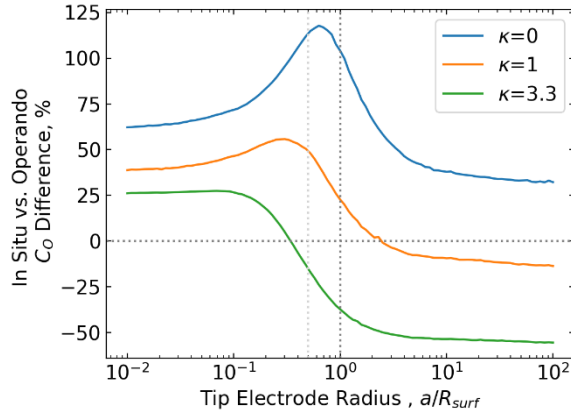


Figure 2-10: Maximum percent difference in C_O concentration, (in situ – operando)/operando, for a cone electrode at $L=1$ over a planar surface electrode, for varying electrode radius ratio and cone aspect ratio, κ , at mass transfer limited conditions. Grey dotted lines represent unity for each axis. The light grey dotted line indicates $\frac{a}{R_{surf}} = \frac{1}{2}$, used in Fig. 2-7.

concentration decreases as κ increases due to decreasing positive feedback. As the tip becomes relatively large, the diffusion of C_O away from the tip at large κ decrease the *in situ* concentration below that of the C_O operando concentration.

Concentration profile distortions due to surface electrode geometry affect the resulting tip responses to an extent that depends on tip geometry. For tip geometries such as planar electrodes, where the tip insulation is close to

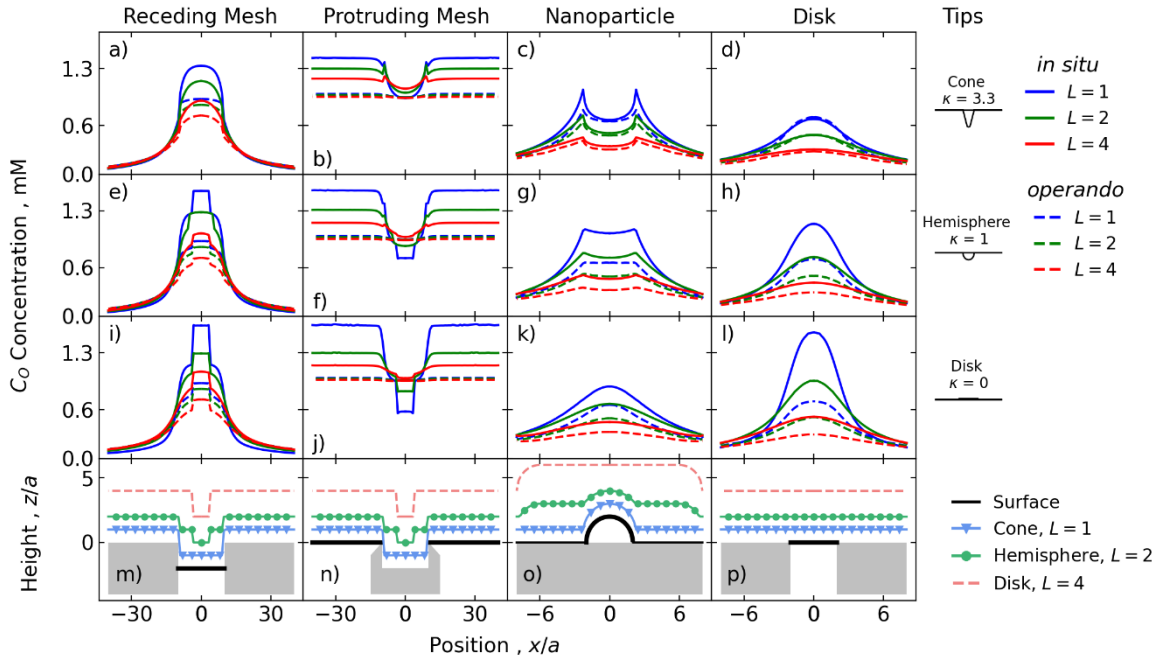


Figure 2-11: *In situ* (solid) vs. *operando* (dashed) C_O concentration profile comparison for conical, disk, and hemispherical electrodes over mesh, nanoparticle, and planar surfaces (a-l). Responses were compared at normalized separations of $L=1, 2$, and 4 , represented by blue, green and red respectively. The *in situ* response is calculated from the tip flux. The tip trajectory and surface topography are depicted in the bottom row (m-p) for each surface site and tip geometry. The active region of the surface is highlighted in bold. Tip and surface electrode fluxes are mass transfer limited.

the surface electrode, a larger distortion of the concentration field is observed. Cornut et al. has shown that varying insulation layer thickness also has an effect on the concentration profile distortion due to decreased hindered diffusion for thinner insulation layers.¹⁷⁶

Operando concentration fields near surface electrodes, calculated by the FEM model, are compared to *in situ* concentration fields, also obtained using the FEM model combined with mass transfer limited current relations (Figs. 2-11 and 2-12). In all *in situ* cases, concentration is calculated with the apex or center of the tip at the given tip position. The effect of hindered diffusion and feedback current on the response are shown by comparing concentrations at different separations ($L=1, 2, 4$), SECM tip geometry, and surface features. The mesh surface with protruding active layer and nanoparticle geometries were adapted from literature.^{331,53}

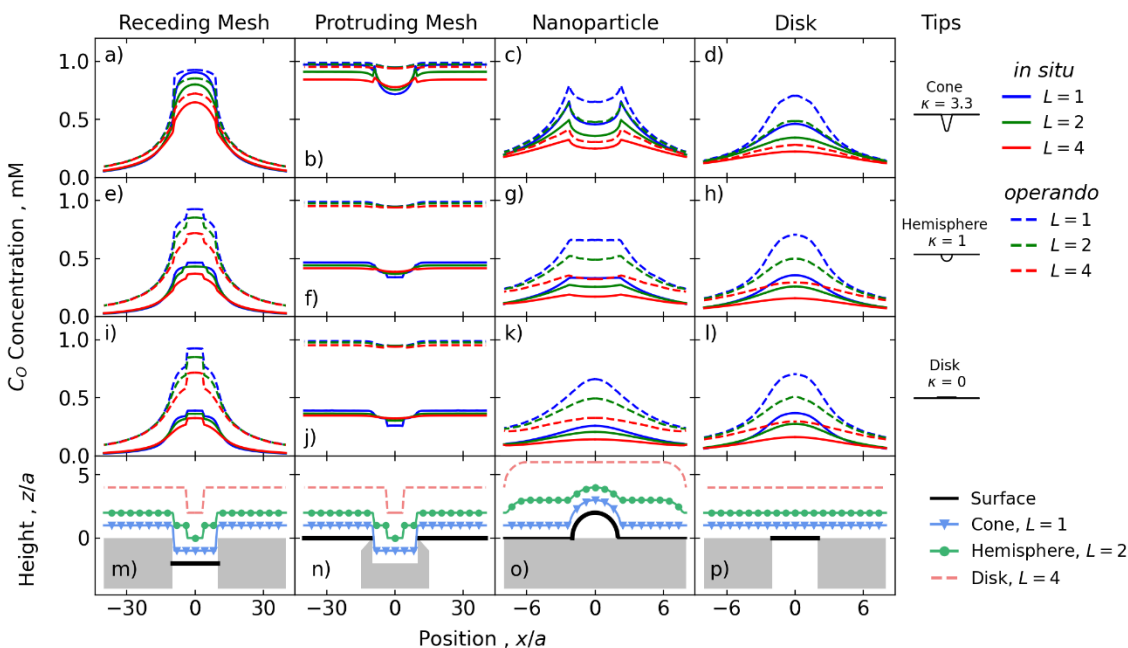


Figure 2-12: *In situ* (solid) vs. *operando* (dashed) C_O concentration profile comparison for conical (a-d), hemispherical (e-h), and disk (i-l) electrodes over mesh, nanoparticle, and planar surfaces that are kinetically limited. The *in situ* response is calculated from the tip flux. The tip trajectory and surface topography are depicted in the bottom row (m-p) for each surface site and tip geometry. The active region of the surface is highlighted in bold.

2.3.4 Kinetically limited tip in situ vs. operando response

The *in situ*

concentration profiles of kinetically limited tip responses (Fig. 2-12) use calculated tip rate constant (Table 2) for the surface and tip electrodes. This causes the calculated *in situ* concentration to underestimate the *operando* concentration. The effects of hindered diffusion are illustrated in the insulating region ($|\frac{x}{a}| > 4$) of the

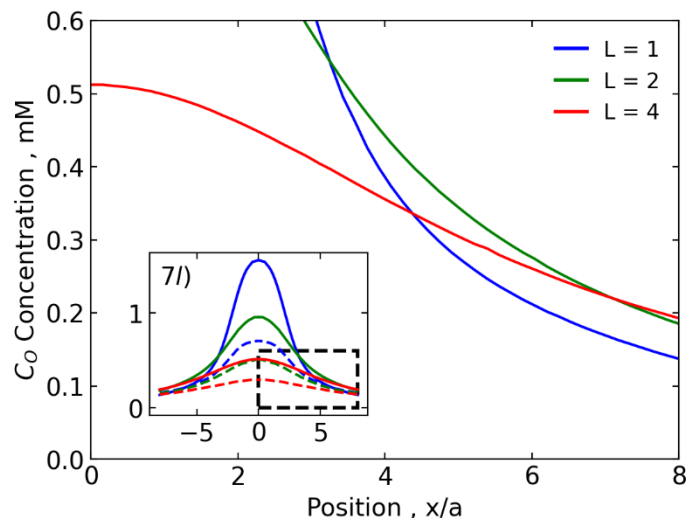


Figure 2-13: Enlarged subset of fig. 2-11l (inset) In situ (solid) C_O concentration profile comparison for a disk electrode over a planar surface under mass transfer limited conditions.

disk electrode, Fig. 2-12 column 4, where the *in situ* deviation from *operando* concentration decreases as the aspect ratio increases. Positive feedback across increasing aspect ratios decreases, due to the parts of the tip active area being further from the surface (Fig. 2-12 column 2). The kinetic limitation manifests in the *in situ* underestimation of the *operando* concentration for the disk and hemispherical tips, where the diffusion is highly hindered.

The simulated SECM tip electrode geometries are a rounded cone (Fig. 2-1),³³¹ disk, and hemisphere.¹⁷⁷ These geometries may be characterized by the tip aspect ratio, κ , where $\kappa \approx 3.3$ for the conical tip (Table 2), $\kappa = 1$ for the spherical tip, and $\kappa = 0$ for the disk geometry. The geometry for the simulation, including the tip height separation, L , is normalized by tip radius, a . The surface electrode geometries include a hemispherical nanoparticle and planar disk, each with a normalized radius of 2, and a circular mesh electrode with a normalized step height and radius of 2 and 10, respectively. The RG and κ values obtained by fitting approach curves (Table 2), are

used for calculations involving the conical tip. Mass transfer limited current was assumed in Fig. 2-11. The effect of the calculated tip rate constant, $k_{0,tip}$, is explored in Figure 2-12.

Tip electrode and insulation geometry affect the tip trajectory for constant separation SECM in the presence of surface features. For the disk tip, the electrode and insulation are coplanar, so there is, at most, one trajectory change during imaging (Fig. 2-11, row 4). The hemispherical tip height is smaller than the surface nanoparticle (Fig. 2-11 column 3) and mesh electrodes (Fig. 2-11 columns 1 and 2). When tracking the surface over the nanoparticle surface electrode, the tip trajectory changes when the tip insulation first interacts with the nanoparticle and again when the hemispherical tip electrode physically interacts with the nanoparticle (Fig. 2-11o). Over the mesh electrodes (Fig. 2-11 m, n) the tip trajectory changes when the mesh edge is first cleared by the tip electrode and then by the tip insulation. The cone tip aspect ratio is large enough that the only trajectory change occurs when the surface interacts with the tip electrode.

A planar disk surface electrode (Figs. 2-11 and 2-12, column 4) exemplifies a case where the surface active site is two-dimensional, allowing for identical tip trajectories for all 3 tip geometries (Fig. 2-11p). For the planar surface electrode, positive feedback decreases as the tip aspect ratio, κ , increases, due to the decreased fraction of tip surface area that is close to the active surface.¹⁹ The *in situ* concentration close to the insulating surface ($x/a \approx \pm 6$) dips below concentrations further from the surface, due to hindered diffusion (detail in Fig. 2-13). Reduced hindered diffusion of C_0 at large κ also reduces deviation between *in situ* and *operando* concentration profiles (Figs. 2-11 c & d). Because all tip trajectories are identical for the disk surface electrode, the *operando* concentration (dashed lines) is therefore independent of tip geometry, and variations in *in situ* response (solid lines) are strictly due to tip geometry.

A hemispherical nanoparticle surface electrode (Fig. 2-11, column 3) shows increased current over the nanoparticle due to positive feedback. The protruding surface feature decreases the hindered diffusion effect near the nanoparticle as compared to planar and recessed surface features. Tip geometries with $\kappa > 0$ (Figs. 2-11c, 11g) show flatter concentration profiles, particularly close to the surface (*i.e.*, $L = 1$), and at the apex of the nanoparticle, $x/a \approx 0$, where the SECM tip closely follows the hemispherical surface. The profile peaks near the nanoparticle edge (Fig. 2-11c), correspond to where the horizontal separation to the nanoparticle is smaller than the vertical separation, L , due to the trajectory of the tip at constant separation. The tip responses approach a constant concentration above the nanoparticle due to the constant tip-nanoparticle separation over this range, particularly at shorter separations (*i.e.*, $L = 1$).

Positive feedback causes the *in situ* response to exceed the *operando* response in most cases in Fig. 2-11. However, higher aspect ratio tip electrodes, such as the conical tip ($\kappa = 3.3$, Fig. 2-11 row 1) produce an *in situ* concentration field that more closely matches *operando*. This agrees with Fig. 2-6, where the difference for the conical electrode at $a/R_{\text{surf}} = 0.5$ is only 13%. It may be inferred that, under mass transfer limited conditions, high aspect ratio tips will often provide sufficient fidelity to *operando* concentration fields and may not require *in situ* to *operando* corrections for nanoscale features.

A mesh electrode, in which the recessed layer is inactive (Figs. 2-11 & 2-12, column 2) represents a macro electrode with a flat concentration field far from the mesh site ($x/a \approx \pm 30$). As the aspect ratio, κ , increases, the tip insulation withdraws further from the surface, decreasing hindered diffusion. As the tip crosses over the inactive recess, the local concentration dips. For the closest tip-surface separation, $L = 1$, the SECM electrode moves into the recess and moves below the surface, (Fig. 2-11 m & n). This causes further hindered diffusion, and a

decrease in calculated *in situ* concentration is observed. The degree and position of this drop depends on the tip trajectory, which is in turn a function of the tip shape.

A similar analysis can be applied to the mesh with recessed active surface (Fig. 2-11 & 2-12 column 1). When the tip electrode scans over the recessed portion of the surface, the positive feedback response is accentuated. As κ increases, the amount of positive feedback decreases, reducing the maximum calculated concentration. Jumps in the *in situ* concentration are seen when the trajectory changes height. For steady state response, with a relatively high fraction of active surface area, the *operando* concentration profile is approximately uniform.

Overall, *operando* concentration fields, unaffected by feedback modes or hindered diffusion, display fewer nonuniformities as compared to *in situ* concentration profiles. The disk surface electrode (Fig. 2-11, column 4) presents the largest concentration deviation between *in situ* and *operando* cases. For a planar surface site observed using a disk tip electrode under mass transfer limited conditions, a maximum 120% over-estimate of the C_0 concentration is observed, at the centerline (Fig. 2-11l). This is the largest deviation observed for all simulated tip and surface combinations. An 80% under-representation of the concentration by the disk tip electrode over a nanoparticle represents the largest deviation under kinetically limited tip conditions, where the surface was held under mass transfer conditions (Fig. 2-11k). Electrodes with higher aspect ratios minimize hindered diffusion and positive feedback, generally leading to a better match between *in situ* and *operando* results. Through reasonable representation of the tip and surface geometries, changes in the calculated concentration profile due to the tip trajectory can be mitigated.

2.4 Conclusions

Operando concentration profiles near nanoelectrodes, generated through a FEM simulation, are compared to *in situ* concentration profiles to identify and describe artifacts arising due to the presence of the SECM tip. In comparing simulated *in situ* and *operando* concentration fields, it was shown that the *in situ* response for surface sites similar in size to the SECM tip can significantly deviate from *operando* concentration fields. The deviation in *in situ* and *operando* concentration profiles was demonstrated using experimental SECM observations of catalysis at a nanoparticle. Calculated comparisons over varied surface and tip geometries show large deviation in concentration gradients for similarly sized electrodes.

Computationally removing these effects can alter the interpretation of experimental results. By fitting the model to experimental results, and subsequently removing experimental tip effects, we can estimate *operando* concentration of nanoelectrodes. In select cases, such as nanoparticles measured by a conical electrode, deviation of the *in situ* and *operando* nanoparticle concentration fields can be minimized experimentally. However, decreasing contamination on these AFM-SECM tips need be prioritized to ensure fidelity of large-scale scans.

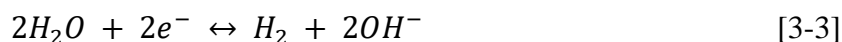
Understanding and removing tip effects will improve the interpretation of kinetic and transport studies of nanoelectrodes through accurate concentration correlations.

Chapter 3

Tip Effects in pH Probe Measurements During CO₂ Reduction‡

3.1 Introduction

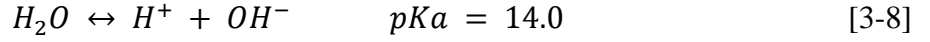
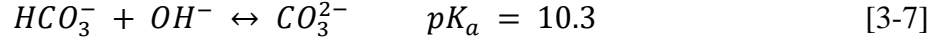
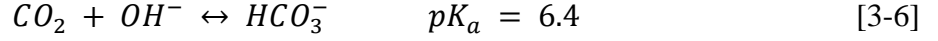
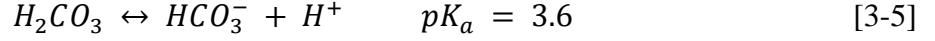
In many studies, the activity for CO₂ reduction is assessed without actual knowledge of the interfacial pH, which can vary drastically from the bulk depending on the current density, electrolyte buffer capacity, and diffusion coefficient of the species in solution. On gold, at low overpotentials, CO₂R and HER yield mainly carbon monoxide (CO) and hydrogen (H₂) through the following reactions³³²:



The interfacial pH and the overpotential will determine whether the overall HER current is dominated by proton or water reduction, displayed in Equations 3-2 and 3-3, respectively. Because of the consumption of protons or formation of OH⁻ by both HER and CO₂R, the pH near the electrode surface can drastically vary from the bulk pH. Apart from the reactions 3-1 to 3-3, various homogeneous reactions may take place in the CO₂-water system as a function of pH^{261,333–337}.



‡This chapter has, in part, been collaboratively published as: Monteiro, M. C. O.; Mirabal, A.; Jacobse, L.; Doblhoff-Dier, K.; Barton, S. C.; Koper, M. T. M. Time-Resolved Local PH Measurements during CO₂ Reduction Using Scanning Electrochemical Microscopy: Buffering and Tip Effects. *JACS Au* **2021**, *1* (11), 1915–1924.
<https://doi.org/10.1021/jacsau.1c00289>.



Our modified Au-UME pH sensor is employed in this work to perform and compare direct pH measurements during HER and CO₂R on polycrystalline gold. We monitor the evolution of pH in time while stepping the electrode potential in either argon or CO₂ atmosphere. Our results show that the homogeneous reactions involving CO₂ in aqueous media are sufficient to buffer the reaction interface to a certain extent, in spite of using an otherwise unbuffered electrolyte. The high sensitivity and time resolution of our pH probe enables us to analyze the dynamics of the diffusion layer pH as a function of the initial conditions and applied potential, which has not been previously reported for CO₂ reduction using SECM. Additionally, in this work we have accounted for the effect of the SECM tip on the diffusion layer concentration fields, and consequently on the pH measured for CO₂R and HER, using 2D, dynamic transport and reaction simulations based on Finite Element Methods (FEM). Simulations are fitted to experimental results to estimate kinetic parameters and enable further analysis of SECM tip effects relevant to the experimental system. This work brings pH measurements during CO₂ reduction one step further, by showing that it can be realized using SECM, with high time resolution and over a wide pH range. This allows for in future studies, decoupling pH effect from other electrolyte/surface effects on the reaction.

3.2 Methods

3.2.1 Finite Element Method (FEM) simulation

The experimental system is represented by a 2D axisymmetric cylindrical SECM tip and a planar working electrode at the bottom of a cylindrical cell. Geometric parameters³³⁸ are listed in Table 2-1 with a graphical depiction of the geometry in Figure 3-1.

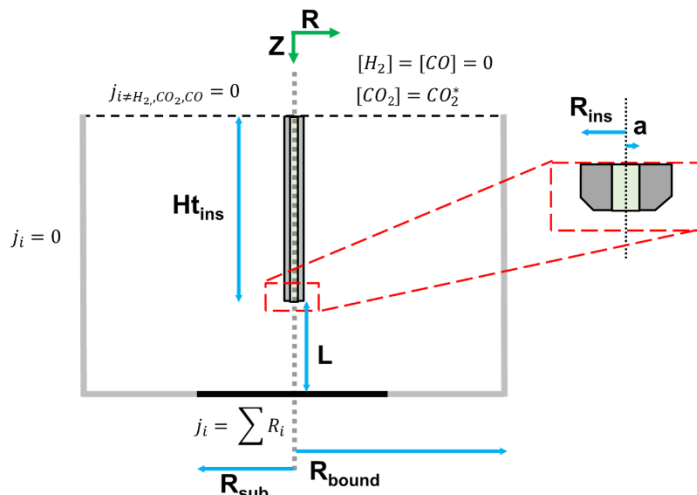


Figure 3-1: Geometric description of the experimental system with simulation boundary conditions used for hydrogen evolution and CO₂ reduction.

Table 3-1: Geometric parameters

Parameter	Value
Tip Radius (R_{tip} , μm)	25
Insulation Radius (R_{ins} , μm)	500
Working Electrode Radius (R_{sub} , mm)	5
Boundary Radius (R_{bound} , mm)	8
Normalized tip-surface separation (L)	3.4
Tip electrode height (h_{ins} , mm)	7.4

Migration and convection are neglected, and transport is governed by Fick's second law of diffusion. Proton-hydroxide ion recombination is included as a homogeneous reaction along with the carbon dioxide reversible reactions (Equations 3-4 – 3-7). The governing equations are:

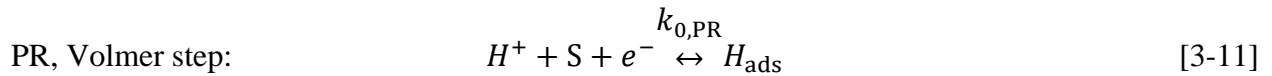
$$\frac{dC_i}{dt} = D_i \nabla^2 C_i + \sum R_{ij} \quad [3-9]$$

where C_i is the concentration of each species in solution (H^+ , OH^- , H_2O , H_2 , Li^+ , and SO_4^{2-}), D_i is the species diffusion coefficient, and the reversible reaction rates, R_{ij} , for each species, i , are summed for each reversible reaction, j .

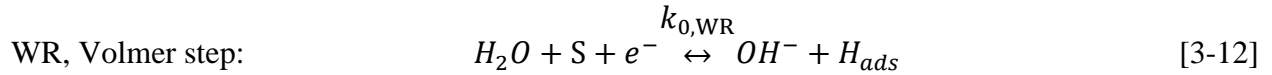
The boundary conditions, visually represented in Figure 3-1, are as follows: At the WE surface ($z = 0$), a flux balance is applied using the electrode reaction:

$$-D \nabla C_i \cdot \vec{n} = \sum_j r_{ij} \quad [3-10]$$

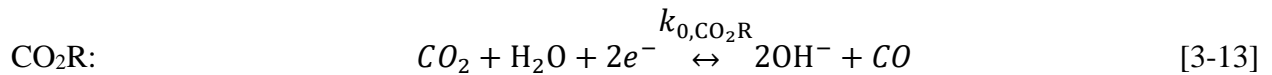
where \vec{n} is the surface normal. The summation is over all surface reactions, j , and r_{ij} is the rate of production of species i due to reaction j ; $\sum r_{ij}$ is the summation of the reactions involving a given species, i . Proton reduction (PR), water reduction (WR) and carbon dioxide reduction (CO_2R , Eq. 3-13) are considered at the substrate. Proton reduction and water reduction rates are assumed to be limited by Volmer adsorption of hydrogen (Equations 3-11 and 3-12, respectively, E_{app} is an arbitrary reference potential for the first reaction step).^{339,340}



$$E_{app} = 0 \text{ V vs. SHE at } pH = 0$$



$$E_{app} = 0 \text{ V vs SHE at } pH = 0$$



$$E_0 = -0.52 \text{ V vs SHE at pH} = 7$$

The rates of PR and WR, due to the large overpotentials, were expressed by Tafel kinetics. CO₂R was expressed in Butler-Volmer form:

$$r_{\text{PR}} = k_{0,\text{PR}}(C_{\text{H}^+} \exp(-\alpha_{\text{PR}}n_{\text{PR}}f\eta_{\text{PR}})) \quad [3-14]$$

$$r_{\text{WR}} = k_{0,\text{WR}}(C_{\text{H}_2\text{O}} \exp(-\alpha_{\text{WR}}n_{\text{WR}}f\eta_{\text{WR}})) \quad [3-15]$$

$$r_{\text{CO}_2\text{R}} = k_{0,\text{CO}_2\text{R}} \left(C_{\text{CO}_2\text{R}} C_{\text{H}^+}^2 \exp(-\alpha_{\text{CO}_2\text{R}}n_{\text{CO}_2\text{R}}f\eta_{\text{CO}_2\text{R}}) - C_{\text{H}_2\text{O}} C_{\text{CO}} \exp((1 - \alpha_{\text{CO}_2\text{R}})n_{\text{CO}_2\text{R}}f\eta_{\text{CO}_2\text{R}}) \right) \quad [3-16]$$

where $k_{0,j}$ are the rate constants, the number of electrons is n_j , the charge transfer coefficient is α_j , and $\eta_j = E - E_{0,j}$, where the $E_{0,j}$ are the formal potentials and E is the applied surface potential. Finally, $f = \frac{F}{RT}$, where F is Faraday's constant, R is the gas constant and T is the temperature.

Three surface reactions occur simultaneously at the gold surface electrode. At the liquid-atmosphere boundary ($z = L + ht_{\text{ins}}$), the concentration of molecular hydrogen, H₂, is zero (Fig. 3), the bulk concentration of CO₂ is set to 0 (under Ar) or 10 mM (under CO₂), and flux is set to zero for all other species. This bulk CO₂ concentration, which is roughly half of the estimated saturation concentration (23 mM, for 1 atm CO₂ in 0.1 M Li₂SO₄ at pH 3 and 25 C), was chosen to avoid numerical convergence issues at higher concentrations.

At all other boundaries, a zero-flux condition is imposed for all species. Diffusivities used in the simulation are listed in Table 3-2 with the equilibrium and dissociation constants for the reversible reactions. Kinetic rate constants for the homogeneous dissociation reactions were

obtained from Wuttig et al.³³³ and Bohra et al.³³⁶ The tip electrode proton adsorption is assumed to have negligible effects on the pH.

3.3 Results

3.3.1 pH Sensor Synthesis and Calibration

The gold ultramicroelectrodes (Au-UMEs) are first characterized by blank voltammetry in 0.1 M H₂SO₄ in order to ensure good sealing and surface cleanliness. In order to perform the SECM pH measurements, the Au-UME is functionalized with the 4-hydroxylaminothiophenol/4-nitrosothiophenol redox couple. This is done by immersion of the Au-UME in a solution containing 4-nitrothiophenol (4-NTP), which leads to the self-assembly of this organic molecule on the Au-UME surface. Next, 4-NTP is partially (30) electrochemically reduced to 4-hydroxylaminothiophenol (4-HATP) in 0.1 M H₂SO₄, as depicted in Figure 1a. The cathodic potential limit must be carefully controlled in order to maximize the conversion to 4-HATP and minimize the amount of 4-aminothiophenol (4-ATP) formed. On the positive-going scan, an

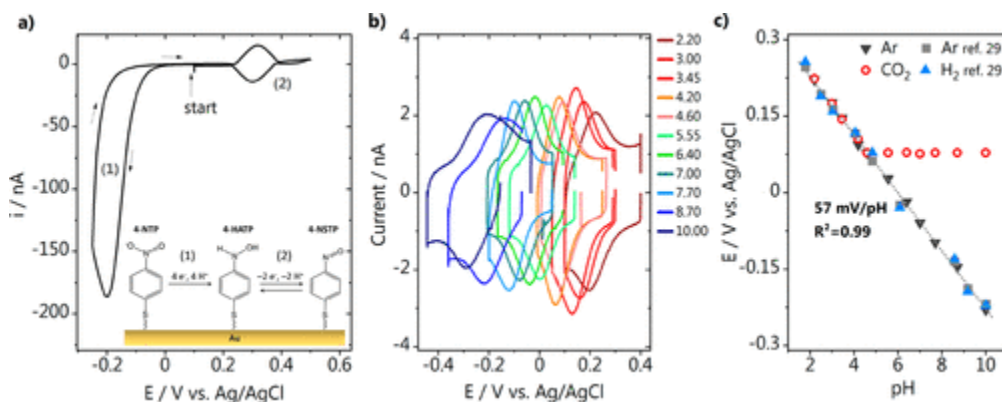


Figure 3-2: SECM pH sensor synthesis and calibration. (a) Voltammogram of the functionalized Au-UME showing the conversion of 4-nitrothiophenol (4-NTP) to the pH sensitive redox couple 4-hydroxylaminothiophenol (4-HATP)/4-nitrosothiophenol(4-NTP); (b) pH sensor voltammetry in 0.1 M Li₂SO₄ solutions adjusted to different pH, taken at 200 mV s⁻¹; (c) Calibration curves of the modified Au-UME pH sensor in different gaseous atmospheres. The calibration curves from our collaborator's previous work [305] are also shown for comparison.

anodic peak can be seen in the gold double layer region between 0.2 and 0.4 V vs Ag/AgCl due to oxidation of 4-HATP, forming 4-nitrosothiophenol (4-NSTP). This is a highly reversible reaction, demonstrated by the subsequent symmetrical cathodic current in the negative-going scan. A schematic representation of the reactions taking place at the Au-UME surface can be seen in the inset of Figure 3-2a, which is correlated to the voltammetry of (1) the reduction of 4-NSTP to 4-HATP and (2) the 4-HATP/4-NSTP redox couple.

The calibration of the functionalized Au-UME pH sensor is performed in the same electrolyte the SECM measurements are carried out, but in different gaseous atmospheres. The cyclic voltammetry (CV) of the tip is recorded in 0.1 M Li₂SO₄ solutions adjusted to different pH and saturated with either argon or CO₂. The CVs obtained in argon are shown in Figure 3-2b. The midpeak potential of the 4-HATP/4-NSTP anodic voltammetry is obtained through a Gaussian fit (with a linear background) of the CVs and can be used to construct the calibration curve shown in Figure 3-2c. Because of the reversible oxidation and reduction of the 4-HATP/4-NSTP involving two protons and two electrons, a Nernstian response is obtained with a shift of 57 mV/pH unit and an R^2 of 0.99. The calibration curves in argon and CO₂ atmosphere overlap until pH 3.45. This is expected as at higher pH values, carbonic acid is formed and the CO₂ saturated solutions equilibrate at a constant pH around 4 (see eqs 4 and 5). We have also displayed the calibration curves presented in our previous work³⁰⁶ in Figure 3-2c, which show how reproducible the pH sensor response is when comparing different measurements, performed in different gaseous atmospheres.

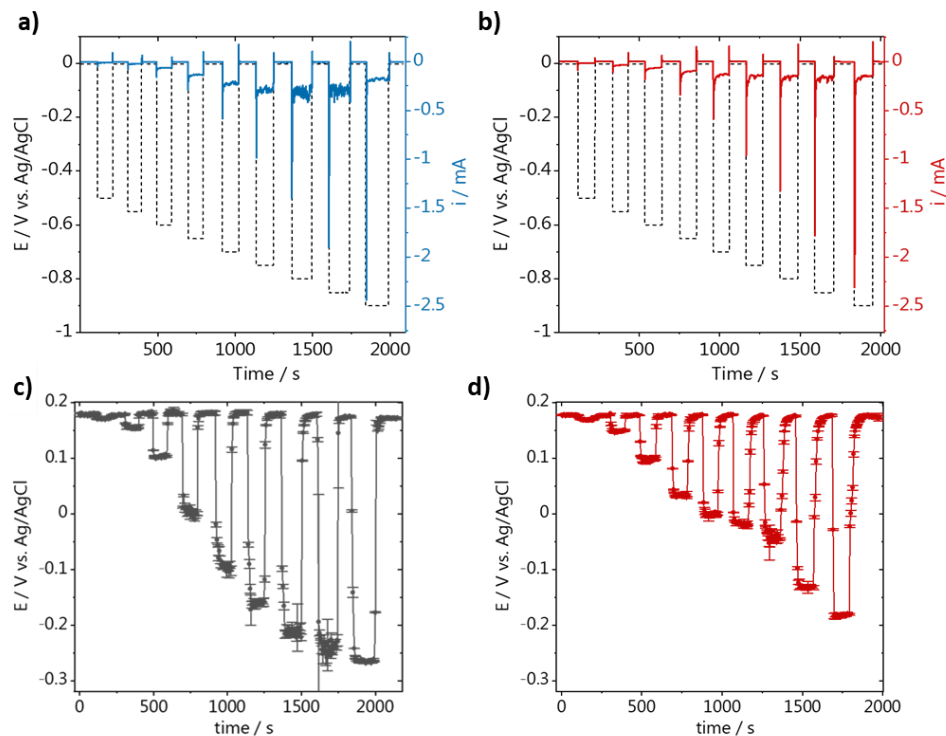


Figure 3-3: Chronoamperometric surface electrode (gold) current over 100s as a function of the surface electrode potential under argon (a) and CO₂ (b) gas sparging in 0.1 M Li₂SO₄. The applied surface potential is stepwise controlled as a function of time (grey dotted line). The corresponding peak potentials at the tip pH electrode follow (c-d).

Electrochemical reduction reactions were studied under chronoamperometry, where the potential was held constant for 100 s. Between each potential, the sample was turned “off” by holding the potential at 0 V. The potential was linearly incremented in 50 mV steps from -0.5 V to -0.9 V vs. Ag|AgCl, encapsulating the onset to peak potential of the 1st cycle of a CV response under argon (Figure 3-4). To quantify the changes in pH in the diffusion layer during these reactions using SECM, the functionalized Au-UME pH sensor is placed at a constant distance of $80 \pm 2 \mu\text{m}$ from the gold surface. The tip voltammetry is constantly recorded at 200 mV s^{-1} , which allows capturing the changes in pH with high time resolution (4 s/data point). Figure 3-3 shows the results obtained in argon atmosphere (c) and then in CO₂ atmosphere (d). These data were obtained in two consecutive measurements and are plotted on top of each other to facilitate

comparison. The peak potentials obtained from fitting the 4-HATP/4-NSTP voltammetry (used to extract these pH data) and the current recorded at the sample during the chronoamperometry can be found in the publication.³⁴¹ From the results in Figure 3-3c-d, it can be seen that at low overpotentials and consequently low current densities (between -0.5 and -0.6 V), small pH changes of maximum 1.5 pH unit are observed at the interface, both in argon and CO₂ atmosphere. At these potentials (and pH) proton reduction is the main reaction taking place, and the activity for CO₂R is still quite low. Although proton reduction is kinetically limited in this narrow potential window, the low proton bulk concentration (pH 3), explains the relatively small effect on the measured pH. The significant pH change we observe even when the reaction appears kinetically limited is related to the presence of the tip, which inhibits local mass transport, as we will later illustrate in the Finite Element modeling section. Between -0.65 and -0.9 V vs. Ag/AgCl, however, the pH recorded in argon atmosphere gradually increases as a function of potential. At these higher interfacial pH values, hydrogen is produced through the reduction of water. As water reduction is a kinetically limited reaction producing OH⁻, the alkalinity is expected to increase with the potential. In CO₂ atmosphere, between -0.65 and -0.8 V vs. Ag/AgCl, we observe that the pH does not significantly increase as the potential is scanned more negatively, although we work in an unbuffered electrolyte. When the pH at the interface becomes alkaline, the reversible reaction between CO₂ and HCO₃⁻ (pK_a = 6.4, Equation 3-6) seems to take place fast enough, so that the CO₂ supplied is not only a reactant but also acts as a buffer to a certain extent. Once potentials more negative than -0.8 V are applied there is a buffer “breakdown” and the pH increases more than a unit above the pK_a of the CO₂/HCO₃⁻ reversible reaction. In fact, this buffering can also be observed in CO₂ atmosphere at lower overpotentials, where the maximum pH reached is still below 6. Interestingly, once the reaction

is turned “on”, there is first an increase in pH that reaches a maximum value after 30-35 seconds. Subsequently, the pH decreases as the OH^- produced are neutralized by the forward $\text{CO}_2/\text{HCO}_3^-$ reaction (Equation 3-6).

3.3.2 Finite Element Simulations

Simulations were completed using COMSOL Multiphysics with transport of dilute species. A triangular mesh was used with an increased resolution surrounding the surface and tip electrodes. All species were included in the simulation and the properties defined below were used to describe the transport and reactivity of each species.

3.3.2.1 Hydrogen evolution reaction kinetics

The hydrogen evolution reaction is simulated by solving Equations 3-11 and 3-12 shown in the Experimental Section. The use of Equation 3-11 to calculate initial proton reduction kinetic rate parameters is justified by the Tafel slope of 147 mV/dec, indicating that a Volmer or large overpotential Heyrovsky steps are likely the rate limiting step.³³⁹ When the reduction reaction is largely irreversible, the Heyrovsky response approaches that of the Volmer. Initial guesses of α_p and $k_{0,PR}$ were determined from the Tafel plot (see Figure 3-5) and $E_0 = 0$ V vs. SHE at pH 0. Subsequently, kinetic parameters for proton reduction (PR) appearing in Eq. 3-11, were obtained from fitting to cyclic voltammetric data, specifically the reductive

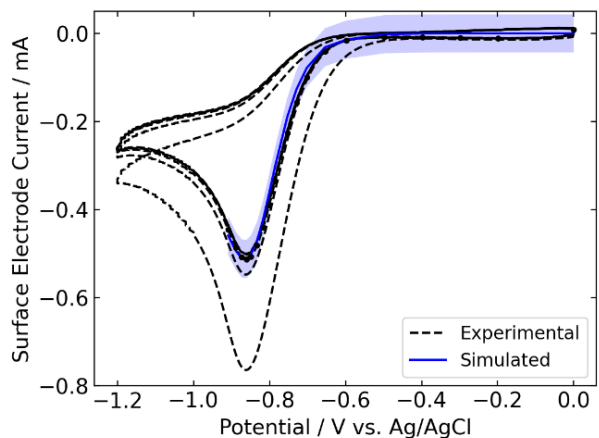


Figure 3-4: 100 mV/s cyclic voltammogram on the gold surface electrode under argon saturation in 0.1 M Li_2SO_4 . Experimental results (black) are compared to FEM simulation results (blue) with the proton reduction rate constant fit to the 3rd cycle (blue line) with a 95% confidence interval.

peak of the third cathodic sweep under argon (Figure 3-4) over a potential range from 0 to 0.9 V vs. Ag/AgCl. We expect this CV current to be mainly due to proton reduction and not water reduction, because of the fast potential sweep rate (100 mV/s) and low bulk pH. During a CV cycle, the surface pH remains below 6.5, supporting this assumption. The resulting parameters for α_p ,

$k_{0,PR}$, D_{H^+} and n_p are listed in Table 3-2, where the calculated charge transfer coefficient ($\alpha_p = 0.41$) agrees with the result obtained from the Tafel slope in Figure 3-5. The cyclic voltammetry reaches mass transfer limited conditions due to its low activity for HER and CO_2R ,³⁴² which allows for a broad potential window.

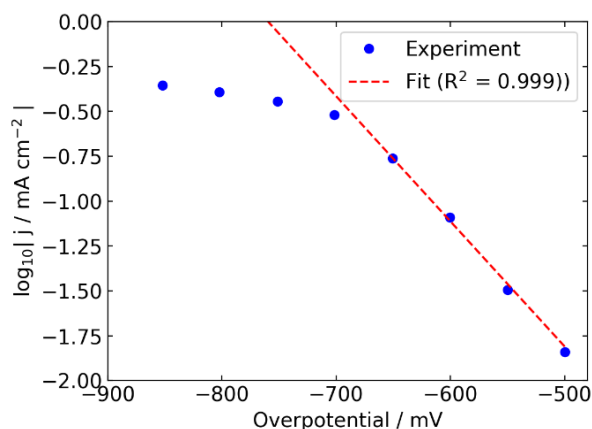


Figure 3-5: Tafel slope for HER at pH 3 extracted from the chronoamperometry (Fig3-2a) experiment using the 4 lowest overpotential values.

Table 3-2: Kinetic parameters estimated by fit to the Tafel plot (Figure 3-5), the cyclic voltammogram (Figure 3-4), or the pH-V relation (see Figure 3-9a). Values that were fixed and not fitted are marked with a star (*).

Parameter	Tafel (Fig. S7)	CV Fit (Fig. S8)	pH-V Fit (Fig. 6)	Literature	Ref.
$k_{0,PR}$ [cm/s]	$4.2E-8 \pm 1.8E-8$	$3.8E-8 \pm 1.8E-8$	-	$1E-6-1E-10$	343-346
α_{PR}	0.41 ± 0.01	0.43 ± 0.03	-	-	-
n_{PR}	-	1.3 ± 0.01	-	-	-
$E_{0,PR}$ [V vs. SHE]	0*	0*	0*		
D_{H^+} [cm ² /s]	-	$1.4E-5 \pm 5.5E-6$	-	$9.3E-5$	333
$k_{0,WR}$ [cm/s]	-	-	$3E-14 \pm 2E-14$	-	-
α_{WR}	-	-	0.5*		
n_{WR}	-	-	1*		
$E_{0,PR}$ [V vs. SHE]	-	-	0*		
D_{OH^-} [cm ² /s]	-	-	$5.3E-5^*$		347
R^2	0.999	0.993	0.976	-	-

After having fit the cyclic voltammogram, the rate constant for the water reduction reaction, $k_{0,WR}$, described by Equation 16 (Experimental Section) was obtained by fitting the pH – voltage relation shown in Figure 3-9. All other parameters appearing in Eq. 16, were set to the values given in Table 3-2. For comparison to experiment, the pH values were averaged over the SECM

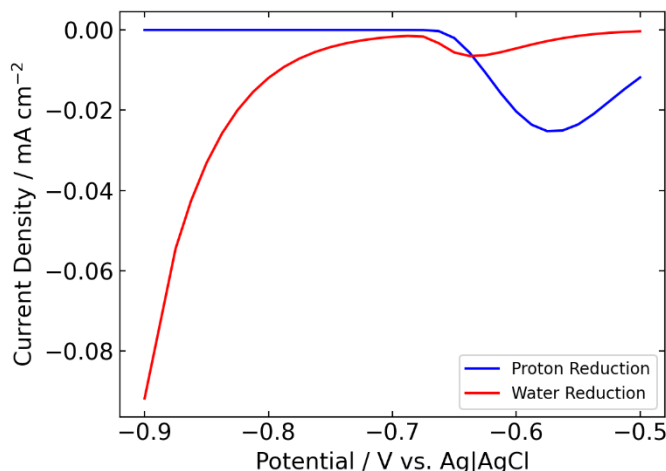


Figure 3-6: Calculated contributions of the local chronoamperometric current density at the gold electrode and beneath the SECM tip ($x=0 \rightarrow a$), due to proton (blue) and water (red) reduction. Current density is calculated from average flux of each species over 25 μm (a) from the center of the surface electrode, which is below the SECM tip electrode.

electrode area. During the optimization of $k_{0,WR}$, the parameters obtained for the hydrogen evolution reaction were kept constant. As the pH response is largely dominated by the water reduction reaction at potentials more negative than -0.65 V vs. Ag/AgCl (Figure 3-6), keeping the hydrogen evolution reaction parameters fixed, is a reasonable approach. Because of this, only the water reduction rate constant ($k_{0,w} = 3\text{E-}14 \pm 2\text{E-}14 \text{ cm/s}$) was fit for this data set. With an R_2 value of 0.976, the simulation results shown in Figure 3-9a match reasonably well with the experimental results, except at the potential of -0.65 V vs. Ag/AgCl, where the simulation underestimates the pH change. The water reduction current at the portion of the surface electrode directly below the surface ($r = 0\text{-}R_{\text{tip}}$, $z = 0$) reaches a local maximum at -0.65 V vs. RHE due to the large pH increase (OH^- accumulation) directly below the tip (see Fig. 6). This hydroxide accumulation drives a decrease in the water reduction rate directly below the SECM tip.

3.3.2.2 CO₂ reduction reaction kinetics:

The electrochemical reduction of CO₂ is described by Eq. 17 in the Experimental section. The relevant parameters, which are listed in Table S2, are either set to the theoretical values or taken from literature. Homogeneous reactions are represented by the below rate laws (Equations 3-17 – 3-23). The values for the equilibrium, K_i , and dissociation rate constants, k_{-i} , are listed in Table 3-2.

$$-r_{s1*H_2O} = K_1 * k_{-1}C_{CO_2}C_{H_2O} - k_{-1}C_{H_2CO_3} \quad [3-17]$$

$$-r_{s2*H_2CO_3} = K_2 * k_{-2}C_{H_2CO_3} - k_{-2}C_{HCO_3^-}C_{H^+} \quad [3-18]$$

$$-r_{s3*OH^-} = K_3 * k_{-3}C_{CO_2}C_{OH^-} - k_{-3}C_{HCO_3^-} \quad [3-19]$$

$$-r_{s4*OH^-} = K_4 * k_{-4}C_{HCO_3^-}C_{OH^-} - k_{-4}C_{CO_3^{2-}} \quad [3-20]$$

$$-r_{s5*H^+} = K_5 * k_{-5}C_{H^+}C_{OH^-} - k_{-5}C_{H_2O} \quad [3-21]$$

$$-r_{s6*HCO_3^-} = K_6 * k_{-6}C_{HCO_3^-} - k_{-6}C_{CO_3^{2-}}C_{H^+} \quad [3-22]$$

$$-r_{s7*H_2O} = K_7 * k_{-7}C_{CO_2}C_{H_2O} - k_{-7}C_{H^+}C_{HCO_3^-} \quad [3-23]$$

Table 3-3: FEM system parameters. Values for proton reduction and water reduction are given in Table 3-2.

Variable	Value	Reference
$D_{\text{H}_2} , \text{cm}^2 \text{s}^{-1}$	5.5E-5	348
$D_{\text{H}_2\text{O}} , \text{cm}^2 \text{s}^{-1}$	2.2E-5	349
$D_{\text{Li}^+} , \text{cm}^2 \text{s}^{-1}$	1.0E-5	350
$D_{\text{SO}_4^{2-}} , \text{cm}^2 \text{s}^{-1}$	2.0E-5	348
$*D_{\text{H}^+} , \text{cm}^2 \text{s}^{-1}$	9.3E-5	333
$D_{\text{OH}^-} , \text{cm}^2 \text{s}^{-1}$	5.3E-5	347
$D_{\text{HSO}_4^-} , \text{cm}^2 \text{s}^{-1}$	2.3E-5	333
$D_{\text{CO}_2} , \text{cm}^2 \text{s}^{-1}$	1.7E-5	333
$D_{\text{CO}} , \text{cm}^2 \text{s}^{-1}$	1.6E-5	333
$D_{\text{HCO}_3^-} , \text{cm}^2 \text{s}^{-1}$	1.0E-5	333
$D_{\text{CO}_3^{2-}} , \text{cm}^2 \text{s}^{-1}$	8.0E-6	333
$D_{\text{H}_2\text{CO}_3} , \text{cm}^2 \text{s}^{-1}$	3.5E-5	333
K_1	2.6E-3	333,351,352
k_{-1} , s^{-1}	2E4	333
K_2 , M	1.7E-4	333,351
$k_{-2} , \text{M}^{-1} \text{s}^{-1}$	1E12	333
K_3 , M^{-1}	4E7	336,351,352
k_{-3} , s^{-1}	5E-5	336
K_4 , M^{-1}	1.7E3	336,352
$k_{-4} , \text{M}^{-1} \text{s}^{-1}$	1E6	336
K_5 , M^2	1E-14	335,336
$k_{-5} , \text{M}^{-1} \text{s}^{-1}$	2E9	335,336

Table 3-3 (cont'd)

K_6 , M	5E-11	333,335,336
k_{-6} , M⁻¹ s⁻¹	1E12	333,335,353
K_7 , M	4.4E-7	335,352
k_{-7} , M⁻¹ s⁻¹	9E4	352
$k_{0,\text{CO}_2\text{R}}$, cm s⁻¹	1E-15	
$\alpha_{\text{CO}_2\text{R}}$	0.5	
$n_{\text{CO}_2\text{R}}$	2	
$E_{0,\text{CO}_2\text{R}}$ [V vs. SHE]	-0.11	

*see Table 3-2 for fitted value used in FEM simulations

3.3.2.3 Finite Element Method (FEM) simulations

In SECM it is known that the tip may physically block the diffusion of species and alter their concentrations in the diffusion layer, thus influencing the pH measurement.³⁵⁴ In order to account for this effect, we have simulated the experimental results presented in Figure 3-3 (and summarized in Figure 3-9) using Finite Element Method based modeling implemented in COMSOL Multiphysics. Fitted kinetic parameters and the use of a 2D axisymmetric model leads to good agreement between simulated and experimental results. This enables us to quantify the local pH excluding the effect of the SECM tip.

First, we considered the pH response during reactions taking place in argon atmosphere (Figure 3-3 c-d), namely proton reduction (PR) and water reduction (WR). The PR rate is assumed to be linear in the proton concentration, as is the case if the Volmer step or a large-overpotential Heyrovsky step is rate limiting. This assumption is justified by the Tafel slope obtained from chronoamperometry being 147 mV/dec (see Figure 3-5)³³⁹ The kinetic parameters

for proton reduction, as well as the proton diffusion coefficient were obtained by fitting the cyclic voltammetry (Figure 3-4, argon). Subsequently, the pH-potential relation (Figure 3-9a, argon) after 100s chronoamperometry was fit to obtain kinetic parameters for water reduction. For comparison to experiment, the pH values were thereby averaged over the SECM electrode area. Relevant diffusion coefficients (except the proton diffusion coefficient) and the rate constant for water association were thereby taken from literature (see Table S2).

The fitted parameters can be used to simulate the pH map during hydrogen evolution after 100s chronoamperometry with and without tip present and hence to investigate the influence of the tip on the pH measurements. As an example, we show the pH map obtained at a substrate potential of -0.8 V vs. Ag/AgCl with and without the probe tip positioned at 80 μm above the surface in Figure 3-7. The pH maps shown demonstrate that the tip significantly blocks

diffusion of species away from the electrode surface. However, this effect is highly localized to the gap below the SECM tip; at horizontal positions far from the tip, the concentration profile approaches the “without tip” conditions.

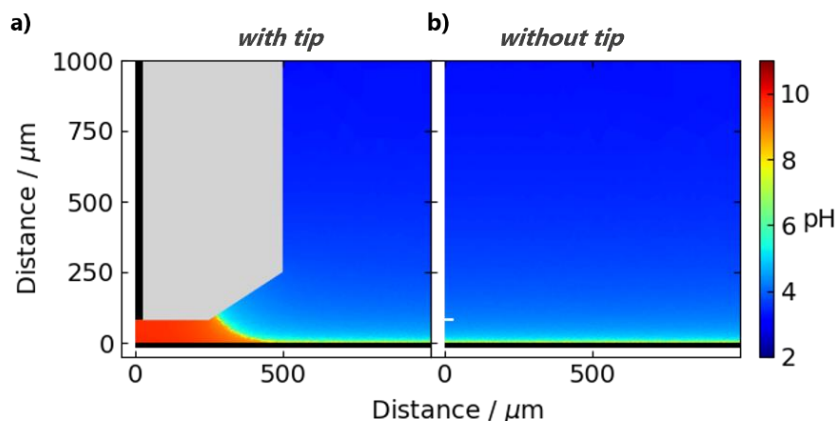


Figure 3-7: pH profile near the electrode surface during HER a) with and b) without the SECM tip present. Sample potential applied -0.8 V vs. Ag/AgCl in 0.1 M Li_2SO_4 .

Similar calculations can also be performed to estimate the influence the tip has on the transient chronoamperometry data. In Figure 3-9, we simulate the potential dependent chronoamperometry data at 100 seconds with and without tip present (solid vs. dashed line). Under argon (Figure 3-9a), as the surface electrode is poised at more negative potentials, HER

and the local pH increases. The concentration of protons estimated with the tip absent is significantly higher than that obtained with the tip present, especially at potentials between -0.65 and -0.85 V vs. Ag/AgCl. At low overpotentials without the SECM tip present, the pH gradients are minimal. Only at large overpotentials, proton consumption at the surface electrode combined with increased hydroxide production due to the onset of water reduction causes the pH boundary layer to grow to a size comparable to the tip-surface separation (see Figure 3-8). In the presence of the SECM tip, hindered diffusion directly below the tip causes the pH to rise more gradually already at a much less reducing potential. The sudden raise in pH between overpotentials of -0.6 to -0.7 V vs. Ag/AgCl can be ascribed to a switch from proton reduction to mainly water reduction, as shown in Figure 3-6.

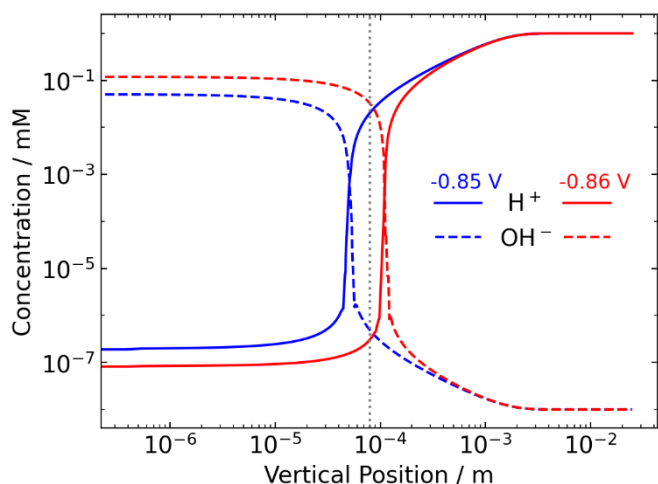


Figure 3-8: H^+ (solid) and OH^- (dashed) vertical concentration profiles during HER under argon saturation as the boundary layer approaches the tip position (dotted grey line). Surface electrode potentials of -0.850 V (blue) and -0.8625 V (red) vs. Ag/AgCl demonstrate growth of the boundary layer beyond the position of the tip electrode.

A similar analysis was performed for the measurement in CO_2 atmosphere (Figure 3-9b). (See Equations 3-17 – 3-23 for the governing electrochemical equations for the governing equations of the additional homogeneous equations. Table 3-3 lists the relevant parameters). The pH measured at the tip increases with increasing overpotential. At medium overpotentials, the tip pH plateaus near pH=7. Although no additional fit was performed, the simulation data (solid line) resembles the experimental results (red dots). Comparing Figure 3-9a and b, it becomes

clear that the pH measured in CO₂ atmosphere remains lower than that measured in argon atmosphere over the entire potential range. This is a consequence of the buffering effect of the

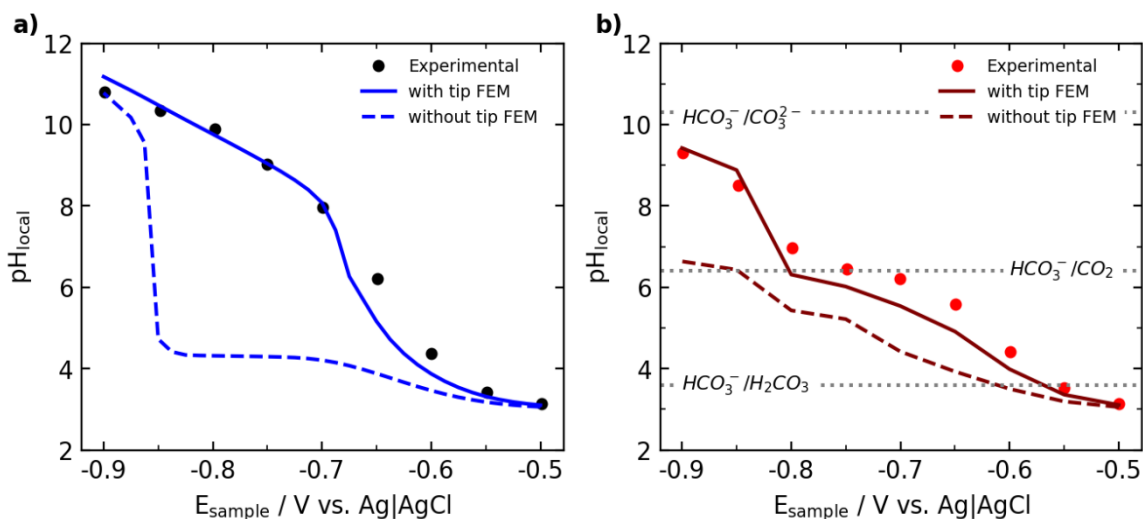


Figure 3-9: Effect of the probe on the local pH response under a) argon and b) CO₂ as a function of the surface potential. pH–potential comparisons of experimental results in argon (black dots) and FEM simulation results (blue line) for $L=3.4$ (close to the surface), compared to the pH at $z/a=3.4$ when the tip is far from the surface ($L = 50$, blue dashed line). The simulated pH ‘without tip’ is obtained from a cross section at 80 μm from the surface with the tip removed to 1.25 mm from the surface ($L = 50$); L is the normalized tip-surface separation (see Experimental Section). b) Similarly, experimental (red dots) and simulation (dark red line) pH under CO₂ reduction for $L = 3.4$, is compared to simulated $L = 50$ (dark red dashed line). Bulk CO₂ concentration was fixed at 10 mM.

CO₂ species present, as evidenced by the two plateau regions in the pH–potential relation, which correlate to the pK_a of bicarbonate (Equation 3-6) and carbonate (Equation 3-7). Although the buffering effect of the CO₂ species is most striking in the presence of the tip, the buffering of the electrolyte is also relevant in the absence of the tip. This is evidenced by the shift of the sudden increase in pH observed in argon atmosphere at -0.85V to even more negative potentials (not plotted). The presence of CO₂ and its derivatives thus has a significant buffering effect near the electrode at experimentally relevant conditions in both the presence and the absence of the tip.

Hindering the diffusion and inducing a high local alkalinity at the reaction interface allowed us to study the diffusion layer during CO₂R at relatively low sample potentials (and current densities), which circumvents e.g. bubble issues and allows for gradually modulating the

pH below the tip. However, this tip blocking effect could of course be minimized by decreasing the radius of the tip insulating layer or by working at larger distances from the surface. Using calculations similar to those shown in Figure 3-9a, we have simulated the effect of decreasing the radius of the tip insulation on the pH response.

Figure 3-10 shows the results of the FEM simulations carried out using different insulating radii from $20 \cdot a$ (the experimental value, a from the UME used in this work)

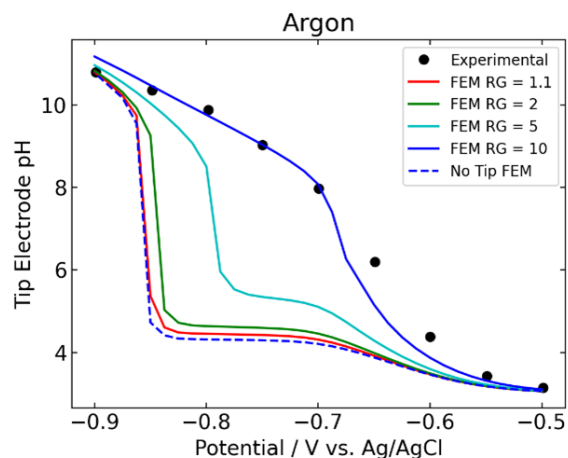


Figure 3-10: Minimization of tip effects by decreasing the insulation radius.

Comparison is made for the experiment in argon, using the results from Figure 3-9a, and simulations decreasing the insulation radii, with a constant a . The bottom tip insulation radius is maintained at $\frac{1}{2} R_{ins}$ (see Figure 3-1 in the Experimental Section). (0.1 M Li_2SO_4 , $L=3.4$, and $R_{surf} = 5\text{mm}$).

down to $1.2 \cdot a$, for a constant tip-sample distance. The simulated pH response in the absence of the SECM tip is also plotted for comparison. It can be seen that for an ideal insulation layer radius of $1.2 \cdot a$ the calculated pH values closely approach those obtained without the tip present. When desired, this situation can be achieved, for example, by using a laser puller to produce the microelectrodes. However, it is important to point out that we find that obtaining a good sealing between the gold and the glass can be challenging, contrary to other metals that have a better adhesion to the insulation layer, like platinum. Alternatively, decreasing the radius of the tip (a) will also decrease the diffusion hindrance and change the profiles shown in Figure 3-10.

3.4 Conclusions

The potential dependency of the local pH during HER and CO_2R is shown to be influenced by buffering of carbonate species. Moreover, the local pH measurements is shown to

vary by ~8 pH units as compared to bulk values. This is indicative of the importance of the local pH versus the bulk pH for deciphering pH influence on CO₂R selectivity and reactivity. We demonstrate that at medium overpotentials, it is essential to account for the effect of the probe on the proton concentration.

Coupling SECM measurements with FEM simulations is a resourceful way to account for the physical blocking effect that the SECM probe has on interfacial concentration profiles. Our case is concerned with proton concentration, but the approach also applies to the detection of other species in solution, participating or not in a catalytic reaction. On the other hand, this hindrance of diffusion can also be intentionally introduced to induce a high local alkalinity in a controlled fashion, and allow the study of homogeneous and inhomogeneous reactions taking place in the diffusion layer, as shown in this and our other recent work.²⁹¹

Chapter 4

Tip Effects in pH Probe Measurements During CO₂ Reduction

4.1 Introduction:

CO₂ reduction reaction conditions generate local gradients of protons and buffering species. In this work we fit experimental local pH measurements to parameterize a simulation that shows the carbonate species and pH variance as a function of distance from the surface in an unbuffered system. Previously, Dr. Gewirth's group has shown that the pH has impact on the local carbonate species concentration, and therefore the reactivity.³⁵⁵ In the growing range of nanoscale catalysts, it would therefore be advantageous to analyze the local pH and then use a compatible simulation to explore the local species. Reactions at gold and silver electrodes poised at cathodic potentials commonly undergo the reactions previously described (Eqs 3-1 – 3-3), namely HER and CO₂R with CO as a product.

We have previously shown that hindered diffusion qualitatively equilibrates the pH at the surface with the probe at high kinetic rates and long time scales.³⁵⁶ Given the geometric parameters of the probe (R_{ins}), the separation between the surface and tip electrodes (L) and the surface electrode radius (R_{surf}), the pH at the surface and the surrounding local environment can be calculated. Sensitivity to these parameters also guides kinetic studies, suggesting the potential range in which a given configuration gives optimal pH sensitivity. In doing so, experiments can be guided toward specific mechanisms for product formation. Using simulations, we suggest how to optimize the tip radius and separation for a given electrode size within practicality.

In this work we proactively examine the separation (L), insulation radius (R_{ins}), surface electrode size (R_{surf}), and the CO₂ and buffer concentrations and their effects in guiding experiments. This is in contrast with our previous reactive work used to analyze already

generated experimental results. We discuss the optimal geometric parameters with consideration of the sensitivity of the experimental conditions (i.e., surface electrode potential). This serves to suggest electrode configuration for studying reactions under given conditions and the sensitivity of the pH probe under those conditions. We also diagnose what the local conditions might look like under a case of unbuffered CO formation on a silver macro-electrode, including the concentration profile of carbonate species.

4.2 Experimental

4.2.1 Finite Element Method (FEM) simulations

A silver macroelectrode in 0.1M KHCO₃ electrolyte under saturated CO₂R reaction conditions is simulated with a pH probe directly centered over the electrode (Figure 3-1). The system geometry and reactions are equivalent to that in Chapter 3. To briefly summarize, carbonate species homogeneous equilibrium reactions are considered in equations 3-4 - 3-7. CO₂R to CO (Eq. 3-1) is considered at the Ag surface electrode, along with HER (Eqs. 3-2 and 3-3) using equations 3-14 - 3-15. The interaction of protons at the tip electrode are considered completely reversible and fast, therefore are assumed to have negligible effects on the concentration, such that the tip electrode is assumed to have a no flux boundary condition.

The salting out effect for 0.1 M KHCO₃ is found to lower the concentration to 31 mM from the Schumpe equation below³⁵⁷:

$$\log_{10} \left(\frac{C_{G,0}}{C_G} \right) = \sum C_i * (h_i + h_G)$$

where $h_i = 0.0922$ and 0.0967 for K^+ and HCO_3^- respectively. Due to the negligible variance at this electrolyte concentration due to salting out, the bulk concentration for CO₂ is assumed to be at saturation (32 mM for 1 atm CO₂ in water at 25 C) in an aqueous 0.1 M KHCO₃ electrolyte.³⁵⁸

The pH is neutral, controlled by the bulk electrolyte concentration. Chemical parameters, unless otherwise specified, are listed in Tables 3-2 and 3-3.^{20,359}

4.3 Results and Discussion:

CO₂R on a silver electrode is known, along with gold and zinc, to highly favor CO formation over formate and C₂⁺ species production.^{245,360–363} CO₂R was simulated on a silver foil electrode of radius 5mm. Kinetic parameters for CO₂R on silver foil have been previously described by Weng et al. with a rate constant of $k_{0,CO_2} = 3E - 13 \text{ cm/s}$.³⁶³ Chronoamperometric studies were simulated in which the surface electrode potential was held constant for 100 s. 0.1 M KHCO₃ buffer was used for simulations except where otherwise stated.

A transient pH probe, held at a fixed position, L , over the surface has a growing pH boundary layer as a function of time and potential. The time after 100s shows a 2% growth in the local pH at a large overpotential (Figure 4-1). As our potential window ends at -0.9 V vs. Ag|AgCl, we find that a 100 second

simulation is sufficient such that local pH change is only due to pH boundary layer growth. After 100s at this potential, the

tip is within the boundary layer, so the pH change is minimal beyond this point.

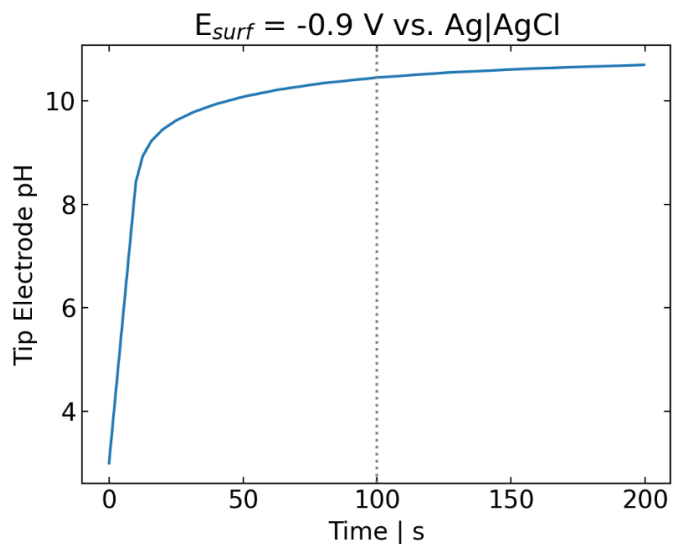


Figure 4-1: Time dependent pH at the tip electrode with a surface electrode potential of -0.9 V vs. Ag|AgCl. ($a = 25 \mu\text{m}$, $L = 3.2$, $R_{surf} = 100$, $RG = 10$, 0.1 M KHCO₃, 32 mM CO₂).

The pH, significantly influenced by HER near the surface, is potential dependent.¹⁶⁷ Previous studies into how the size of the probe effects the response has shown that minimizing the size, minimizes the effect of the probe.³⁵⁶

The previous studies demonstrated the effect of RG on pH in an unbuffered system (Figure 3-9). In 0.1M KHCO₃, a

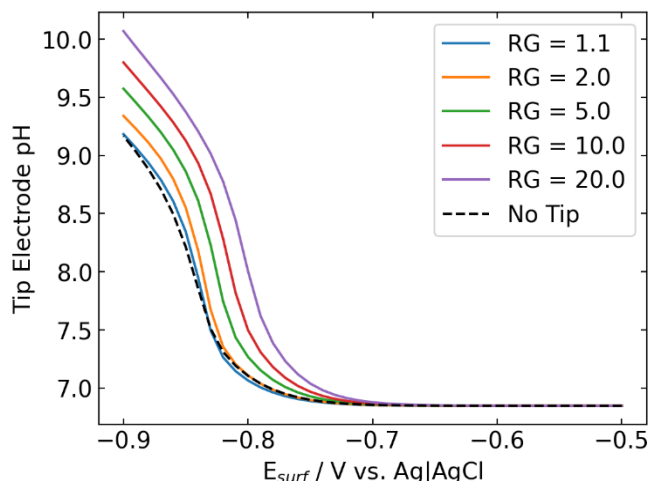


Figure 4-2: Insulation radius (RG) impact on pH-potential relations as detected at the pH probe 80 μm from the surface. ($a = 25 \mu\text{m}$, $L = 3.2$, $R_{surf} = 100$, 0.1 M KHCO₃, 32 mM CO₂).

similar increase in pH over high overpotentials is demonstrated as shown in Figure 4-2. As the insulation radius, RG , increases, the pH at the tip increases. This is due to increased hindered diffusion in the region beneath the probe. Perhaps most importantly, the pH, even at small radii, where hindered diffusion is minimized, demonstrates a pH increase at large overpotentials. This implies that, at potentials of $\sim -0.9\text{V}$ vs Ag|AgCl, a local pH change exists even without the presence of the probe. This can be further examined in our model by examining the pH at the

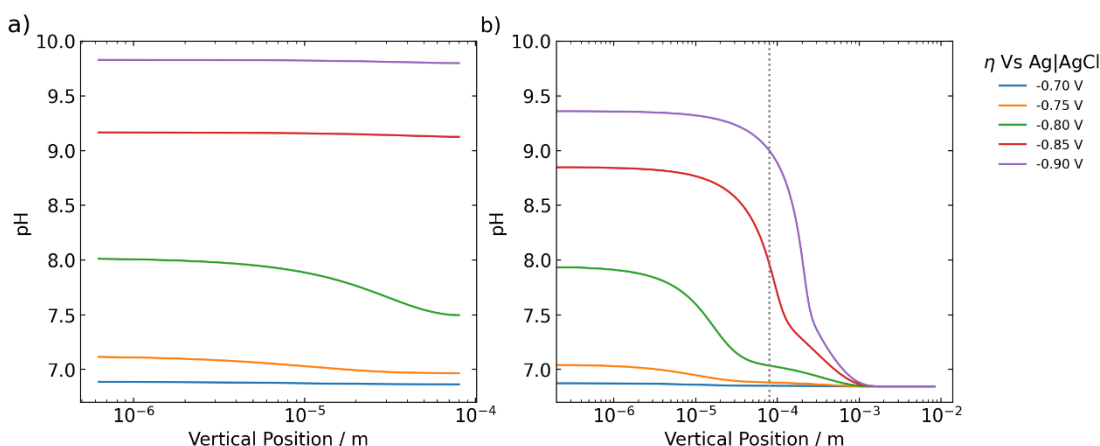


Figure 4-3: Vertical pH profile beneath the tip electrode at varied potentials. b) Vertical pH profile in the absence of the probe for different surface overpotentials. Grey dotted line correlates to the tip position. ($a = 25 \mu\text{m}$, $L = 3.2$, $R_{surf} = 100$, $RG = 10$, 0.1 M KHCO₃, 32 mM CO₂).

same location without the presence of the probe. The dashed line in Figure 4-2 shows the pH, at the same location as the probe, when the probe is not present. The pH resembles that of the thinnest insulation radius, indicating that the insulation radius significantly impacts hindered diffusion. This conclusion also agrees with previous results (Figure 3-9) in an unbuffered solution.

The flux due to electrochemical reactions for 1st order elementary reactions and above is dependent on reactant concentration at the electrode surface. The vertical concentration of all carbonate species varies with potential due to the potential dependent HER.

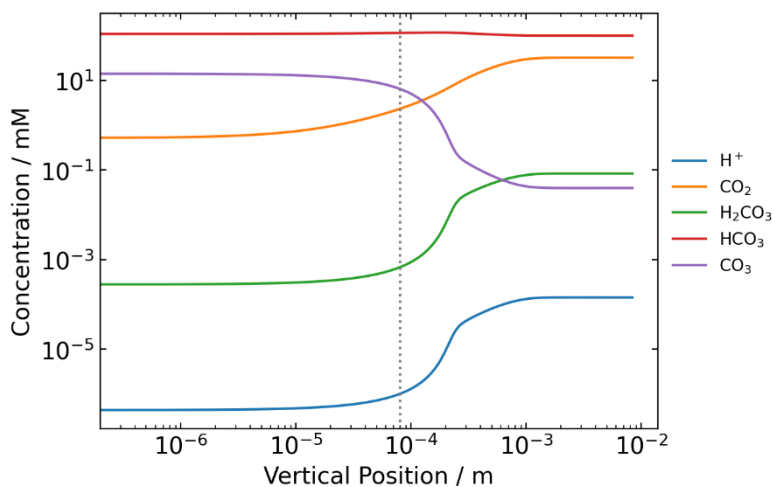


Figure 4-4: Vertical concentration profiles over the surface electrode at $E_{surf} = -0.9 \text{ V vs. Ag|AgCl}$. ($a = 25 \mu\text{m}$, $L = 3.2$, $R_{surf} = 100$, $RG = 10$, 0.1 M KHCO_3 , 32 mM CO_2).

As the pH increases (proton concentration decreases), blue curve in Figure 4-4, the carbonate concentration also increases (purple curve in Figure 4-4). Primarily, this change occurs at the pH boundary layer that is both time and potential dependent. As the pH increases towards the carbonate pK_a of 10.2 ($\sim 10^{-7} \text{ mM}$), the carbonate concentration trends towards that of bicarbonate. As the product distribution diversifies, it will be increasingly important to understand the species distribution near the surface.

Under large overpotentials, the concentration is horizontally uniform (Figure 4-5). Similar to a thin-layer cell, diffusion normal to the electrode is larger than horizontally. This implies that the probe is within the boundary layer. At

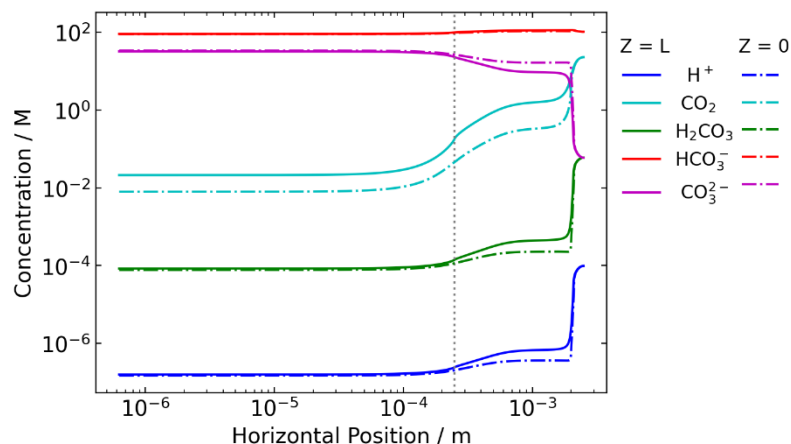


Figure 4-5: Horizontal concentration profiles at the surface electrode ($Z=0$) and at the tip electrode ($Z = L = 80\mu\text{m}$) at a potential of -0.9V vs. $\text{Ag}|\text{AgCl}$. ($a = 25\mu\text{m}$, $L = 3.2$, $R_{surf} = 100$, $RG = 10$, 0.1 M KHCO_3 , 32 mM CO_2).

the edge of the tip insulation, there is a large horizontal concentration gradient, increasing the diffusion in this region according to Fick's second law. At long times (100s) the proton depletion causes a pH equilibrium in the region beneath the probe, shown by comparing the H^+ concentration (blue curve, Figure 4-5) at $Z=L$ and $Z=0$.

Unlike Chapter 3, the buffered solution mitigates pH changes at low overpotentials, where the buffer can compensate for the consumption of protons.

As the overpotential increases, the water reduction rate on the surface increases, generating

more hydroxide ions and increasing the pH (Figure 4-3a). When the tip is outside of the pH

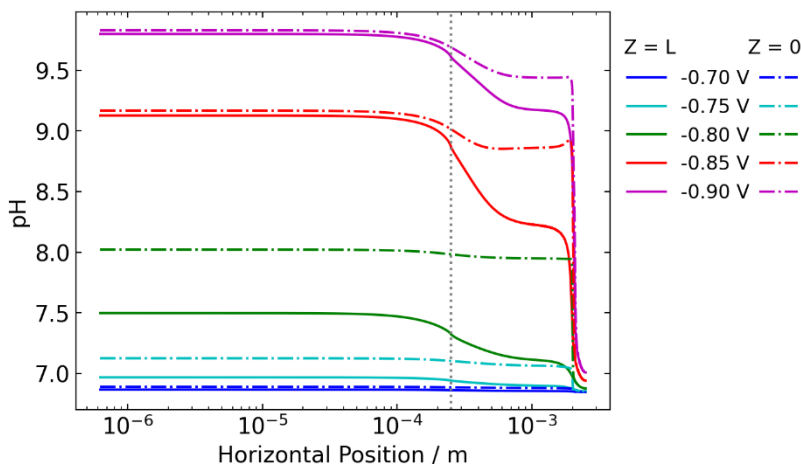


Figure 4-6: Horizontal pH profile at two different positions, at the surface electrode ($Z=0$) and at the tip electrode ($Z=L=80\mu\text{m}$). The surface electrode potential is varied vs $\text{Ag}|\text{AgCl}$. The insulation radius, RG , is indicated by the dotted line. ($a = 25\mu\text{m}$, $L = 3.2$, $R_{surf} = 100$, $RG = 10$, 0.1 M KHCO_3 , 32 mM CO_2).

boundary layer, there is a region of mixed diffusion, where the vertical concentration gradient drives diffusion between the probe and the surface electrode, and hindered diffusion also drives an increased horizontal diffusion. This is best illustrated at a potential of -0.8 V vs. Ag|AgCl in Figure 4-5. There are two distinct regions, where the pH has plateaued inside the pH boundary layer, but there is still a pH gradient near the surface. At low overpotentials, a linear, vertical concentration profile exists, consistent with a planar macroelectrode.

When diffusion resembles a thin cell underneath the pH probe, the pH at the SECM tip electrode resembles the pH at the surface beneath the probe. The vertical pH profiles beneath the probe shows a constant pH at large overpotentials (Figure 4-3a). This corresponds to the potentials at which the tip is within the pH boundary layer. When comparing the corresponding vertical pH profiles away from the probe (Figure 4-3b) to those underneath the probe (Figure 4-3a), there is an increase in the pH with respect to potential at the surface electrode for all overpotentials. However, at larger overpotentials (red and purple curves), where hindered diffusion begins to impact the pH, the pH change underneath the probe is larger. The impact of the presence of the tip electrode is further illustrated by comparing horizontal concentration profiles. In Figure 4-6, the pH at low overpotentials is consistent over the entire surface electrode, where the low reaction rates lead to a minimized hindered diffusion. At medium overpotentials, a pH gradient develops outward from the surface. The higher pH at $Z = L$ underneath the probe is indicative of hindered diffusion. At large overpotentials, the high kinetic rate leads to a large pH gradient. Additionally, the pH in the entire region beneath the tip is uniform, shown by the overlapping pH at tip and surface electrodes. What's more, the decreasing deviation in the pH at $Z = L$ vs. $Z = 0$ at -0.9 V vs. Ag|AgCl, as compared to -0.85 V vs. Ag|AgCl, indicates a growing pH boundary layer that is approaching $Z = L$.

As the separation between the tip electrode and surface electrode, L , increases, the amount of hindered diffusion decreases (Figure 4-7). The increasing pH at the tip for smaller separations and identical reaction conditions illustrates the increasing effect of hindered diffusion. The potential range in which high hindered diffusion exists, at high pH, widens as a function of L . At

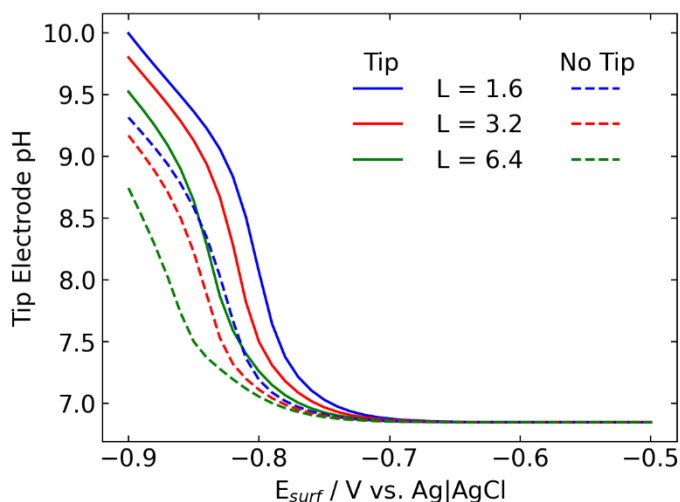


Figure 4-7: local pH during pulsed chronoamperometry as a function of tip-surface separation (L). ($a = 25 \mu m$, $R_{surf} = 100$, $RG = 10$, $0.1 M KHCO_3$, $32 mM CO_2$, $\nabla E = 10 mV$).

smaller separations the potential window affected by hindered diffusion begins at lower overpotentials. More importantly the closer separation qualitatively provides a better measurement of the undistorted pH field, even though hindered diffusion pH field distortion hinders the quantitative accuracy. High overpotentials, where the pH beneath the probe is constant (Figure 4-3a), is only limited by horizontal diffusion from the region away from the probe. Alternatively, when the kinetic activity is low, the pH probe may not detect any variance in pH at a given separation.

Combining the results in Figure 4-2 and Figure 4-7 in Figure 4-8 shows the generalized effects of hindered diffusion. At high kinetic activity (Figure 4-8a), the response is dependent on the separation and insulation radius. It can be summarized into one combined effect of solely hindered diffusion, such that there is a single curve. The pH at -0.9 V vs. Ag|AgCl does not completely collapse to a single curve, which would indicate that the response is not solely due to hindered diffusion. This can be related to the pH boundary layer being right at the boundary layer thickness (Figure 4-3b, purple curve). The definition of this relation is still under further research. However, we suggest that there are two regions, the hindered diffusion dominated region at low L and large RG, and the region in which the tip response is dominated by the pH boundary layer growth. At low kinetic activity, the pH change is not significant (Figure 4-8b, $\eta = -0.7 V$). At medium kinetic activity, the effect of the probe is combined with the effect of the growing pH boundary layer. This is illustrated by a higher pH at larger L/RG as the

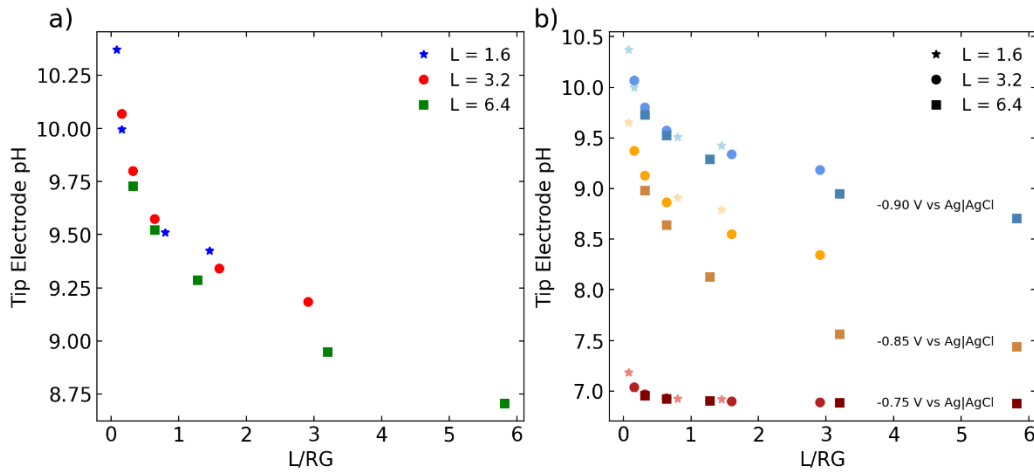


Figure 4-8: Potential dependent local pH as a function of the tip-surface separation (L), the insulation radius (RG), and the surface electrode potential (E_{sub}). Varied RG, at constant L, is differentiated by color (a) and shading/marker (b). The surface potential, indicated on the plot (-0.75, -0.8, and -0.9 V vs. Ag|AgCl) are separated by color in b. separation decreases. This implies that the amount of hindered diffusion is affected by L and RG distinctly ($E_{sub} = -0.85 V$ vs. Ag|AgCl) as compared to high kinetic rates ($E_{sub} =$

$-0.9\text{ V vs. Ag|AgCl}$). This shows that at medium overpotentials, there is an increased pH sensitivity to L for a given tip (constant RG), in agreement with Figure 4-7. Further, this demonstrates a mechanism to control at which potential the pH sensitivity is largest.

As the surface radius decreases, the total consumption rate decreases due to the decreasing surface area. This, in turn, affects hindered diffusion. Figure 4-9a indicates that as the size of the surface site decreases, larger overpotentials are required to observe an increase in pH at a given separation. This is particularly true as the surface electrode size approaches the radius of the tip, where a larger shift is observed due to the concentration profile shrinking. When $R_{surf} \gg R_{ins}$, the pH response become relatively uniform with minor variations at medium

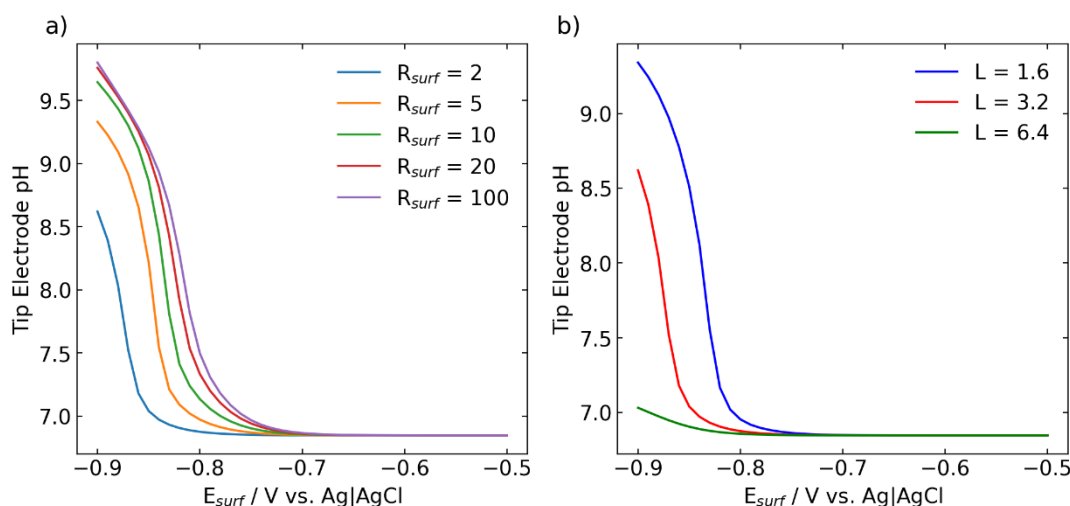


Figure 4-9: a) Local pH response as a function of surface electrode radius for a range of surface electrode potentials ($L = 3.2$). b) pH potential dependence at different tip-surface separation for a surface electrode radius of $R_{surf} = 2$. ($a = 25\ \mu\text{m}$, $L = 3.2$ (a), $RG = 10$, 0.1 M KHCO_3 , 32 mM CO_2 , $\nabla E = 10\text{ mV}$). overpotentials. At larger L , the sensitivity to pH decreases significantly for small surface electrodes ($R_{surf} = 2$) as shown in Figure 4-9b. The onset for pH increase shifts by $\sim 100\text{ mV}$ for

a 4 fold difference in separation (Figure 4-9b). While it might be obvious that smaller electrodes will have a smaller concentration profile, it is important to identify the separations at which the tip electrode is sensitive to the local profile.

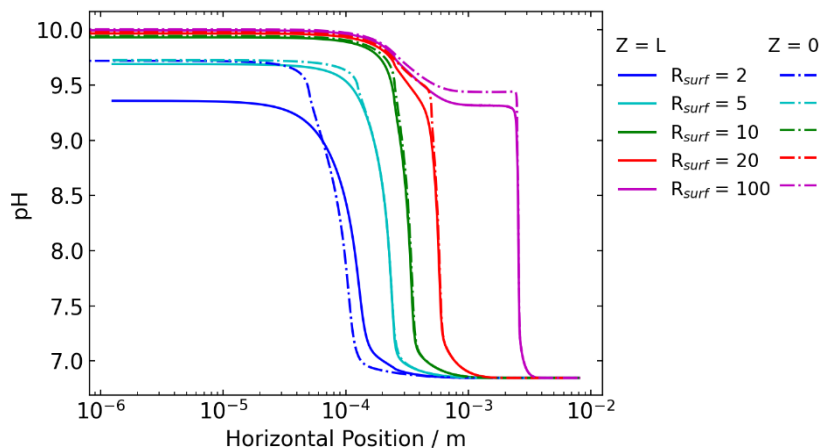


Figure 4-10: Horizontal pH profiles for varied surface electrode radii across the surface (dashed) and at the height of the tip (solid) at -0.9 V vs Ag|AgCl and 100s. ($a = 25 \mu\text{m}$, $L = 3.2$, $R_{surf} = 100$, $RG = 10$, 0.1 M KHCO_3 , 32 mM CO_2).

The macro electrode response ($R_{surf} = 100$, purple) has a constant vertical pH. As the surface electrode radius decreases, the concentration profile approaches a hemispherical concentration profile. The horizontal concentration profile (Figure 4-10) for a surface electrode twice the size of the tip radius shows a gradient from the edge of the surface site outwards. At this radius, the pH is lower at the tip as compared to the surface, indicating that it is not dominated by hindered diffusion. The remaining surface electrode sizes are dominated by hindered diffusion, indicated by the matching pH in the region beneath the electrode. When the insulation radius and the surface electrode are the same size (Figure 4-7, green), the pH at the surface and tip electrodes perfectly overlap. This means that at $t = 100$ s and $E_{surf} = -0.9$ V vs. Ag|AgCl, the pH

boundary layer, combined with hindered diffusion effects, is growing radially, beyond the tip electrode.

CO₂ concentration is frequently assumed to be at saturation. It is of interest to consider how deviations in bulk CO₂ concentration from saturation affect the pH. In Figure 4-12a, at low overpotentials low bulk CO₂ leads to an

increase in the pH at the probe. Increased carbonic acid formation at higher CO₂ concentrations leads to a lower pH. However, the pH at large overpotentials approaches the same value, regardless of the bulk concentration. The lack of deviation in pH at large overpotentials indicates that HER is the surface reaction primarily responsible for the increase in pH. The pH-potential

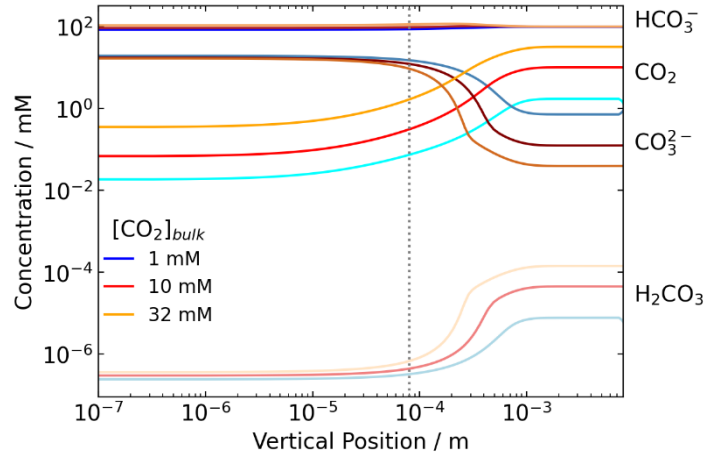


Figure 4-11: Vertical concentration profile of four species, H⁺, CO₂, HCO₃⁻, CO₃²⁻ as a function of bulk CO₂ concentration. The surface potential is held at -0.9 V vs. Ag|AgCl for 100s. ($a = 25 \mu\text{m}$, $L = 3.2$, $R_{surf} = 100$, $RG = 10$, 0.1 M KHCO₃).

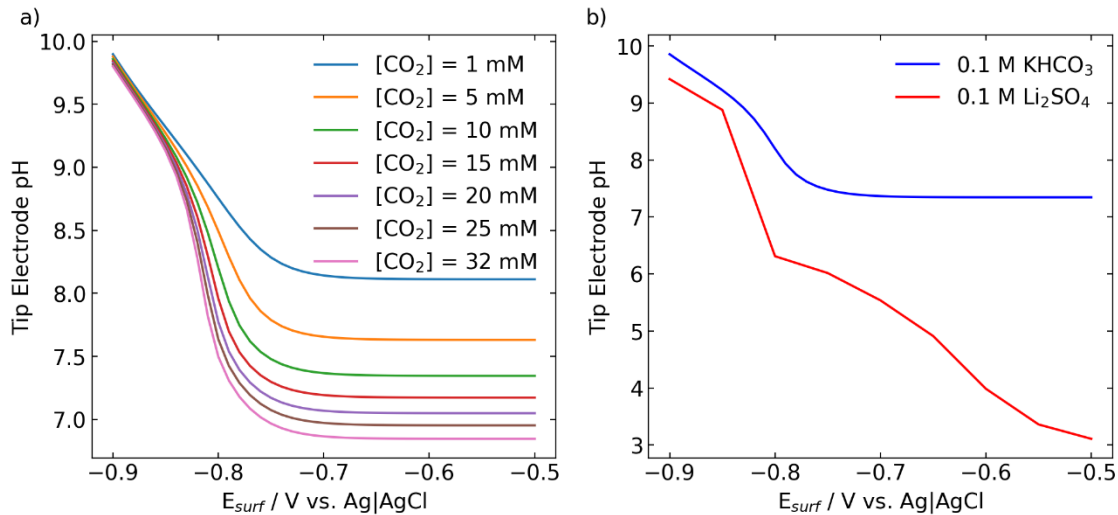


Figure 4-12: pH profiles versus surface potential for a) varied bulk CO₂ concentration. $L=3.2$ and $RG=10$ for the tip electrode with an electrolyte concentration of 0.1 M. The buffered electrolyte in (a) is compared to an unbuffered electrolyte from fig. 3-8 at $[\text{CO}_2] = 10 \text{ mM}$. ($a = 25 \mu\text{m}$, $L = 3.2$, $R_{surf} = 100$, $RG = 10$, 0.1 M KHCO₃ (a), $\nabla E = 10 \text{ mV}$).

relation can be compared to Figure 3-8 in which an unbuffered electrolyte is used (Figure 4-12b). The unbuffered electrolyte has a bulk acidic pH but increases to basic pH at large overpotentials. There are similar increases in pH at large overpotentials in both electrolytes. The difference in pH at low overpotentials reflects their different bulk pH. The vertical concentration profiles in Figure 4-11 demonstrate the

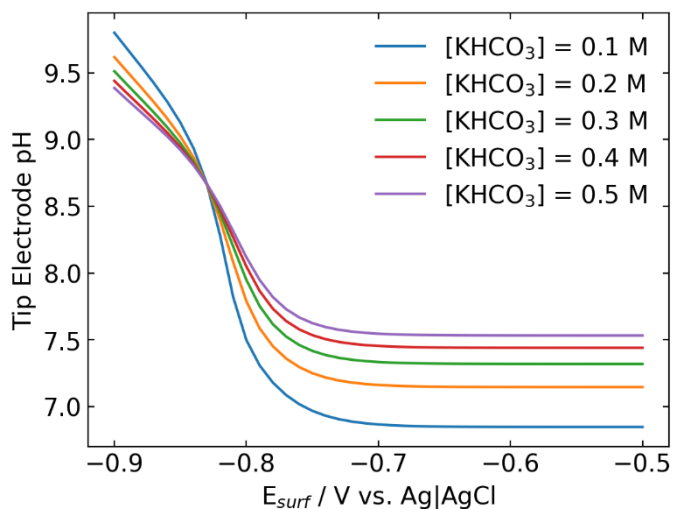


Figure 4-13: Potential dependent pH response for varied electrolyte (KHCO_3) concentrations. $L=3.2$ and $RG=10$ for the tip electrode with a CO_2 concentration of 32 mM. ($a = 25 \mu\text{m}$, $L = 3.2$, $R_{surf} = 100$, $RG = 10$, 32 mM CO_2 , $\nabla E = 10 \text{ mV}$).

convergence of the carbonate species within the boundary layer. Due to slow hydration of CO_2 , the CO_2 concentration within the pH boundary layer, remains distinct when compared to different CO_2 bulk concentrations.

The ability of the solution to buffer the local concentration change is inherent with CO_2 equilibrium reactions during CO_2R . It is further enhanced by the electrolyte composition. By varying the electrolyte concentration in Figure 4-13, a larger increase in pH is observed. The electrolyte is varied between 0.1 and 0.5 M, two commonly used electrolyte concentrations. The pH at low overpotentials is lower for small electrolyte concentrations, in agreement with previously measured bulk pH for these concentrations.³⁶⁴ At larger overpotentials, $E \rightarrow -0.9 \text{ V vs Ag|AgCl}$, the minimized buffering at low KHCO_3 increases the pH ~ 3 pH units, as compared to ~ 2 pH units at larger buffer concentrations.

4.4 Conclusions:

In this work we have shown that the pH and carbonate species vary as a function of the geometric parameters, spatial position, and composition. Specifically, at large overpotentials, the response at the tip electrode is dominated by the effects of hindered diffusion. Due to these effects, the pH beneath the tip is increased and spatially uniform. When hindered diffusion effects control the pH, there is a clear trend in pH versus the tip-surface separation and insulation radius, two parameters primarily affecting the tip surface separation. At medium overpotentials, the response of the probe is not entirely controlled by hindered diffusion. Because of this, the tip-surface separation has an increased effect over the insulation radius on the pH at the tip. The understanding of how the probe changes the local environment can help guide mechanistic studies for increased spatial resolution by controlling the potential at which the probe is most sensitive. Additionally, the combination experimental and simulation increases the breadth of chemical species information available. Due to hindered diffusion the homogeneous equilibrium reactions play a significant role in pH response at the tip.

The analysis presented here shows the relation of tip-surface spacing and insulation size with pH over a macro electrode. At high kinetic rates the pH beneath the probe is uniform. This forms a trend in which the insulation size and separation produce the same rise in pH due to hindered diffusion effects. At medium overpotentials, the separation causes a larger amount of hindered diffusion as compared to the insulation. The relationships described in this work is used to proactively design experiments using a pH ultramicroelectrode.

Chapter 5

Redox Couples in Aqueous AFM-SECM

5.1 Introduction

A review by Polcari et al. highlights the significant factors in design of experiments for SECM; electrolyte, analyte, and probe.²⁹⁹ The choice of each factor is non-trivial in the design of SECM experiments. Commercial AFM-SECM systems are somewhat prohibitive in the variety of probes. Additionally, there lacks a sufficient market currently for third-party probe sourcing. As such, the choice of analyte and electrolyte must also be chosen with regards to the given probe in addition to the interface that is being studied.

AFM-SECM probes, including their cantilevers, are composites.¹⁵⁸ The cantilevers of silicon nitride have a wire passing through the middle to electrically connect the exposed Pt tip to a wire connector. The insulation material is silicon dioxide, SiO₂, and there is a metal coating on the back of the probe to enhance the reflectivity of the probe. There are other epoxy components as well. As such the chemical stability of all these materials should be accounted for in the design experiments.

In positive feedback SECM a crucial component is a fast, reversible redox couple. Table 1-3 lists some redox couples used. A few common redox couples are commonly used regardless of their well-known deficiencies. For example, Ru(NH₃)₆ is known to be light sensitive.³⁶⁵ With a technique that is dependent on light and laser sources for operation, it is challenging to not degrade the redox couple and also contaminate the probe. Ferrocene is a common redox couple for organic solvents in SECM.²⁹⁹ However, its derivatives, in which different groups are added, are often used to increase its solubility. One of the most common redox couples, ferrocene methanol, still has a low solubility in water (~1 mM), but the fast kinetics ($k_0 \approx 10 \text{ cm s}^{-1}$) at mild

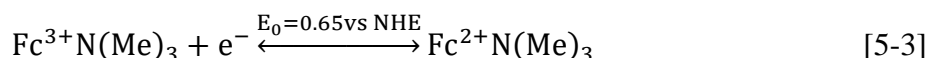
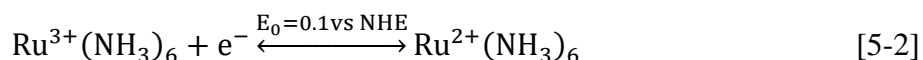
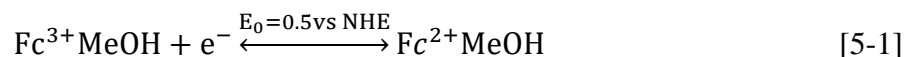
potentials for ferrocene compounds is attractive. Compatibility of redox couples with the system is essential. Ferri/ferrocyanide is highly soluble. However, AFM-SECM probes use a gold coated cantilever for an enhanced AFM response in liquid. Cyanide groups adsorb on gold at room temperature, making it a contamination source.^{366,367}

The consideration of how the redox couple interacts with all components of the electrochemical cell in use, and particularly the probe, is critical for SECM measurements. In this chapter we aim to provide key comparative behaviors for a few common redox couples for SECM.

5.2 Experimental

5.2.1 Materials

A series of redox couples were electrochemically tested in a 0.1 M potassium chloride (KCl) aqueous electrolyte (Sigma Aldrich). Electrochemical tests were carried out on a polytetrafluoroethylene (PTFE) insulated platinum RDE (Pine Research) and a Pt AFM-SECM electrode (Bruker). RDE tests were conducted with an Ag|AgCl reference electrode and Pt wire counter electrode. AFM-SECM experiments used a silver wire quasi-reference electrode (AgQRE) and a Pt wire counter electrode. Four redox couples (Equations 5-1-5-4) were considered (see Table 1-3); Ferrocene methanol (FcMeOH: Sigma Aldrich), Ruthenium Hexamine Trichloride ($\text{Ru}(\text{NH}_3)_6\text{Cl}_3$: Sigma Aldrich), (Ferrocenylmethyl)trimethylammonium Chloride (FcNCl: Tokyo Chemical Industries), and Methyl Viologen (MV: Sigma Aldrich).





5.2.2 Cyclic voltammetry

Cyclic voltammetry measurements, using a Biologic VSP potentiostat, were carried out in a jacketed electrochemical cell maintained at 25 C. The rotating disk electrode was spun at 1600 rpm. Experiments were carried out under nitrogen saturation using nitrogen sparging throughout the duration of measurements. The sweep rate was maintained at 20 mV/s across all measurements.

5.2.3 SECM

SECM measurements were carried out in a sandwich cell. A surface electrode was electrically connected from the backside and sealed using a teflon insert and gasket. The cell was connected to a CH instruments 700E Bipotentiostat for electrochemical measurements. A Bruker Dimension Icon was used for AFM-SECM measurements.

5.2.4 SECM Probe Cleaning

5.2.4.1 Plasma Cleaning

AFM-SECM tip electrodes were plasma cleaned³⁶⁸ using a Harrick Plasma Basic Plasma Cleaner. After pumping the chamber below 1 Torr, the plasma was generated on “low” (6.5W) for <15 min. Subsequently, the tip was dipped in 18.2 MΩ DI water to rinse.

5.2.4.2 Warm Water

Alternatively, a warm water bath was used to clean the AFM-SECM tip electrode. The tip, in 18.2 MΩ DI water, was raised to 85 C in a preheated oven. The probe was held at this temperature for ~15 minutes. The tip was subsequently dipped in fresh room temperature DI water.

5.3 Results and Discussion:

5.3.1 AFM-SECM

$\text{Ru}(\text{NH}_3)_6$, previously used for AFM-SECM measurements, is known to be light sensitive.³⁶⁵ Its fast, outer-sphere electron transfer, and high solubility make it an attractive option for SECM measurements.¹⁵⁸ However, the degradation of the couple when exposed to ambient light during long SECM

measurements causes the AFM cantilever to become contaminated (Figure 5-1). This

visible contamination decreased the laser total reflectance from the back of the

cantilever, leaving the probe less sensitive to

topography. Additionally, the electrochemical

response is also diminished after SECM

imaging due to contamination (Figure 5-2).

Contamination of the probe made this couple undesirable for use in AFM-SECM imaging measurements.

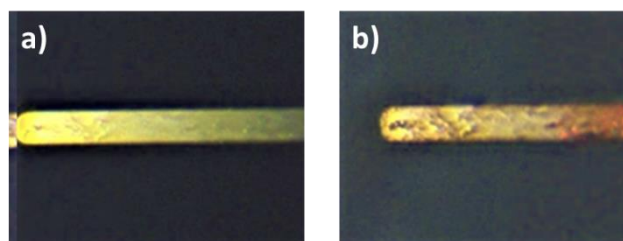


Figure 5-1: AFM-SECM probe before (a) and after (b) SECM measurements in 10 mM $\text{Ru}(\text{NH}_3)_6$ and 0.1 M KCl.

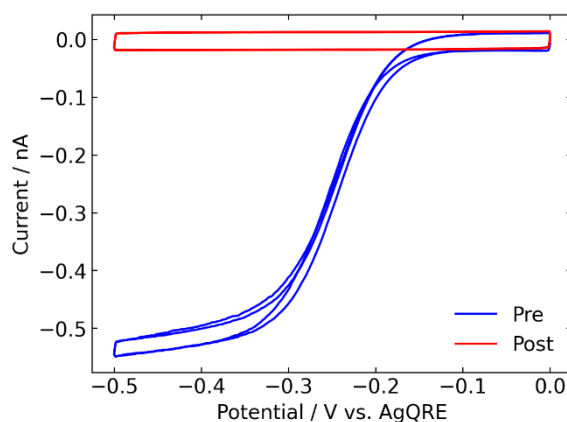


Figure 5-2: AFM-SECM tip CV in 10 mM $\text{Ru}(\text{NH}_3)_6$ and 0.1 M KCl before and after SECM imaging.

5.3.2 RDE CV decay studies

Alternate redox couples have been used

for a variety of substrates in SECM.²⁹⁹ The compatibility with the probe and AFM analysis

conditions is critical in addition to its reversibility and kinetics. To prevent further damage to the

AFM-SECM probes, we test the stability first through CV degradation studies. Feedback mode SECM independently drives the reduction and oxidation reactions at the two electrodes. To mimic this cycling, a CV alternatingly drives the reduction and oxidation reactions (Figure 5-3).

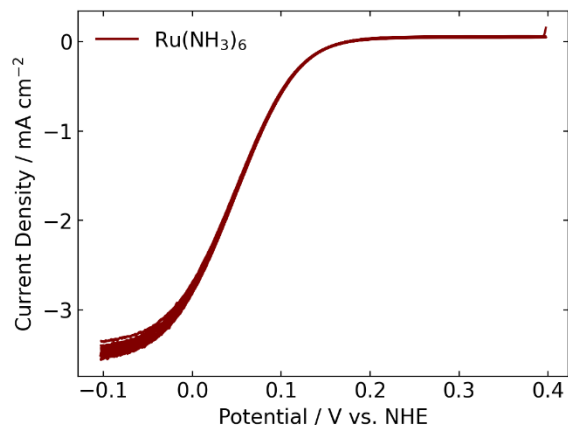


Figure 5-3: 20 cycle CV on a 5 mm Pt RDE in 0.1 M KCl with 10 mM $\text{Ru}(\text{NH}_3)_6$. The rotation was held at 1600 rpm.

The reduction current for $\text{Ru}(\text{NH}_3)_6$ decreases with cycling. Degradation can be characterized by the amount of oxidation and reduction reactions

that occur as a function of cycle (i.e. time). We define the degradation rate as:

$$r = \Delta(i_{ox} + i_{red}) \quad [5-5]$$

where i_{ox} is the oxidative current, i_{red} is the reductive current density and r is the cycle-to-cycle decay rate. i_{ox} is minimal as the bulk species is oxidized ($\text{Ru}(\text{NH}_3)_6^{3+}$). In Figure 5-4, the decay

rate of $\text{Ru}(\text{NH}_3)_6$ is shown to be high compared to other redox couples. For this reason we have determined that it is not feasible under reasonable conditions in our system.

Methyl viologen had a relatively low decay rate. However, the redox potential for sufficient

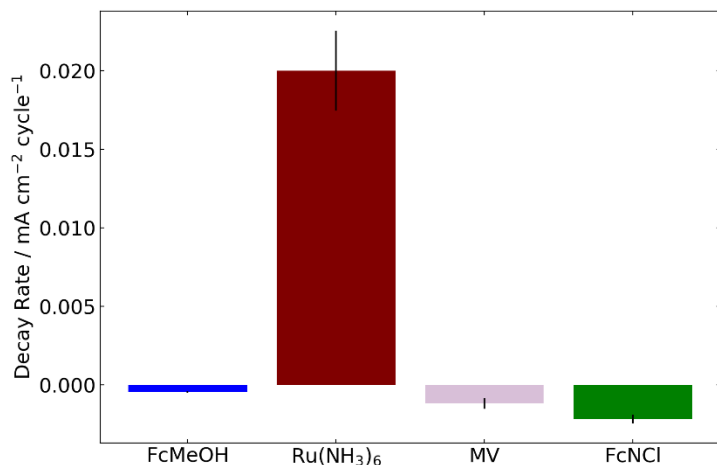


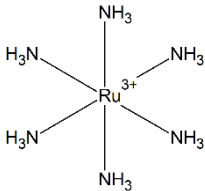
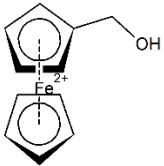
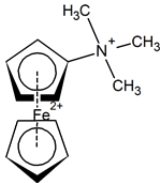
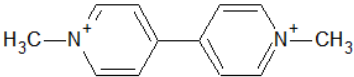
Figure 5-4: Redox couple decay rates from CV studies at 1600 rpm in 0.1 M KCl.

reduction of its radical is below -0.45 V vs NHE and is therefore also expected to undergo HER

at the electrode. Additionally, the blue shift of the radical (MV^{+1})³⁶⁹ decreased the AFM signal ~4 fold. This makes mapping the surface increasingly difficult. It was decided that a combined decreases in AFM signal and promotion of side reactions (HER) makes MV not ideal for AFM-SECM feedback studies.

The two ferrocene-based compounds, FcMeOH and FcNCl, had minimal decay rates. FcNCl has a significantly higher solubility, but the redox potential is higher. To be at mass transfer limited oxidation currents (i_{ox}), the electrode would need be poised $>\sim 750$ mV vs NHE. This is close to potentials where one might start to see oxygen evolution (~ 0.8 V vs NHE @ pH=7). Given the use of a quasi-reference electrode, it's important to choose potentials far from any potential side reactions.

Table 5-1: Redox couple comparison in aqueous solutions.

				
Solubility	High	1 mM	4 M	0.2 M
Stability	Low	High	High	High
$E^{0'}$ vs NHE	0.05	0.44	0.597	-0.45

5.3.3 Cleaning of AFM-SECM electrodes

The enhanced mass transport and presence of impurities in solution lead to contamination of SECM nanoelectrodes.³⁶⁸ However, given the fragility of these electrodes, mechanical cleaning is not possible without significant risk of damaging the tip. Sun et al. had success cleaning electrodes with air plasma.³⁶⁸ For Bruker AFM-SECM electrodes using a Harrick Plasma Basic Plasma Cleaner on “low” (6.5W) for <15 min. was successful. The plasma caused the tip to rise in temperature and, for time >15 min, caused embrittling of the epoxy that surrounds the probe. If longer time periods are required due to increased contamination, we find that multiple plasmas with rinsing in DI water to be reasonable as it both cools the probe and removes oxidized impurities. Increasing the temperature of water can increase the solubility of the impurities in DI water. However, the epoxy once again becomes embrittled with too long of periods at increased temperatures. Electrochemical cycling in sulfuric acid, a known method for cleaning platinum electrodes, weakens the bonding of insulating glass to the epoxy encapsulant of the AFM-SECM probe. Each method of cleaning the tip was compared by using a Pt wire working electrode in the SECM (Figure 5-5). The plasma cleaning method after 15 min showed a response close to the original. The warm water also worked reasonably well, but the oxidation peak potential was slightly shifted, indicating that there needed to be further cleaning.

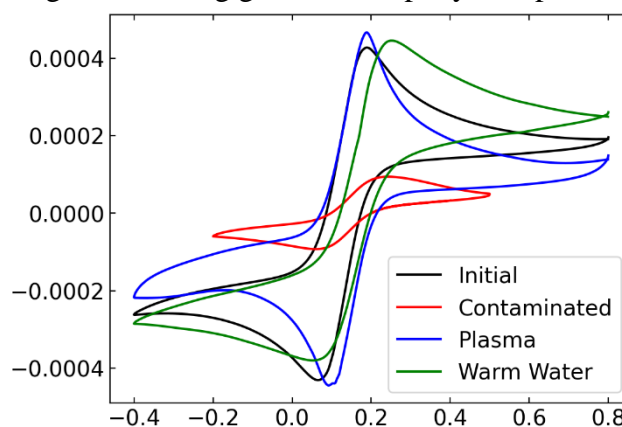


Figure 5-5: CV at 50 mV/s over a Pt wire in the SECM cell comparing the initial response (black) to after use (red), and the two cleaning methods of plasma (blue) and warm water (green). (20 mV/s, 2 mM FcMeOH, 0.1 M KCl).

5.4 Conclusions

The contamination of nanoelectrodes have long been a concern due to the increased mass transport and small surface area.^{368,370,371} The fragility of nanoelectrodes makes cleaning of these electrodes challenging. An intentional approach of minimizing impurities and optimized potential window with simultaneously understanding the stability of the redox couple used can help to minimize contamination of these electrodes. While we present four commonly used redox couples decay rate analysis, we recognize the abundance of potential redox couples that have been used in a variety of environments. It is then more relevant to rationally choose which redox couple is optimal for a given environment considering: 1) materials in the system, 2) stability of the redox couple, 3) redox degradation mechanisms with respect to operational conditions (i.e. light), and 4) the solubility of the redox couple in the electrolyte.

Chapter 6

Conclusions and Future Directions

The work in this thesis is motivated by the need to quantitatively understand physicochemical property relations at the liquid-solid interface for electrochemical reactions. The development of an experimentally informed FEM simulation demonstrably removes the effects due to the presence of the probe in SECM measurements. This provides a means to understand the local environment of electrocatalytic reactions. In this thesis, we examine local probe effects for multiple systems and propose properties such as the insulation radius that control the probe effects.

Chapter 2 focuses on the tip effects in SECM electrochemical mapping, where the 2D tip current is related to concentration over nanoparticle active sites. Approximately 50 nm electrochemical resolution is, to our knowledge the highest resolution to date for AFM-SECM and approaches the size of the tip. We show that, due to enhanced mass transport at the tip in UMEs, finite large kinetic values ($k_0=10$ cm/s) are required to accurately simulate experimental results. Mass transfer boundary conditions leads to errors for high aspect ratio tips due to interactions with the non-apex region of the tip electrode. Simulations of nanoscale surface geometries revealed concentration errors up to 120% due to the presence of a disk electrode SECM probe. We study the effects of the surface and tip geometry on the concentration profiles in SECM measurements. Differences in concentration due to the presence of the probe are attributed to: 1) positive feedback enhancement and 2) hindered diffusion, which are both affected by: 1) tip trajectory, 2) tip geometry, 3) surface geometry, and 4) kinetic rates at both electrodes.

Chapters 3 and 4 studied the probe effects due to a stationary SECM probe that was functionalized to measure the pH at high time and spatial resolution. The probe effects enhanced the pH by up to ~7.5 pH units at a given potential due to hindered diffusion when compared to experimental results. While the probe was demonstrated to have effects on the pH profile, the trends seen experimentally were still representative of what happens when the probe is not present.

In addition to reactively removing the effects of the probe, we also proactively study the parameters that control the probe effects. The insulation radius was shown to have an inverse relation with probe effects. Minimizing the insulation radius, even to a size twice as large as the tip (R_{tip}), removed the effect of the probe. For a macro surface electrode, it was shown that the insulation radius, R_G , and tip-surface separation, L , have a correlated impact on the probe. This is particularly true for larger overpotentials, where the pH boundary layer has grown large enough such that the SECM probe is within the boundary layer. As the surface electrode radius decreases, the effects of the probe decreases, along with sensitivity to the local pH gradient.

Chemical factors, such as CO_2 and buffer concentration were also explored. For CO_2R studies, CO_2 equilibrium reactions always forms buffering carbonates. The addition of KHCO_3 can be shown to have an impact on the low overpotential region, which proton reduction dominates. The bicarbonate buffer raises the bulk electrolyte pH to ~7, minimizing the proton concentration near the surface. This minimizes the reactivity at low potentials and creates a flat pH-potential response. However, in the high overpotential regions, a similar effect in buffered and unbuffered pH responses is observed. This is due to water reduction at more basic pH. The first equilibrium reaction that CO_2 undergoes is the formation of carbonic acid. At larger CO_2 concentrations, this acidifies the solution, lowering the pH. The effect of buffer concentration

was studied in the experimentally relevant region of 0.1 – 0.5 M. These concentrations are 30-150 times larger in concentration than saturated aqueous CO₂. The local pH profile is dependent on the buffer concentration, which controls the bulk pH and the increase in local pH at large overpotentials.

Overall, Chapters 2, 3, and 4 demonstrate how the local environment is more important for physicochemical property relations. Relating parameters such as kinetic rate constants and local concentrations to physical properties such as the surface site geometry and size will drive further understanding of electrochemical reactions. To study these reactions, we use SECM. The presence of the electrochemical probe near the surface was quantitatively shown to affect the local concentration profile. We remove these effects by correlating a FEM simulation with experimental results.

For these studies to be possible, the accuracy and strength of signal from AFM-SECM must be high. One of the most important features is the analyte. In chapter 5, we transitioned to study how stable four common redox couples are in solution. The enhanced mass transport of nano electrodes and their small surface area make them particularly susceptible to contamination. Additionally, the fragility of these electrodes limit how/if they can be cleaned. We showed that, for the complex AFM-SECM system, additional parameters such as the reflectivity of the laser for surface tracking is also important. Therefore methyl viologen, a stable and soluble redox couple, is incompatible with AFM-SECM systems as it reduced the total reflectance, received at the sensor, 4 fold. Cyanide compounds, which are stable on gold, and light sensitive compounds such as Ru(NH₃)₆, similarly lower the reflectivity of the gold plated cantilever. The degradation of Ru(NH₃)₆ also decreases as it degrades and coats the AFM-SECM tip. Ferrocene compounds

are relatively stable. However, optimization of the ligand molecule/s controls the redox potential and the solubility.

The work presented herein allow for corrections to concentration measurements over interfaces. The application of this work to complex interfaces with multiple reactive species is of interest. As in Chapter 3, the use of functionalized SECM probes can provide unique insights. Specifically, the use of functionalized probes to study individual rates of specific species will allow for the design of efficient chemical reactions and transportation control.

SECM UMEs have, in large part, made use of laser pulled, polished electrodes. These electrodes are relatively easier to maintain. As such, they have been able to creatively modify these probes. While AFM-SECM probes enable simultaneous topographical and electrochemical analysis, their complex probe structure limits the ways in which they can be modified. Electrochemical deposition of functional groups is one way to prevent deposition on other parts of the probe, such as the back of the cantilever used for laser reflectance. The electrochemical modification of these probes is an important step to simplify the electrochemical response of complex solutions. The use of membranes, such as chitosan, will enable enzyme decoration of the probe. Chitosan is deposited based upon the local pH. As shown in Chapter 4, the local pH is potential dependent. It should be possible to control the film thickness. The thickness will have a significant impact on the electrochemical response and topographical resolution. Accounting for the impact on this will be important for future studies.

A modified probe provides capability to directly analyze local reaction intermediates in complex reactions. Use of a membrane with an enzyme will allow for isolated response of the intermediate concentration. In catalyst cascades, in which the transport of intermediates controls the reaction efficiency, detection of these intermediates will allow analysis of synthetic cascades

and their transport efficiency. This can also be applied to complex kinetics to derive the local concentration dependence of a given species (exemplified in Chapter 3).

This thesis serves as a guide for future local concentration studies using SECM, which promise to be of importance in electrolysis, energy, corrosion, and other fields. The removal of probe effects will allow quantitative correlation of physicochemical properties to concentration. Additionally, we suggest a few specific cases in which the probe effects can be minimized, when the insulation radius is small and for high aspect ratio tips (i.e., conical AFM-SECM tips). The results in this thesis will help guide the development of molecular/nanoscale electrocatalysts and nanoscale transport.

BIBLIOGRAPHY

BIBLIOGRAPHY

- (1) Pletcher, D. *A First Course in Electrode Processes*; 2009.
- (2) Faulkner, L. R. Understanding Electrochemistry: Some Distinctive Concepts. *J. Chem. Educ.* **1983**, *60* (4), 262. <https://doi.org/10.1021/ed060p262>.
- (3) Shearing, P. R.; Brett, D. J. L.; Brandon, N. P. Towards Intelligent Engineering of SOFC Electrodes: A Review of Advanced Microstructural Characterisation Techniques. *International Materials Reviews* **2010**, *55* (6), 347–363. <https://doi.org/10.1179/095066010X12777205875679>.
- (4) Dillon, S. J.; Sun, K. Microstructural Design Considerations for Li-Ion Battery Systems. *Current Opinion in Solid State and Materials Science* **2012**, *16* (4), 153–162. <https://doi.org/10.1016/j.cossms.2012.03.002>.
- (5) García, R. E.; Chiang, Y.-M. Spatially Resolved Modeling of Microstructurally Complex Battery Architectures. *J. Electrochem. Soc.* **2007**, *154* (9), A856. <https://doi.org/10.1149/1.2754072>.
- (6) García, R. E.; Chiang, Y.-M.; Carter, W. C.; Limthongkul, P.; Bishop, C. M. Microstructural Modeling and Design of Rechargeable Lithium-Ion Batteries. *J. Electrochem. Soc.* **2004**, *152* (1), A255. <https://doi.org/10.1149/1.1836132>.
- (7) Cashen, C.; Evans, R. C.; Nilsson, Z. N.; Sambur, J. B. Local Substrate Heterogeneity Influences Electrochemical Activity of TEM Grid-Supported Battery Particles. *Frontiers in Chemistry* **2021**, *9*, 164. <https://doi.org/10.3389/fchem.2021.651248>.
- (8) Friend, C. M.; Xu, B. Heterogeneous Catalysis: A Central Science for a Sustainable Future. *Acc. Chem. Res.* **2017**, *50* (3), 517–521. <https://doi.org/10.1021/acs.accounts.6b00510>.
- (9) Hsu, T.; Epting, W. K.; Mahbub, R.; Nuhfer, N. T.; Bhattacharya, S.; Lei, Y.; Miller, H. M.; Ohodnicki, P. R.; Gerdes, K. R.; Abernathy, H. W.; Hackett, G. A.; Rollett, A. D.; De Graef, M.; Litster, S.; Salvador, P. A. Mesoscale Characterization of Local Property Distributions in Heterogeneous Electrodes. *Journal of Power Sources* **2018**, *386*, 1–9. <https://doi.org/10.1016/j.jpowsour.2018.03.025>.
- (10) Hori, Y. Electrochemical CO₂ Reduction on Metal Electrodes. In *Modern Aspects of Electrochemistry*; Vayenas, C. G., White, R. E., Gamboa-Aldeco, M. E., Eds.; Modern Aspects of Electrochemistry; Springer: New York, NY, 2008; pp 89–189. https://doi.org/10.1007/978-0-387-49489-0_3.
- (11) Li, Y.; Boone, E.; El-Sayed, M. A. Size Effects of PVP–Pd Nanoparticles on the Catalytic Suzuki Reactions in Aqueous Solution. *Langmuir* **2002**, *18* (12), 4921–4925. <https://doi.org/10.1021/la011469q>.

- (12) Haruta, M. When Gold Is Not Noble: Catalysis by Nanoparticles. *The Chemical Record* **2003**, 3 (2), 75–87. <https://doi.org/10.1002/tcr.10053>.
- (13) Koper, M. T. M. Structure Sensitivity and Nanoscale Effects in Electrocatalysis. *Nanoscale* **2011**, 3 (5), 2054–2073. <https://doi.org/10.1039/C0NR00857E>.
- (14) Kleijn, S. E. F.; Lai, S. C. S.; Koper, M. T. M.; Unwin, P. R. Electrochemistry of Nanoparticles. *Angewandte Chemie International Edition* **2014**, 53 (14), 3558–3586. <https://doi.org/10.1002/anie.201306828>.
- (15) Bard, A. J. Inner-Sphere Heterogeneous Electrode Reactions. Electrocatalysis and Photocatalysis: The Challenge. *J. Am. Chem. Soc.* **2010**, 132 (22), 7559–7567. <https://doi.org/10.1021/ja101578m>.
- (16) Haensch, M.; Balboa, L.; Graf, M.; Silva Olaya, A. R.; Weissmüller, J.; Wittstock, G. Mass Transport in Porous Electrodes Studied by Scanning Electrochemical Microscopy: Example of Nanoporous Gold. *ChemElectroChem* **2019**, 6 (12), 3160–3166. <https://doi.org/10.1002/celec.201900634>.
- (17) Kai, T.; Zhou, M.; Johnson, S.; Ahn, H. S.; Bard, A. J. Direct Observation of $\text{C}_2\text{O}_4^{\bullet-}$ and $\text{CO}_2^{\bullet-}$ by Oxidation of Oxalate within Nanogap of Scanning Electrochemical Microscope. *J. Am. Chem. Soc.* **2018**, 140 (47), 16178–16183. <https://doi.org/10.1021/jacs.8b08900>.
- (18) Trinh, D.; Keddam, M.; Nóvoa, X. R.; Vivier, V. Characterization of Adsorbates by Transient Measurements in Scanning Electrochemical Microscopy. *Electrochimica Acta* **2014**, 131, 28–35. <https://doi.org/10.1016/j.electacta.2014.02.002>.
- (19) Singh, M. R.; Goodpaster, J. D.; Weber, A. Z.; Head-Gordon, M.; Bell, A. T. Mechanistic Insights into Electrochemical Reduction of CO_2 over Ag Using Density Functional Theory and Transport Models. *PNAS* **2017**, 114 (42), E8812–E8821. <https://doi.org/10.1073/pnas.1713164114>.
- (20) Bohra, D.; Chaudhry, J. H.; Burdyny, T.; Pidko, E. A.; Smith, W. A. Modeling the Electrical Double Layer to Understand the Reaction Environment in a CO_2 Electrocatalytic System. *Energy Environ. Sci.* **2019**, 12 (11), 3380–3389. <https://doi.org/10.1039/C9EE02485A>.
- (21) Monteiro, M. C. O.; Mirabal, A.; Jacobse, L.; Doblhoff-Dier, K.; Barton, S. C.; Koper, M. T. M. Time-Resolved Local pH Measurements during CO_2 Reduction Using Scanning Electrochemical Microscopy: Buffering and Tip Effects. *JACS Au* **2021**. <https://doi.org/10/gm6t96>.
- (22) Jamali, S. S.; Moulton, S. E.; Tallman, D. E.; Zhao, Y.; Weber, J.; Wallace, G. G. Self-Healing Characteristic of Praseodymium Conversion Coating on AZNd Mg Alloy Studied by Scanning Electrochemical Microscopy. *Electrochemistry Communications* **2017**, 76, 6–9. <https://doi.org/10.1016/j.elecom.2017.01.004>.
- (23) Nazarov, A.; Vivier, V.; Vucko, F.; Thierry, D. Effect of Tensile Stress on the Passivity Breakdown and Repassivation of AISI 304 Stainless Steel: A Scanning Kelvin Probe and

Scanning Electrochemical Microscopy Study. *J. Electrochem. Soc.* **2019**, *166* (11), C3207. <https://doi.org/10.1149/2.0251911jes>.

(24) Rosenfeld, I. L.; Danilov, I. S. Electrochemical Aspects of Pitting Corrosion. *Corrosion Science* **1967**, *7* (3), 129–142. [https://doi.org/10.1016/S0010-938X\(67\)80073-8](https://doi.org/10.1016/S0010-938X(67)80073-8).

(25) Silva, E. L.; Lamaka, S. V.; Mei, D.; Zheludkevich, M. L. The Reduction of Dissolved Oxygen During Magnesium Corrosion. *ChemistryOpen* **2018**, *7* (8), 664–668. <https://doi.org/10.1002/open.201800076>.

(26) Snihirova, D.; Lamaka, S. V.; Gonzalez-Garcia, Y.; Yilmaz, A.; Scharnagl, N.; Montemor, M. F.; Zheludkevich, M. L. Influence of Inhibitor Adsorption on Readings of Microelectrode during SVET Measurements. *Electrochimica Acta* **2019**, 322, 134761. <https://doi.org/10.1016/j.electacta.2019.134761>.

(27) Atkinson, A.; Barnett, S.; Gorte, R. J.; Irvine, J. T. S.; McEvoy, A. J.; Mogensen, M.; Singhal, S. C.; Vohs, J. Advanced Anodes for High-Temperature Fuel Cells. *Nature Mater* **2004**, *3* (1), 17–27. <https://doi.org/10.1038/nmat1040>.

(28) Weber, A. Z.; Darling, R. M.; Newman, J. Modeling Two-Phase Behavior in PEFCs. *Journal of The Electrochemical Society* **2004**, *151* (10), A1715. <https://doi.org/10.1149/1.1792891>.

(29) Anker, J. N.; Hall, W. P.; Lyandres, O.; Shah, N. C.; Zhao, J.; Van Duyne, R. P. Biosensing with Plasmonic Nanosensors. *Nature Mater* **2008**, *7* (6), 442–453. <https://doi.org/10.1038/nmat2162>.

(30) Campbell, F. W.; Compton, R. G. The Use of Nanoparticles in Electroanalysis: An Updated Review. *Anal Bioanal Chem* **2010**, *396* (1), 241–259. <https://doi.org/10.1007/s00216-009-3063-7>.

(31) Hernández-Santos, D.; González-García, M. B.; García, A. C. Metal-Nanoparticles Based Electroanalysis. *Electroanalysis* **2002**, *14* (18), 1225–1235. [https://doi.org/10.1002/1521-4109\(200210\)14:18<1225::AID-ELAN1225>3.0.CO;2-Z](https://doi.org/10.1002/1521-4109(200210)14:18<1225::AID-ELAN1225>3.0.CO;2-Z).

(32) Monteiro, M. C. O.; Koper, M. T. M. Measuring Local PH in Electrochemistry. *Current Opinion in Electrochemistry* **2021**, *25*, 100649. <https://doi.org/10.1016/j.coelec.2020.100649>.

(33) Zhang, F.; Co, A. C. Direct Evidence of Local PH Change and the Role of Alkali Cation during CO₂ Electroreduction in Aqueous Media. *Angewandte Chemie International Edition* **2020**, *59* (4), 1674–1681. <https://doi.org/10.1002/anie.201912637>.

(34) Wencel, D.; Abel, T.; McDonagh, C. Optical Chemical PH Sensors. *Anal. Chem.* **2014**, *86* (1), 15–29. <https://doi.org/10.1021/ac4035168>.

(35) Dieckhöfer, S.; Öhl, D.; Junqueira, J. R. C.; Quast, T.; Turek, T.; Schuhmann, W. Probing the Local Reaction Environment During High Turnover Carbon Dioxide Reduction with

Ag-Based Gas Diffusion Electrodes. *Chemistry – A European Journal* **2021**, 27 (19), 5906–5912. <https://doi.org/10.1002/chem.202100387>.

(36) Morris, C. A.; Chen, C.-C.; Baker, L. A. Transport of Redox Probes through Single Pores Measured by Scanning Electrochemical-Scanning Ion Conductance Microscopy (SECM-SICM). *The Analyst* **2012**, 137 (13), 2933. <https://doi.org/10.1039/c2an16178h>.

(37) Wheeldon, I.; Minter, S. D.; Banta, S.; Barton, S. C.; Atanassov, P.; Sigman, M. Substrate Channelling as an Approach to Cascade Reactions. *Nature Chem* **2016**, 8 (4), 299–309. <https://doi.org/10.1038/nchem.2459>.

(38) Welch, A. J.; Fenwick, A. Q.; Böhme, A.; Chen, H.-Y.; Sullivan, I.; Li, X.; DuChene, J. S.; Xiang, C.; Atwater, H. A. Operando Local pH Measurement within Gas Diffusion Electrodes Performing Electrochemical Carbon Dioxide Reduction. *J. Phys. Chem. C* **2021**, 125 (38), 20896–20904. <https://doi.org/10.1021/acs.jpcc.1c06265>.

(39) Perez, J.; Gonzalez, E. R.; Villullas, H. M. Hydrogen Evolution Reaction on Gold Single-Crystal Electrodes in Acid Solutions. *J. Phys. Chem. B* **1998**, 102 (52), 10931–10935. <https://doi.org/10.1021/jp9831987>.

(40) Hamelin, A.; Weaver, M. J. Dependence of the Kinetics of Proton Reduction at Gold Electrodes on the Surface Crystallographic Orientation. *Journal of Electroanalytical Chemistry and Interfacial Electrochemistry* **1987**, 223 (1), 171–184. [https://doi.org/10.1016/0022-0728\(87\)85258-0](https://doi.org/10.1016/0022-0728(87)85258-0).

(41) Varela, A. S.; Kroschel, M.; Reier, T.; Strasser, P. Controlling the Selectivity of CO₂ Electroreduction on Copper: The Effect of the Electrolyte Concentration and the Importance of the Local pH. *Catalysis Today* **2016**, 260, 8–13. <https://doi.org/10.1016/j.cattod.2015.06.009>.

(42) Qi, K.; Zhang, Y.; Li, J.; Charmette, C.; Ramonda, M.; Cui, X.; Wang, Y.; Zhang, Y.; Wu, H.; Wang, W.; Zhang, X.; Voiry, D. Enhancing the CO₂-to-CO Conversion from 2D Silver Nanoprisms via Superstructure Assembly. *ACS Nano* **2021**, 15 (4), 7682–7693. <https://doi.org/10/gmx788>.

(43) Binnig, G.; Rohrer, H. Scanning Tunneling Microscopy. *Surface Science* **1983**, 126 (1), 236–244. [https://doi.org/10.1016/0039-6028\(83\)90716-1](https://doi.org/10.1016/0039-6028(83)90716-1).

(44) Binnig, G.; Quate, C. F.; Gerber, Ch. Atomic Force Microscope. *Phys. Rev. Lett.* **1986**, 56 (9), 930–933. <https://doi.org/10.1103/PhysRevLett.56.930>.

(45) SALAPAKA, S. M.; SALAPAKA, M. V. Scanning Probe Microscopy. *IEEE Control Systems Magazine* **2008**, 28 (2), 65–83. <https://doi.org/10.1109/MCS.2007.914688>.

(46) Hoppert, M. Scanning Probe Microscopy (Includes Atomic Force Microscopy). In *Encyclopedia of Geobiology*; Reitner, J., Thiel, V., Eds.; Springer Netherlands: Dordrecht, 2011; pp 772–777. https://doi.org/10.1007/978-1-4020-9212-1_15.

- (47) Wiesendanger, R. Scanning-Probe-Based Science and Technology. *PNAS* **1997**, *94* (24), 12749–12750. <https://doi.org/10.1073/pnas.94.24.12749>.
- (48) Bard, A. J.; Fan, F.-R. F.; Kwak, J.; Lev, O. Scanning Electrochemical Microscopy. Introduction and Principles. *Analytical Chemistry* **1989**, *61* (2), 132–138. <https://doi.org/10.1021/ac00177a011>.
- (49) Kwak, J.; Bard, A. J. Scanning Electrochemical Microscopy. Theory of the Feedback Mode. *Analytical Chemistry* **1989**, *61* (11), 1221–1227. <https://doi.org/10.1021/ac00186a009>.
- (50) Perry, D.; Al Botros, R.; Momotenko, D.; Kinnear, S. L.; Unwin, P. R. Simultaneous Nanoscale Surface Charge and Topographical Mapping. *ACS Nano* **2015**, *9* (7), 7266–7276. <https://doi.org/10.1021/acsnano.5b02095>.
- (51) Plettenberg, I.; Wittstock, G. Combined Detection of Electrochemical Reactions and Topographical Effects - Imaging with Scanning Ohmic Microscopy. *Electrochimica Acta* **2016**, *197*, 318–329. <https://doi.org/10.1016/j.electacta.2015.12.033>.
- (52) Matsue, T.; Takahashi, Y.; Shevchuk, A. I.; Novak, P.; Murakami, Y.; Shiku, H.; Korchev, Y. E.; Matsue, T. Simultaneous Noncontact Topography and Electrochemical Imaging by SECM/SICM Featuring Ion Current Feedback Regulation. *Journal of the American Chemical Society* **2010**, *132* (29), 10118–10126. <https://doi.org/10.1021/ja1029478>.
- (53) Kim, J.; Renault, C.; Nioradze, N.; Arroyo-Currás, N.; Leonard, K. C.; Bard, A. J. Electrocatalytic Activity of Individual Pt Nanoparticles Studied by Nanoscale Scanning Electrochemical Microscopy. *Journal of the American Chemical Society* **2016**, *138* (27), 8560–8568. <https://doi.org/10.1021/jacs.6b03980>.
- (54) Nogala, W.; Celebanska, A.; Szot, K.; Wittstock, G.; Opallo, M. Bioelectrocatalytic Mediatorless Dioxygen Reduction at Carbon Ceramic Electrodes Modified with Bilirubin Oxidase. *Electrochimica Acta* **2010**, *55* (20), 5719–5724. <https://doi.org/10.1016/j.electacta.2010.05.007>.
- (55) O'Connell, M. A.; Wain, A. J. Mapping Electroactivity at Individual Catalytic Nanostructures Using High-Resolution Scanning Electrochemical–Scanning Ion Conductance Microscopy. *Analytical Chemistry* **2014**, *86* (24), 12100–12107. <https://doi.org/10.1021/ac502946q>.
- (56) Pust, S. E.; Salomo, M.; Oesterschulze, E.; Wittstock, G. Influence of Electrode Size and Geometry on Electrochemical Experiments with Combined SECM–SFM Probes. *Nanotechnology* **2010**, *21* (10), 105709. <https://doi.org/10.1088/0957-4484/21/10/105709>.
- (57) Izquierdo, J.; Knittel, P.; Kranz, C. Scanning Electrochemical Microscopy: An Analytical Perspective. *Anal Bioanal Chem* **2018**, *410* (2), 307–324. <https://doi.org/10.1007/s00216-017-0742-7>.

- (58) Jacobse, L.; Raaijman, S. J.; Koper, M. T. M. The Reactivity of Platinum Microelectrodes. *Physical Chemistry Chemical Physics* **2016**, *18* (41), 28451–28457. <https://doi.org/10.1039/C6CP05361K>.
- (59) Diaz-Morales, O.; Ferrus-Suspedra, D.; Koper, M. T. M. The Importance of Nickel Oxyhydroxide Deprotonation on Its Activity towards Electrochemical Water Oxidation. *Chemical Science* **2016**, *7* (4), 2639–2645. <https://doi.org/10.1039/c5sc04486c>.
- (60) Uitto, O. D.; White, H. S.; Aoki, K. Diffusive-Convective Transport into a Porous Membrane. A Comparison of Theory and Experiment Using Scanning Electrochemical Microscopy Operated in Reverse Imaging Mode. *Analytical Chemistry* **2002**, *74* (17), 4577–4582. <https://doi.org/10.1021/ac0256538>.
- (61) Gardner, C. E.; Unwin, P. R.; Macpherson, J. V. Correlation of Membrane Structure and Transport Activity Using Combined Scanning Electrochemical–Atomic Force Microscopy. *Electrochemistry Communications* **2005**, *7* (6), 612–618. <https://doi.org/10.1016/j.elecom.2005.04.005>.
- (62) Arca, M.; Mirkin, M. V.; Bard, A. J. Polymer Films on Electrodes. 26. Study of Ion Transport and Electron Transfer at Polypyrrole Films by Scanning Electrochemical Microscopy. *J. Phys. Chem* **1995**, *99*, 5040–5050.
- (63) Kueng, A.; Kranz, C.; Lugstein, A.; Bertagnolli, E.; Mizaikoff, B. A FM-Tip-Integrated Amperometric Microbiosensors: High-Resolution Imaging of Membrane Transport. *Angewandte Chemie - International Edition* **2005**, *44* (22), 3419–3422. <https://doi.org/10.1002/anie.200461556>.
- (64) Goyal, A.; Marcandalli, G.; Mints, V. A.; Koper, M. T. M. Competition between CO₂ Reduction and Hydrogen Evolution on a Gold Electrode under Well-Defined Mass Transport Conditions. *J Am Chem Soc* **2020**, *142* (9), 4154–4161. <https://doi.org/10/gg84dq>.
- (65) Dunwell, M.; Yang, X.; Setzler, B. P.; Anibal, J.; Yan, Y.; Xu, B. Examination of Near-Electrode Concentration Gradients and Kinetic Impacts on the Electrochemical Reduction of CO₂ Using Surface-Enhanced Infrared Spectroscopy. *ACS Catal.* **2018**, *8* (5), 3999–4008. <https://doi.org/10.1021/acscatal.8b01032>.
- (66) Kas, R.; Kortlever, R.; Yilmaz, H.; Koper, M. T. M.; Mul, G. Manipulating the Hydrocarbon Selectivity of Copper Nanoparticles in CO₂ Electroreduction by Process Conditions. *ChemElectroChem* **2015**, *2* (3), 354–358. <https://doi.org/10.1002/celec.201402373>.
- (67) Macpherson, J. V.; Jones, C. E.; Barker, A. L.; Unwin, P. R. Electrochemical Imaging of Diffusion through Single Nanoscale Pores. *Analytical Chemistry* **2002**, *74* (8), 1841–1848. <https://doi.org/10.1021/ac0157472>.
- (68) Wittstock, G.; Burchardt, M.; Pust, S. E.; Shen, Y.; Zhao, C. Scanning Electrochemical Microscopy for Direct Imaging of Reaction Rates. *Angewandte Chemie - International Edition* **2007**, *46* (10), 1584–1617. <https://doi.org/10.1002/anie.200602750>.

- (69) Seo, M. H.; Choi, S. M.; Seo, J. K.; Noh, S. H.; Kim, W. B.; Han, B. The Graphene-Supported Palladium and Palladium–Yttrium Nanoparticles for the Oxygen Reduction and Ethanol Oxidation Reactions: Experimental Measurement and Computational Validation. *Applied Catalysis B: Environmental* **2013**, *129*, 163–171. <https://doi.org/10.1016/j.apcatb.2012.09.005>.
- (70) Kim, J.; Renault, C.; Nioradze, N.; Arroyo-Curra, N.; Leonard, K. C.; Bard, A. J.; Arroyo, N.; Leonard, K. C.; Bard, A. J. Nanometer Scale Scanning Electrochemical Microscopy Instrumentation. *Analytical Chemistry* **2016**, *88* (20), acs.analchem.6b03024. <https://doi.org/10.1021/acs.analchem.6b03024>.
- (71) Diaz-Morales, O.; Ferrus-Suspedra, D.; Koper, M. T. M. The Importance of Nickel Oxyhydroxide Deprotonation on Its Activity towards Electrochemical Water Oxidation. *Chem. Sci.* **2016**, *7* (4), 2639–2645. <https://doi.org/10.1039/C5SC04486C>.
- (72) Mauzeroll, J.; Bard, A. J.; Owhadian, O.; Monks, T. J. Menadione Metabolism to Thiodione in Hepatoblastoma by Scanning Electrochemical Microscopy. *PNAS* **2004**, *101* (51), 17582–17587. <https://doi.org/10.1073/pnas.0407613101>.
- (73) Bard, A. J.; Mirkin, M. V.; Unwin, P. R.; Wipf, D. O. Scanning Electrochemical Microscopy. 12. Theory and Experiment of the Feedback Mode with Finite Heterogeneous Electron-Transfer Kinetics and Arbitrary Substrate Size. *The Journal of Physical Chemistry* **1992**, *96* (4), 1861–1868. <https://doi.org/10.1021/j100183a064>.
- (74) Unwin, P. R.; Bard, A. J. Scanning Electrochemical Microscopy. 9. Theory and Application of the Feedback Mode to the Measurement of Following Chemical Reaction Rates in Electrode Processes. *Journal of Physical Chemistry* **1991**, *95* (20), 7814–7824. <https://doi.org/10.1021/j100173a049>.
- (75) Bard, A.; Mirkin, M. *Scanning Electrochemical Microscopy, Second Edition*; CRC Press, 2012. <https://doi.org/10.1201/b11850>.
- (76) Demaille, C.; Unwin, P. R.; Bard, A. J. Scanning Electrochemical Microscopy. 33. Application to the Study of ECE/DISP Reactions. *J. Phys. Chem.* **1996**, *100* (33), 14137–14143. <https://doi.org/10.1021/jp9611380>.
- (77) Fernández, J. L.; Bard, A. J. Scanning Electrochemical Microscopy 50. Kinetic Study of Electrode Reactions by the Tip Generation–Substrate Collection Mode. *Anal. Chem.* **2004**, *76* (8), 2281–2289. <https://doi.org/10.1021/ac035518a>.
- (78) Pierce, D. T.; Unwin, P. R.; Bard, A. J. Scanning Electrochemical Microscopy. 17. Studies of Enzyme-Mediator Kinetics for Membrane- and Surface-Immobilized Glucose Oxidase. *Analytical Chemistry* **1992**, *64* (17), 1795–1804. <https://doi.org/10.1021/ac00041a011>.
- (79) Zaumseil, J.; Wittstock, G.; Bahrs, S.; Steinrücke, P. Imaging the Activity of Nitrate Reductase by Means of a Scanning Electrochemical Microscope. *Fresenius' journal of analytical chemistry* **2000**, *367* (4), 352–355. <https://doi.org/10.1007/s002160000370>.

- (80) Uitto, O. D.; White, H. S.; Aoki, K. Diffusive–Convective Transport into a Porous Membrane. A Comparison of Theory and Experiment Using Scanning Electrochemical Microscopy Operated in Reverse Imaging Mode. *Anal. Chem.* **2002**, *74* (17), 4577–4582. <https://doi.org/10.1021/ac0256538>.
- (81) Frederix, P. L. T. M.; Bosshart, P. D.; Akiyama, T.; Chami, M.; Gullo, M. R.; Blackstock, J. J.; Dooleweerd, K.; de Rooij, N. F.; Staufer, U.; Engel, A. Conductive Supports for Combined AFM–SECM on Biological Membranes. *Nanotechnology* **2008**, *19* (38), 384004. <https://doi.org/10.1088/0957-4484/19/38/384004>.
- (82) Shao, Y.; Mirkin, M. V. Probing Ion Transfer at the Liquid / Liquid Interface by Scanning Electrochemical Microscopy (SECM). *The Journal of Physical Chemistry B* **1998**, *102* (49), 9915–9921. <https://doi.org/10.1021/jp9828282>.
- (83) Wu, F.; Minter, S. Krebs Cycle Metabolon: Structural Evidence of Substrate Channeling Revealed by Cross-Linking and Mass Spectrometry. *Angewandte Chemie International Edition* **2015**, *54* (6), 1851–1854. <https://doi.org/10.1002/anie.201409336>.
- (84) Fu, J.; Yang, Y. R.; Johnson-Buck, A.; Liu, M.; Liu, Y.; Walter, N. G.; Woodbury, N. W.; Yan, H. Multi-Enzyme Complexes on DNA Scaffolds Capable of Substrate Channelling with an Artificial Swinging Arm. *Nature Nanotech* **2014**, *9* (7), 531–536. <https://doi.org/10.1038/nnano.2014.100>.
- (85) Liu, F.; Banta, S.; Chen, W. Functional Assembly of a Multi-Enzyme Methanol Oxidation Cascade on a Surface-Displayed Trifunctional Scaffold for Enhanced NADH Production. *Chem. Commun.* **2013**, *49* (36), 3766–3768. <https://doi.org/10.1039/C3CC40454D>.
- (86) Lu, F.; Jin, M.; Belkin, M. A. Tip-Enhanced Infrared Nanospectroscopy via Molecular Expansion Force Detection. *Nature Photonics* **2014**, *8* (4), 307–312. <https://doi.org/10.1038/nphoton.2013.373>.
- (87) Verma, P. Tip-Enhanced Raman Spectroscopy: Technique and Recent Advances. *Chemical Reviews*. American Chemical Society May 10, 2017, pp 6447–6466. <https://doi.org/10.1021/acs.chemrev.6b00821>.
- (88) Larmour, I. A.; Faulds, K.; Graham, D. The Past, Present and Future of Enzyme Measurements Using Surface Enhanced Raman Spectroscopy. *Chemical Science* **2010**, *1* (2), 151. <https://doi.org/10.1039/c0sc00226g>.
- (89) Ding, S.-Y.; Yi, J.; Li, J.-F.; Ren, B.; Wu, D.-Y.; Panneerselvam, R.; Tian, Z.-Q. Nanostructure-Based Plasmon-Enhanced Raman Spectroscopy for Surface Analysis of Materials. *Nature Reviews Materials* **2016**, *1* (6), 16021. <https://doi.org/10.1038/natrevmats.2016.21>.
- (90) Jayaraman, S.; Hillier, A. C. Construction and Reactivity Mapping of a Platinum Catalyst Gradient Using the Scanning Electrochemical Microscope. *Langmuir* **2001**, *17* (25), 7857–7864. <https://doi.org/10.1021/la010930b>.

- (91) Monteiro, M. C. O.; Jacobse, L.; Touzalin, T.; Koper, M. T. M. Mediator-Free SECM for Probing the Diffusion Layer PH with Functionalized Gold Ultramicroelectrodes. *Anal. Chem.* **2020**, 92 (2), 2237–2243. <https://doi.org/10.1021/acs.analchem.9b04952>.
- (92) Xie, X. S.; Trautman, J. K. OPTICAL STUDIES OF SINGLE MOLECULES AT ROOM TEMPERATURE. *Annual Review of Physical Chemistry* **1998**, 49 (1), 441–480. <https://doi.org/10.1146/annurev.physchem.49.1.441>.
- (93) Zhou, X.; Andoy, N. M.; Liu, G.; Choudhary, E.; Han, K. S.; Shen, H.; Chen, P. Quantitative Super-Resolution Imaging Uncovers Reactivity Patterns on Single Nanocatalysts. *Nature Nanotechnology* **2012**, 7 (4), 237–241. <https://doi.org/10.1038/nnano.2012.18>.
- (94) Zaera, F. Surface Chemistry at the Liquid/Solid Interface. *Surface Science* **2011**, 605 (13), 1141–1145. <https://doi.org/10.1016/j.susc.2011.04.021>.
- (95) Brown, M. A.; Jordan, I.; Belouqui Redondo, A.; Kleibert, A.; Wörner, H. J.; van Bokhoven, J. A. In Situ Photoelectron Spectroscopy at the Liquid/Nanoparticle Interface. *Surface Science* **2013**, 610, 1–6. <https://doi.org/10.1016/j.susc.2013.01.012>.
- (96) Kolagatla, S.; Subramanian, P.; Schechter, A. Nanoscale Mapping of Catalytic Hotspots on Fe, N-Modified HOPG by Scanning Electrochemical Microscopy-Atomic Force Microscopy. *Nanoscale* **2018**, 10 (15), 6962–6970. <https://doi.org/10.1039/C8NR00849C>.
- (97) Mangun, C. L.; Benak, K. R.; Economy, J.; Foster, K. L. Surface Chemistry, Pore Sizes and Adsorption Properties of Activated Carbon Fibers and Precursors Treated with Ammonia. *Carbon* **2001**, 39 (12), 1809–1820. [https://doi.org/10.1016/S0008-6223\(00\)00319-5](https://doi.org/10.1016/S0008-6223(00)00319-5).
- (98) Banerjee, S.; Sarkar, P.; Turner, A. P. F. Amperometric Biosensor Based on Prussian Blue Nanoparticle-Modified Screen-Printed Electrode for Estimation of Glucose-6-Phosphate. *Analytical Biochemistry* **2013**, 439 (2), 194–200. <https://doi.org/10.1016/j.ab.2013.04.025>.
- (99) Kuhnke, K.; Große, C.; Merino, P.; Kern, K. Atomic-Scale Imaging and Spectroscopy of Electroluminescence at Molecular Interfaces. *Chemical Reviews*. American Chemical Society March 15, 2017, pp 5174–5222. <https://doi.org/10.1021/acs.chemrev.6b00645>.
- (100) Liu, H.; Fan, F.; Lin, C.; Bard, A. Scanning Electrochemical and Tunneling Ultramicroelectrode Microscope for High-Resolution Examination of Electrode Surfaces in Solution. *Journal of the American Chemical Society* **1986**, 108 (13), 3838–3839. <https://doi.org/10.1021/ja00273a054>.
- (101) Moon, J.-S.; Wiedemair, J.; Masson, J.-F.; Mizaikoff, B.; Kranz, C. Atomic Force Scanning Electrochemical Microscopy (AFM-SECM) for Electrochemical Imaging at the Nanoscale. *Microscopy and Microanalysis* **2007**, 13 (S02), 58–59. <https://doi.org/10.1017/S1431927607073734>.
- (102) Edwards, M. A.; Robinson, D. A.; Ren, H.; Cheyne, C. G.; Tan, C. S.; White, H. S. Nanoscale Electrochemical Kinetics & Dynamics: The Challenges and Opportunities of Single-Entity Measurements. *Faraday Discussions* **2018**. <https://doi.org/10.1039/C8FD00134K>.

- (103) Kang, M.; Momotenko, D.; Page, A.; Perry, D.; Unwin, P. R. Frontiers in Nanoscale Electrochemical Imaging: Faster, Multifunctional, and Ultrasensitive. *Langmuir* **2016**, *32* (32). <https://doi.org/10.1021/acs.langmuir.6b01932>.
- (104) Kranz, C. Recent Advancements in Nanoelectrodes and Nanopipettes Used in Combined Scanning Electrochemical Microscopy Techniques. *Analyst* **2014**, *139* (2), 336–352. <https://doi.org/10.1039/c3an01651j>.
- (105) Clausmeyer, J.; Schuhmann, W. Nanoelectrodes: Applications in Electrocatalysis, Single-Cell Analysis and High-Resolution Electrochemical Imaging. *TrAC Trends in Analytical Chemistry* **2016**, *79*, 46–59. <https://doi.org/10.1016/j.trac.2016.01.018>.
- (106) Rudd, N. C.; Cannan, S.; Bitziou, E.; Ciani, I.; Whitworth, A. L.; Unwin, P. R. Fluorescence Confocal Laser Scanning Microscopy as a Probe of PH Gradients in Electrode Reactions and Surface Activity. *Anal. Chem.* **2005**, *77* (19), 6205–6217. <https://doi.org/10.1021/ac050800y>.
- (107) Henckel, D. A.; Counihan, M. J.; Holmes, H. E.; Chen, X.; Nwabara, U. O.; Verma, S.; Rodríguez-López, J.; Kenis, P. J. A.; Gewirth, A. A. Potential Dependence of the Local PH in a CO₂ Reduction Electrolyzer. *ACS Catal.* **2021**, *11* (1), 255–263. <https://doi.org/10/gmtzfm>.
- (108) Ataka, K.; Stripp, S. T.; Heberle, J. Surface-Enhanced Infrared Absorption Spectroscopy (SEIRAS) to Probe Monolayers of Membrane Proteins. *Biochimica et Biophysica Acta (BBA) - Biomembranes* **2013**, *1828* (10), 2283–2293. <https://doi.org/10.1016/j.bbamem.2013.04.026>.
- (109) Morhart, T. A.; Unni, B.; Lardner, M. J.; Burgess, I. J. Electrochemical ATR-SEIRAS Using Low-Cost, Micromachined Si Wafers. *Anal. Chem.* **2017**, *89* (21), 11818–11824. <https://doi.org/10.1021/acs.analchem.7b03509>.
- (110) Pierce, D. T.; Bard, A. J. Scanning Electrochemical Microscopy. 23. Reaction Localization of Artificially Patterned and Tissue-Bound Enzymes. *Analytical Chemistry* **1993**, *65* (24), 3598–3604. <https://doi.org/10.1021/ac00072a012>.
- (111) Kueng, A.; Kranz, C.; Lugstein, A.; Bertagnolli, E.; Mizaikoff, B. Integrated AFM-SECM in Tapping Mode: Simultaneous Topographical and Electrochemical Imaging of Enzyme Activity. *Angewandte Chemie - International Edition* **2003**, *42* (28), 3238–3240. <https://doi.org/10.1002/anie.200351111>.
- (112) Kranz, C.; Kueng, A.; Lugstein, A.; Bertagnolli, E.; Mizaikoff, B. Mapping of Enzyme Activity by Detection of Enzymatic Products during AFM Imaging with Integrated SECM-AFM Probes. In *Ultramicroscopy*; 2004; Vol. 100, pp 127–134. <https://doi.org/10.1016/j.ultramic.2003.10.004>.
- (113) Kranz, C.; Wittstock, G.; Wohlschläger, H.; Schuhmann, W. Imaging of Microstructured Biochemically Active Surfaces by Means of Scanning Electrochemical Microscopy. *Electrochimica Acta* **1997**, *42* (20–22), 3105–3111. [https://doi.org/10.1016/S0013-4686\(97\)00158-8](https://doi.org/10.1016/S0013-4686(97)00158-8).

- (114) Hengstenberg, A.; Kranz, C.; Schuhmann, W. Facilitated Tip-Positioning and Applications of Non-Electrode Tips in Scanning Electrochemical Microscopy Using a Shear Force Based Constant-Distance Mode. *Chemistry - A European Journal* **2000**, 6 (9), 1547–1554. [https://doi.org/10.1002/\(SICI\)1521-3765\(20000502\)6:9<1547::AID-CHEM1547>3.3.CO;2-3](https://doi.org/10.1002/(SICI)1521-3765(20000502)6:9<1547::AID-CHEM1547>3.3.CO;2-3).
- (115) Wittstock, G.; Schuhmann, W. Formation and Imaging of Microscopic Enzymatically Active Spots on an Alkanethiolate-Covered Gold Electrode by Scanning Electrochemical Microscopy. *Anal. Chem.* **1997**, 69 (24), 5059–5066. <https://doi.org/10.1021/ac970504o>.
- (116) De Viveiros, B. V. G.; Donatus, U.; Cavalieri De Alencar, M.; Berbel, L. O.; Costa, I. Comparing the Corrosion Behaviour of AA2050 and AA7050 Aluminium Alloys by Scanning Vibrating Electrode and Scanning Ion-Selective Electrode Techniques. *Corrosion Engineering, Science and Technology* **2021**, 0 (0), 1–12. <https://doi.org/10.1080/1478422X.2021.1992132>.
- (117) Matsue, T.; Takahashi, Y.; Shevchuk, A. I.; Novak, P.; Murakami, Y.; Shiku, H.; Korchev, Y. E. Simultaneous Noncontact Topography and Electrochemical Imaging by SECM/SICM Featuring Ion Current Feedback Regulation. *Journal of the American Chemical Society* **2010**, 132 (29), 10118–10126. <https://doi.org/10.1021/ja1029478>.
- (118) Darby, M. T.; Sykes, E. C. H.; Michaelides, A.; Stamatakis, M. Carbon Monoxide Poisoning Resistance and Structural Stability of Single Atom Alloys. *Top Catal* **2018**, 61 (5), 428–438. <https://doi.org/10.1007/s11244-017-0882-1>.
- (119) Alex Mirabal; Scott Calabrese Barton. Numerical Correction of In Situ AFM-SECM Measurements | Analytical Chemistry. <https://doi.org/10.1021/acs.analchem.1c00770>.
- (120) Kueng, A.; Kranz, C.; Lugstein, A.; Bertagnolli, E.; Mizaikoff, B. Integrated AFM-SECM in Tapping Mode: Simultaneous Topographical and Electrochemical Imaging of Enzyme Activity. *Angewandte Chemie - International Edition* **2003**, 42 (28), 3238–3240. <https://doi.org/10.1002/anie.200351111>.
- (121) Nebel, M.; Eckhard, K.; Erichsen, T.; Schulte, A.; Schuhmann, W. 4D Shearforce-Based Constant-Distance Mode Scanning Electrochemical Microscopy. *Analytical Chemistry* **2010**, 82 (18), 7842–7848. <https://doi.org/10.1021/ac1008805>.
- (122) Darvishi, S.; Pick, H.; Lin, T.-E.; Zhu, Y.; Li, X.; Ho, P.-C.; Girault, H. H.; Lesch, A. Tape-Stripping Electrochemical Detection of Melanoma. *Anal. Chem.* **2019**, 91 (20), 12900–12908. <https://doi.org/10.1021/acs.analchem.9b02819>.
- (123) Mirkin, M. V.; Richards, T. C.; Bard, A. J. Scanning Electrochemical Microscopy. 20. Steady-State Measurements of the Fast Heterogeneous Kinetics in the Ferrocene/Acetonitrile System. *Journal of Physical Chemistry* **1993**, 97 (29), 7672–7677. <https://doi.org/10.1021/j100131a042>.
- (124) Bard, A. J.; Denuault, G.; Lee, C.; Mandler, D.; Wipf, D. O. Scanning Electrochemical Microscopy: A New Technique for the Characterization and Modification of Surfaces. *Accounts of Chemical Research* **1990**, 23 (11), 357–363. <https://doi.org/10.1021/ar00179a002>.

- (125) Hansma, P.; Drake, B.; Marti, O.; Gould, S.; Prater, C. The Scanning Ion-Conductance Microscope. *Science* **1989**, *243* (4891), 641–643. <https://doi.org/10.1126/science.2464851>.
- (126) Korchev, Y. E. Y. E.; Bashford, C. L. L.; Milovanovic, M.; Vodyanoy, I.; Lab, M. J. M. J. M. J. Scanning Ion Conductance Microscopy of Living Cells. *Biophysical journal* **1997**, *73* (2), 653–658. [https://doi.org/10.1016/S0006-3495\(97\)78100-1](https://doi.org/10.1016/S0006-3495(97)78100-1).
- (127) Ebejer, N.; Güell, A. G.; Lai, S. C. S.; McKelvey, K.; Snowden, M. E.; Unwin, P. R. Scanning Electrochemical Cell Microscopy: A Versatile Technique for Nanoscale Electrochemistry and Functional Imaging. *Annual Review of Analytical Chemistry* **2013**, *6* (1), 329–351. <https://doi.org/10.1146/annurev-anchem-062012-092650>.
- (128) Hengstenberg, A.; Kranz, C.; Schuhmann, W. Facilitated Tip-Positioning and Applications of Non-Electrode Tips in Scanning Electrochemical Microscopy Using a Shear Force Based Constant-Distance Mode. *Chemistry - A European Journal* **2000**, *6* (9), 1547–1554. [https://doi.org/10.1002/\(SICI\)1521-3765\(20000502\)6:9<1547::AID-CHEM1547>3.3.CO;2-3](https://doi.org/10.1002/(SICI)1521-3765(20000502)6:9<1547::AID-CHEM1547>3.3.CO;2-3).
- (129) Ludwig, M.; Kranz, C.; Schuhmann, W.; Gaub, H. E. Topography Feedback Mechanism for the Scanning Electrochemical Microscope Based on Hydrodynamic Forces between Tip and Sample. *Review of Scientific Instruments* **1995**, *66* (4), 2857. <https://doi.org/10.1063/1.1145568>.
- (130) Macpherson, J. V.; Unwin, P. R. Combined Scanning Electrochemical–Atomic Force Microscopy. *Analytical Chemistry* **2000**, *72* (2), 276–285. <https://doi.org/10.1021/ac990921w>.
- (131) Alessandrini, A.; Facci, P. AFM: A Versatile Tool in Biophysics. *Meas. Sci. Technol.* **2005**, *16* (6), R65–R92. <https://doi.org/10.1088/0957-0233/16/6/R01>.
- (132) Revenko, I.; Proksch, R. Magnetic and Acoustic Tapping Mode Microscopy of Liquid Phase Phospholipid Bilayers and DNA Molecules. *Journal of Applied Physics* **2000**, *87* (1), 526–533. <https://doi.org/10.1063/1.371894>.
- (133) Melitz, W.; Shen, J.; Kummel, A. C.; Lee, S. Kelvin Probe Force Microscopy and Its Application. *Surface Science Reports* **2011**, *66* (1), 1–27. <https://doi.org/10.1016/j.surfrep.2010.10.001>.
- (134) Huang, Z.; Wolf, P. D.; Poddar, R.; Li, C.; Mark, A.; Nellist, M. R.; Chen, Y.; Jiang, J.; Papastavrou, G.; Boettcher, S. W.; Xiang, C.; Brunschwig, B. S. PeakForce Scanning Electrochemical Microscopy with Nanoelectrode Probes. *Microsc. Today* **2016**, *24* (November), 18–25. <https://doi.org/10.1017/S1551929516000882>.
- (135) Kai, T.; Zoski, C. G.; Bard, A. J. Scanning Electrochemical Microscopy at the Nanometer Level. *Chemical Communications* **2018**, *54* (16), 1934–1947. <https://doi.org/10.1039/C7CC09777H>.
- (136) Kim, J.; Renault, C.; Nioradze, N.; Arroyo-Curra, N.; Leonard, K. C.; Bard, A. J.; Arroyo, N.; Leonard, K. C.; Bard, A. J. Nanometer Scale Scanning Electrochemical Microscopy Instrumentation. *Analytical Chemistry* **2016**, *88* (20), acs.analchem.6b03024. <https://doi.org/10.1021/acs.analchem.6b03024>.

- (137) Dobson, P. S.; Weaver, J. M. R.; Holder, M. N.; Unwin, P. R.; Macpherson, J. V. In Situ Scanning Electrochemical Probe Microscopy for Energy Applications. *Analytical Chemistry* **2005**, *74* (7), 668–674. <https://doi.org/10.1557/mrs.2012.146>.
- (138) Zoski, C. G. Nanoscale Scanning Electrochemical Microscopy: Emerging Advances in Applications and Theory. *Current Opinion in Electrochemistry* **2017**, *1* (1), 46–52. <https://doi.org/10/gmfz72>.
- (139) Jones, C. E.; Macpherson, J. V.; Barber, Z. H.; Somekh, R. E.; Unwin, P. R. Simultaneous Topographical and Amperometric Imaging of Surfaces in Air: Towards a Combined Scanning Force–Scanning Electrochemical Microscope (SF–SECM). *Electrochemistry Communications* **1999**, *1* (2), 55–60. [https://doi.org/10.1016/S1388-2481\(99\)00004-1](https://doi.org/10.1016/S1388-2481(99)00004-1).
- (140) Bard, A. J.; Mirkin, M. V.; Unwin, P. R.; Wipf, D. O. Scanning Electrochemical Microscopy. 12. Theory and Experiment of the Feedback Mode with Finite Heterogeneous Electron-Transfer Kinetics and Arbitrary Substrate Size. *Journal of Physical Chemistry* **1992**, *96* (4), 1861–1868. <https://doi.org/10.1021/j100183a064>.
- (141) Nellist, M. R.; Chen, Y.; Mark, A.; Gödrich, S.; Stelling, C.; Jiang, J.; Poddar, R.; Li, C.; Kumar, R.; Papastavrou, G.; Retsch, M.; Brunschwig, B. S.; Huang, Z.; Xiang, C.; Boettcher, S. W. Atomic Force Microscopy with Nanoelectrode Tips for High Resolution Electrochemical, Nanoadhesion and Nanoelectrical Imaging. *Nanotechnology* **2017**, *28* (9), 095711. <https://doi.org/10.1088/1361-6528/aa5839>.
- (142) Knittel, P.; Mizaikoff, B.; Kranz, C. Simultaneous Nanomechanical and Electrochemical Mapping: Combining Peak Force Tapping Atomic Force Microscopy with Scanning Electrochemical Microscopy. *Analytical Chemistry* **2016**, *88* (12), 6174–6178. <https://doi.org/10.1021/acs.analchem.6b01086>.
- (143) Mirkin, M. V.; Sun, T.; Yu, Y.; Zhou, M. Electrochemistry at One Nanoparticle. *Accounts of Chemical Research* **2016**, *49* (10), 2328–2335. <https://doi.org/10.1021/acs.accounts.6b00294>.
- (144) Katemann, B. B.; Schuhmann, W. Fabrication and Characterization of Needle-Type Pt-Disk Nanoelectrodes. *Electroanalysis* **2002**, *14* (1), 22–28. [https://doi.org/10.1002/1521-4109\(200201\)14:1<22::AID-ELAN22>3.0.CO;2-F](https://doi.org/10.1002/1521-4109(200201)14:1<22::AID-ELAN22>3.0.CO;2-F).
- (145) Bard, A. J.; Faulkner, L. R.; York, N.; @bullet, C.; Brisbane, W.; Toronto, S. E. *ELECTROCHEMICAL METHODS Fundamentals and Applications*; 1944.
- (146) Kwak, J.; Bard, A. J. Scanning Electrochemical Microscopy. Apparatus and Two-Dimensional Scans of Conductive and Insulating Substrates. *Analytical Chemistry* **1989**, *61* (17), 1794–1799. <https://doi.org/10.1021/ac00192a003>.
- (147) Bard, A. J.; Fan, F.-R. F.; Kwak, J.; Lev, O. Scanning Electrochemical Microscopy. Introduction and Principles. *Analytical Chemistry* **1989**, *61* (2), 132–138. <https://doi.org/10.1021/ac00177a011>.

- (148) Amphlett, J. L.; Denuault, G. Scanning Electrochemical Microscopy (SECM): An Investigation of the Effects of Tip Geometry on Amperometric Tip Response. *The Journal of Physical Chemistry B* **1998**, *102* (49), 9946–9951. <https://doi.org/10.1021/jp982829u>.
- (149) Mirkin, M. V.; Fan, F.-R. F.; Bard, A. J. Scanning Electrochemical Microscopy Part 13. Evaluation of the Tip Shapes of Nanometer Size Microelectrodes. *Journal of Electroanalytical Chemistry* **1992**, *328* (1–2), 47–62. [https://doi.org/10.1016/0022-0728\(92\)80169-5](https://doi.org/10.1016/0022-0728(92)80169-5).
- (150) Critelli, R. A. J.; Bertotti, M.; Torresi, R. M. Probe Effects on Concentration Profiles in the Diffusion Layer: Computational Modeling and near-Surface PH Measurements Using Microelectrodes. *Electrochimica Acta* **2018**, *292*, 511–521. <https://doi.org/10.1016/j.electacta.2018.09.157>.
- (151) Zhu, Y.; Wang, J.; Chu, H.; Chu, Y.-C.; Chen, H. M. In Situ/Operando Studies for Designing Next-Generation Electrocatalysts. *ACS Energy Lett.* **2020**, *5* (4), 1281–1291. <https://doi.org/10.1021/acsenenergylett.0c00305>.
- (152) Brenner, S. C.; Scott, L. R. The Construction of a Finite Element Space. In *The Mathematical Theory of Finite Element Methods*; Brenner, S. C., Scott, L. R., Eds.; Texts in Applied Mathematics; Springer: New York, NY, 1994; pp 67–90. https://doi.org/10.1007/978-1-4757-4338-8_4.
- (153) Brenner, S. C.; Scott, L. R. Basic Concepts. In *The Mathematical Theory of Finite Element Methods*; Brenner, S. C., Scott, L. R., Eds.; Texts in Applied Mathematics; Springer: New York, NY, 1994; pp 1–20. https://doi.org/10.1007/978-1-4757-4338-8_1.
- (154) Kasas, S.; Gmur, T.; Dietler, G. Chapter Eleven - Finite-Element Analysis of Microbiological Structures. In *The World of Nano-Biomechanics (Second Edition)*; Ikai, A., Ed.; Elsevier: Amsterdam, 2017; pp 199–218. <https://doi.org/10.1016/B978-0-444-63686-7.00011-0>.
- (155) Zhang, H.; Šavija, B.; Luković, M.; Schlangen, E. Experimentally Informed Micromechanical Modelling of Cement Paste: An Approach Coupling X-Ray Computed Tomography and Statistical Nanoindentation. *Composites Part B: Engineering* **2019**, *157*, 109–122. <https://doi.org/10.1016/j.compositesb.2018.08.102>.
- (156) Dobson, P. S.; Weaver, J. M. R.; Holder, M. N.; Unwin, P. R.; Macpherson, J. V. Characterization of Batch-Microfabricated Scanning Electrochemical-Atomic Force Microscopy Probes. *Anal. Chem.* **2005**, *77* (2), 424–434. <https://doi.org/10.1021/ac048930e>.
- (157) Lazenby, R. A.; McKelvey, K.; Unwin, P. R. Hopping Intermittent Contact-Scanning Electrochemical Microscopy (HIC-SECM): Visualizing Interfacial Reactions and Fluxes from Surfaces to Bulk Solution. *Analytical Chemistry* **2013**, *85* (5), 2937–2944. <https://doi.org/10.1021/ac303642p>.
- (158) Nellist, M. R.; Chen, Y.; Mark, A.; Gödrich, S.; Stelling, C.; Jiang, J.; Poddar, R.; Li, C.; Kumar, R.; Papastavrou, G.; Retsch, M.; Brunschwig, B. S.; Huang, Z.; Xiang, C.; Boettcher, S. W. Atomic Force Microscopy with Nanoelectrode Tips for High Resolution Electrochemical,

Nanoadhesion and Nanoelectrical Imaging. *Nanotechnology* **2017**, 28 (9), 095711.
<https://doi.org/10.1088/1361-6528/aa5839>.

(159) Fulian, Q.; Fisher, A. C.; Denuault, G. Applications of the Boundary Element Method in Electrochemistry: Scanning Electrochemical Microscopy. *J. Phys. Chem. B* **1999**, 103 (21), 4387–4392. <https://doi.org/10.1021/jp983732a>.

(160) Fulian, Q.; Fisher, A. C.; Denuault, G. Applications of the Boundary Element Method in Electrochemistry: Scanning Electrochemical Microscopy, Part 2. *J. Phys. Chem. B* **1999**, 103 (21), 4393–4398. <https://doi.org/10.1021/jp983993k>.

(161) Sklyar, O.; Wittstock, G. Numerical Simulations of Complex Nonsymmetrical 3D Systems for Scanning Electrochemical Microscopy Using the Boundary Element Method. *J. Phys. Chem. B* **2002**, 106 (30), 7499–7508. <https://doi.org/10.1021/jp020301q>.

(162) Sklyar, O.; Träuble, M.; Zhao, C.; Wittstock, G. Modeling Steady-State Experiments with a Scanning Electrochemical Microscope Involving Several Independent Diffusing Species Using the Boundary Element Method. *Journal of Physical Chemistry B* **2006**, 110 (32), 15869–15877. <https://doi.org/10.1021/jp062619e>.

(163) Sklyar, O.; Kueng, A.; Kranz, C.; Mizaikoff, B.; Lugstein, A.; Bertagnolli, E.; Wittstock, G. Numerical Simulation of Scanning Electrochemical Microscopy Experiments with Frame-Shaped Integrated Atomic Force Microscopy–SECM Probes Using the Boundary Element Method. *Anal. Chem.* **2005**, 77 (3), 764–771. <https://doi.org/10.1021/ac048732n>.

(164) Sklyar, O.; Ufheil, J.; Heinze, J.; Wittstock, G. Application of the Boundary Element Method Numerical Simulations for Characterization of Heptode Ultramicroelectrodes in SECM Experiments. *Electrochimica Acta* **2003**, 49 (1), 117–128.
<https://doi.org/10.1016/j.electacta.2003.04.007>.

(165) Stephens, L. I.; Mauzeroll, J. Altered Spatial Resolution of Scanning Electrochemical Microscopy Induced by Multifunctional Dual-Barrel Microelectrodes. *Analytical Chemistry* **2018**, 90 (11), 6796–6803. <https://doi.org/10.1021/acs.analchem.8b00821>.

(166) Stephens, L. I.; Payne, N. A.; Skaanvik, S. A.; Polcari, D.; Geissler, M.; Mauzeroll, J. Evaluating the Use of Edge Detection in Extracting Feature Size from Scanning Electrochemical Microscopy Images. *Anal. Chem.* **2019**, 91 (6), 3944–3950.
<https://doi.org/10.1021/acs.analchem.8b05011>.

(167) Carneiro-Neto, E. B.; Lopes, M. C.; Pereira, E. C. Simulation of Interfacial PH Changes during Hydrogen Evolution Reaction. *Journal of Electroanalytical Chemistry* **2016**, 765, 92–99.
<https://doi.org/10.1016/j.jelechem.2015.09.029>.

(168) Earl, E.; Calabrese Barton, S. Simulation of Intermediate Transport in Nanoscale Scaffolds for Multistep Catalytic Reactions. *Phys. Chem. Chem. Phys.* **2017**, 19 (23), 15463–15470. <https://doi.org/10.1039/C7CP00239D>.

- (169) Eun, C.; Keken-Huskey, P. M.; Metzger, V. T.; McCammon, J. A. A Model Study of Sequential Enzyme Reactions and Electrostatic Channeling. *The Journal of chemical physics* **2014**, *140* (10), 105101. <https://doi.org/10.1063/1.4867286>.
- (170) Chavan, K. S.; Calabrese Barton, S. Simulation of Intermediate Channeling by Nanoscale Confinement. *The Journal of Physical Chemistry C* **2018**. <https://doi.org/10.1021/acs.jpcc.8b01922>.
- (171) Cynthia G. Zoski*, † and; Michael V. Mirkin*, ‡. Steady-State Limiting Currents at Finite Conical Microelectrodes. **2002**. <https://doi.org/10.1021/AC015669I>.
- (172) Comstock, D. J.; Elam, J. W.; Pellin, M. J.; Hersam, M. C. Integrated Ultramicroelectrode-Nanopipet Probe for Concurrent Scanning Electrochemical Microscopy and Scanning Ion Conductance Microscopy. *Analytical Chemistry* **2010**, *82* (4), 1270–1276. <https://doi.org/10.1021/ac902224q>.
- (173) Wang, F. F.; Wang, W.; He, X.; Han, L.; Zhou, J. Z.; Tian, Z. Q.; Tian, Z. W.; Zhan, D. Nanofabrication of the Gold Scanning Probe for the STM-SECM Coupling System with Nanoscale Spatial Resolution. *Science China Chemistry* **2017**, *60* (5). <https://doi.org/10.1007/s11426-017-9029-9>.
- (174) Kai, T.; Zoski, C. G.; Bard, A. J. Scanning Electrochemical Microscopy at the Nanometer Level. *Chemical Communications* **2018**, *54* (16), 1934–1947. <https://doi.org/10.1039/C7CC09777H>.
- (175) Mirkin, M. V.; Fan, F.-R. F.; Bard, A. J. Scanning Electrochemical Microscopy Part 13. Evaluation of the Tip Shapes of Nanometer Size Microelectrodes. *Journal of Electroanalytical Chemistry* **1992**, *328* (1–2), 47–62. [https://doi.org/10.1016/0022-0728\(92\)80169-5](https://doi.org/10.1016/0022-0728(92)80169-5).
- (176) Cornut, R.; Lefrou, C. New Analytical Approximation of Feedback Approach Curves with a Microdisk SECM Tip and Irreversible Kinetic Reaction at the Substrate. *Journal of Electroanalytical Chemistry* **2008**, *621* (2), 178–184. <https://doi.org/10.1016/j.jelechem.2007.09.021>.
- (177) Zoski, C. G.; Mirkin, M. V. Steady-State Limiting Currents at Finite Conical Microelectrodes. *Analytical Chemistry* **2002**, *74* (9), 1986–1992. <https://doi.org/10.1021/ac015669i>.
- (178) Fernández, J. L.; Wijesinghe, M.; Zoski, C. G. Theory and Experiments for Voltammetric and SECM Investigations and Application to ORR Electrocatalysis at Nanoelectrode Ensembles of Ultramicroelectrode Dimensions. *Analytical Chemistry* **2015**, *87* (2), 1066–1074. <https://doi.org/10.1021/ac5039187>.
- (179) Yamada, Y.; Tsung, C.-K.; Huang, W.; Huo, Z.; Habas, S. E.; Soejima, T.; Aliaga, C. E.; Somorjai, G. A.; Yang, P. Nanocrystal Bilayer for Tandem Catalysis. *Nature Chem* **2011**, *3* (5), 372–376. <https://doi.org/10.1038/nchem.1018>.

- (180) Yang, M.; Qi, H.; Liu, F.; Ren, Y.; Pan, X.; Zhang, L.; Liu, X.; Wang, H.; Pang, J.; Zheng, M.; Wang, A.; Zhang, T. One-Pot Production of Cellulosic Ethanol via Tandem Catalysis over a Multifunctional Mo/Pt/WO_x Catalyst. *Joule* **2019**, 3 (8), 1937–1948. <https://doi.org/10.1016/j.joule.2019.05.020>.
- (181) Wilner, O. I.; Weizmann, Y.; Gill, R.; Lioubashevski, O.; Freeman, R.; Willner, I. Enzyme Cascades Activated on Topologically Programmed DNA Scaffolds. *Nature nanotechnology* **2009**, 4 (4), 249–254. <https://doi.org/10.1038/nnano.2009.50>.
- (182) Wilner, O. I.; Shimron, S.; Weizmann, Y.; Wang, Z.-G.; Willner, I. Self-Assembly of Enzymes on DNA Scaffolds: En Route to Biocatalytic Cascades and the Synthesis of Metallic Nanowires. *Nano Lett.* **2009**, 9 (5), 2040–2043. <https://doi.org/10.1021/nl900302z>.
- (183) Niemeyer, C. M. Semisynthetic DNA–Protein Conjugates for Biosensing and Nanofabrication. *Angewandte Chemie International Edition* **2010**, 49 (7), 1200–1216. <https://doi.org/10.1002/anie.200904930>.
- (184) Niemeyer, C. M.; Koehler, J.; Wuerdemann, C. DNA-Directed Assembly of Bienzymic Complexes from In Vivo Biotinylated NAD(P)H:FMN Oxidoreductase and Luciferase. *ChemBioChem* **2002**, 3 (2–3), 242–245. [https://doi.org/10.1002/1439-7633\(20020301\)3:2/3<242::AID-CBIC242>3.0.CO;2-F](https://doi.org/10.1002/1439-7633(20020301)3:2/3<242::AID-CBIC242>3.0.CO;2-F).
- (185) Müller, J.; Niemeyer, C. M. DNA-Directed Assembly of Artificial Multienzyme Complexes. *Biochemical and Biophysical Research Communications* **2008**, 377 (1), 62–67. <https://doi.org/10.1016/j.bbrc.2008.09.078>.
- (186) Broadwater, S. J.; Roth, S. L.; Price, K. E.; Kobašlija, M.; McQuade, D. T. One-Pot Multi-Step Synthesis: A Challenge Spawning Innovation. *Org. Biomol. Chem.* **2005**, 3 (16), 2899–2906. <https://doi.org/10.1039/B506621M>.
- (187) Lee, J. M.; Na, Y.; Han, H.; Chang, S. Cooperative Multi-Catalyst Systems for One-Pot Organic Transformations. *Chem. Soc. Rev.* **2004**, 33 (5), 302–312. <https://doi.org/10.1039/B309033G>.
- (188) Climent, M. J.; Corma, A.; Iborra, S.; Sabater, M. J. Heterogeneous Catalysis for Tandem Reactions. *ACS Catal.* **2014**, 4 (3), 870–891. <https://doi.org/10.1021/cs401052k>.
- (189) Lohr, T. L.; Marks, T. J. Orthogonal Tandem Catalysis. *Nature Chem* **2015**, 7 (6), 477–482. <https://doi.org/10.1038/nchem.2262>.
- (190) Oroz-Guinea, I.; García-Junceda, E. Enzyme Catalysed Tandem Reactions. *Current Opinion in Chemical Biology* **2013**, 17 (2), 236–249. <https://doi.org/10.1016/j.cbpa.2013.02.015>.
- (191) Robert, C.; M. Thomas, C. Tandem Catalysis: A New Approach to Polymers. *Chemical Society Reviews* **2013**, 42 (24), 9392–9402. <https://doi.org/10.1039/C3CS60287G>.
- (192) Wasilke, J.-C.; Obrey, S. J.; Baker, R. T.; Bazan, G. C. Concurrent Tandem Catalysis. *Chem. Rev.* **2005**, 105 (3), 1001–1020. <https://doi.org/10.1021/cr020018n>.

- (193) McInnis, J. P.; Delferro, M.; Marks, T. J. Multinuclear Group 4 Catalysis: Olefin Polymerization Pathways Modified by Strong Metal–Metal Cooperative Effects. *Acc. Chem. Res.* **2014**, *47* (8), 2545–2557. <https://doi.org/10.1021/ar5001633>.
- (194) A. Mata, J.; Ekkehardt Hahn, F.; Peris, E. Heterometallic Complexes, Tandem Catalysis and Catalytic Cooperativity. *Chemical Science* **2014**, *5* (5), 1723–1732. <https://doi.org/10.1039/C3SC53126K>.
- (195) Al-Amin, M.; Roth, K. E.; Blum, S. A. Mechanistic Studies of Gold and Palladium Cooperative Dual-Catalytic Cross-Coupling Systems. *ACS Catal.* **2014**, *4* (2), 622–629. <https://doi.org/10.1021/cs400641k>.
- (196) Smidt, J.; Hafner, W.; Jira, R.; Sieber, R.; Sedlmeier, J.; Sabel, A. The Oxidation of Olefins with Palladium Chloride Catalysts. *Angewandte Chemie International Edition in English* **1962**, *1* (2), 80–88. <https://doi.org/10.1002/anie.196200801>.
- (197) Liu, Y.; Hickey, D. P.; Guo, J. Y.; Earl, E.; Abdellaoui, S.; Milton, R. D.; Sigman, M. S.; Minter, S. D.; Calabrese Barton, S. Substrate Channeling in an Artificial Metabolon: A Molecular Dynamics Blueprint for an Experimental Peptide Bridge. *ACS Catalysis* **2017**, *7* (4), 2486–2493. <https://doi.org/10.1021/acscatal.6b03440>.
- (198) Spivey, H. O.; Ovádi, J. Substrate Channeling. *Methods: A Companion to Methods in Enzymology*. Academic Press October 1, 1999, pp 306–321. <https://doi.org/10.1006/meth.1999.0858>.
- (199) Milani, M.; Pesce, A.; Bolognesi, M.; Bocedi, A.; Ascenzi, P. Substrate Channeling: Molecular Bases. *Biochemistry and Molecular Biology Education* **2003**, *31* (4), 228–233. <https://doi.org/10.1002/bmb.2003.494031040239>.
- (200) Elcock, A. H.; Huber, G. A.; Andrew McCammon, J. Electrostatic Channeling of Substrates between Enzyme Active Sites: Comparison of Simulation and Experiment. *Biochemistry* **1997**, *36* (51), 16049–16058. <https://doi.org/10.1021/bi971709u>.
- (201) Elcock, a H.; Potter, M. J.; Matthews, D. a; Knighton, D. R.; McCammon, J. a. Electrostatic Channeling in the Bifunctional Enzyme Dihydrofolate Reductase-Thymidylate Synthase. *Journal of molecular biology* **1996**, *262* (3), 370–374. <https://doi.org/10.1006/jmbi.1996.0520>.
- (202) Bulutoglu, B.; Garcia, K. E.; Wu, F.; Minter, S. D.; Banta, S. Direct Evidence for Metabolon Formation and Substrate Channeling in Recombinant TCA Cycle Enzymes. *ACS Chemical Biology* **2016**, *11* (10), 2847–2853. <https://doi.org/10.1021/acscembio.6b00523>.
- (203) Xie, Y.; Calabrese Barton, S. Infrequent Metadynamics Study of Rare-Event Electrostatic Channeling. *Phys. Chem. Chem. Phys.* **2021**, *23* (23), 13381–13388. <https://doi.org/10/gkgmtf>.
- (204) Liu, Y.; Hickey, D. P.; Minter, S. D.; Dickson, A.; Calabrese Barton, S. Markov-State Transition Path Analysis of Electrostatic Channeling. *J. Phys. Chem. C* **2019**, *123* (24), 15284–15292. <https://doi.org/10/ghfprh>.

- (205) Knighton, D. R.; Kan, C.-C.; Howland, E.; Janson, C. A.; Hostomska, Z.; Welsh, K. M.; Matthews, D. A. Structure of and Kinetic Channelling in Bifunctional Dihydrofolate Reductase–Thymidylate Synthase. *Nat Struct Mol Biol* **1994**, *1* (3), 186–194. <https://doi.org/10.1038/nsb0394-186>.
- (206) Hyde, C. C.; Ahmed, S. A.; Padlan, E. A.; Miles, E. W.; Davies, D. R. Three-Dimensional Structure of the Tryptophan Synthase Alpha 2 Beta 2 Multienzyme Complex from *Salmonella Typhimurium*. *Journal of Biological Chemistry* **1988**, *263* (33), 17857–17871. [https://doi.org/10.1016/S0021-9258\(19\)77913-7](https://doi.org/10.1016/S0021-9258(19)77913-7).
- (207) Wang, J.; Nemeria, N. S.; Chandrasekhar, K.; Kumaran, S.; Arjunan, P.; Reynolds, S.; Calero, G.; Brukh, R.; Kakalis, L.; Furey, W.; Jordan, F. Structure and Function of the Catalytic Domain of the Dihydrolipoyl Acetyltransferase Component in *Escherichia Coli* Pyruvate Dehydrogenase Complex *. *Journal of Biological Chemistry* **2014**, *289* (22), 15215–15230. <https://doi.org/10.1074/jbc.M113.544080>.
- (208) Binda, C.; Bossi, R. T.; Wakatsuki, S.; Arzt, S.; Coda, A.; Curti, B.; Vanoni, M. A.; Mattevi, A. Cross-Talk and Ammonia Channeling between Active Centers in the Unexpected Domain Arrangement of Glutamate Synthase. *Structure* **2000**, *8* (12), 1299–1308. [https://doi.org/10.1016/S0969-2126\(00\)00540-2](https://doi.org/10.1016/S0969-2126(00)00540-2).
- (209) Cheng, Y.; Chang, C. A.; Yu, Z.; Zhang, Y.; Sun, M.; Leyh, T. S.; Holst, M. J.; Andrew McCammon, J. Diffusional Channeling in the Sulfate-Activating Complex: Combined Continuum Modeling and Coarse-Grained Brownian Dynamics Studies. *Biophysical Journal* **2008**, *95* (10), 4659–4667. <https://doi.org/10.1529/biophysj.108.140038>.
- (210) Johnson, J. L.; West, J. K.; Nelson, A. D. L.; Reinhart, G. D. Resolving the Fluorescence Response of *Escherichia Coli* Carbamoyl Phosphate Synthetase: Mapping Intra- and Intersubunit Conformational Changes. *Biochemistry* **2007**, *46* (2), 387–397. <https://doi.org/10.1021/bi061642n>.
- (211) Krahn, J. M.; Kim, J. H.; Burns, M. R.; Parry, R. J.; Zalkin, H.; Smith, J. L. Coupled Formation of an Amidotransferase Interdomain Ammonia Channel and a Phosphoribosyltransferase Active Site,. *Biochemistry* **1997**, *36* (37), 11061–11068. <https://doi.org/10.1021/bi9714114>.
- (212) Larsen, T. M.; Boehlein, S. K.; Schuster, S. M.; Richards, N. G. J.; Thoden, J. B.; Holden, H. M.; Rayment, I. Three-Dimensional Structure of *Escherichia Coli* Asparagine Synthetase B: A Short Journey from Substrate to Product,. *Biochemistry* **1999**, *38* (49), 16146–16157. <https://doi.org/10.1021/bi9915768>.
- (213) Raushel, F. M.; Thoden, J. B.; Reinhart, G. D.; Holden, H. M. Carbamoyl Phosphate Synthetase: A Crooked Path from Substrates to Products. *Current Opinion in Chemical Biology* **1998**, *2* (5), 624–632. [https://doi.org/10.1016/S1367-5931\(98\)80094-X](https://doi.org/10.1016/S1367-5931(98)80094-X).
- (214) Raushel, F. M.; Thoden, J. B.; Holden, H. M. Enzymes with Molecular Tunnels. *Acc. Chem. Res.* **2003**, *36* (7), 539–548. <https://doi.org/10.1021/ar020047k>.

- (215) Teplyakov, A.; Obmolova, G.; Badet, B.; Badet-Denisot, M.-A. Channeling of Ammonia in Glucosamine-6-Phosphate Synthase¹ Edited by R. Huber. *Journal of Molecular Biology* **2001**, *313* (5), 1093–1102. <https://doi.org/10.1006/jmbi.2001.5094>.
- (216) Creighton, T. E. A Steady-State Kinetic Investigation of the Reaction Mechanism of the Tryptophan Synthetase of Escherichia Coli. *European Journal of Biochemistry* **1970**, *13* (1), 1–10. <https://doi.org/10.1111/j.1432-1033.1970.tb00892.x>.
- (217) Demoss, J. A. Studies on the Mechanism of the Tryptophan Synthetase Reaction. *Biochimica et Biophysica Acta* **1962**, *62* (2), 279–293. [https://doi.org/10.1016/0006-3002\(62\)90041-0](https://doi.org/10.1016/0006-3002(62)90041-0).
- (218) Matchett, W. H. Indole Channeling by Tryptophan Synthase of Neurospora. *Journal of Biological Chemistry* **1974**, *249* (13), 4041–4049. [https://doi.org/10.1016/S0021-9258\(19\)42481-2](https://doi.org/10.1016/S0021-9258(19)42481-2).
- (219) Meek, T. D.; Garvey, E. P.; Santi, D. V. Purification and Characterization of the Bifunctional Thymidylate Synthetase-Dihydrofolate Reductase from Methotrexate-Resistant Leishmania Tropica. *Biochemistry* **1985**, *24* (3), 678–686. <https://doi.org/10.1021/bi00324a021>.
- (220) Stroud, R. M. An Electrostatic Highway. *Nat Struct Mol Biol* **1994**, *1* (3), 131–134. <https://doi.org/10.1038/nsb0394-131>.
- (221) Yanofsky, C.; Rachmeler, M. The Exclusion of Free Indole as an Intermediate in the Biosynthesis of Tryptophan in Neurospora Crassa. *Biochimica et Biophysica Acta* **1958**, *28*, 640–641. [https://doi.org/10.1016/0006-3002\(58\)90533-X](https://doi.org/10.1016/0006-3002(58)90533-X).
- (222) Leibundgut, M.; Maier, T.; Jenni, S.; Ban, N. The Multienzyme Architecture of Eukaryotic Fatty Acid Synthases. *Current Opinion in Structural Biology* **2008**, *18* (6), 714–725. <https://doi.org/10.1016/j.sbi.2008.09.008>.
- (223) Richard Perham. Swinging Arms and Swinging Domains in Multifunctional Enzymes: Catalytic Machines for Multistep Reactions | Annual Review of Biochemistry. *Annual review of biochemistry* **2020**, *69*, 961–1004. <https://doi-org.proxy1.cl.msu.edu/10.1146/annurev.biochem.69.1.961>.
- (224) Smolle, M.; Lindsay, J. G. Molecular Architecture of the Pyruvate Dehydrogenase Complex: Bridging the Gap. *Biochemical Society Transactions* **2006**, *34* (5), 815–818. <https://doi.org/10.1042/BST0340815>.
- (225) Smolle, M.; Prior, A. E.; Brown, A. E.; Cooper, A.; Byron, O.; Lindsay, J. G. A New Level of Architectural Complexity in the Human Pyruvate Dehydrogenase Complex *. *Journal of Biological Chemistry* **2006**, *281* (28), 19772–19780. <https://doi.org/10.1074/jbc.M601140200>.
- (226) Zhou, Z. H.; McCarthy, D. B.; O'Connor, C. M.; Reed, L. J.; Stoops, J. K. The Remarkable Structural and Functional Organization of the Eukaryotic Pyruvate Dehydrogenase Complexes. *PNAS* **2001**, *98* (26), 14802–14807. <https://doi.org/10.1073/pnas.011597698>.

- (227) Salles, A. G.; Zarra, S.; Turner, R. M.; Nitschke, J. R. A Self-Organizing Chemical Assembly Line. *J. Am. Chem. Soc.* **2013**, *135* (51), 19143–19146. <https://doi.org/10.1021/ja412235e>.
- (228) Vriezema, D. M.; Garcia, P. M. L.; Sancho Oltra, N.; Hatzakis, N. S.; Kuiper, S. M.; Nolte, R. J. M.; Rowan, A. E.; van Hest, J. C. M. Positional Assembly of Enzymes in Polymersome Nanoreactors for Cascade Reactions. *Angewandte Chemie* **2007**, *119* (39), 7522–7526. <https://doi.org/10.1002/ange.200701125>.
- (229) Wörsdörfer, B.; Woycechowsky, K. J.; Hilvert, D. Directed Evolution of a Protein Container. *Science* **2011**, *331* (6017), 589–592. <https://doi.org/10.1126/science.1199081>.
- (230) Zhao, M.; Deng, K.; He, L.; Liu, Y.; Li, G.; Zhao, H.; Tang, Z. Core–Shell Palladium Nanoparticle@Metal–Organic Frameworks as Multifunctional Catalysts for Cascade Reactions. *J. Am. Chem. Soc.* **2014**, *136* (5), 1738–1741. <https://doi.org/10.1021/ja411468e>.
- (231) Jørgensen, K.; Rasmussen, A. V.; Morant, M.; Nielsen, A. H.; Bjarnholt, N.; Zagrobelny, M.; Bak, S.; Møller, B. L. Metabolon Formation and Metabolic Channeling in the Biosynthesis of Plant Natural Products. *Current Opinion in Plant Biology* **2005**, *8* (3), 280–291. <https://doi.org/10.1016/j.pbi.2005.03.014>.
- (232) Sweetlove, L. J.; Fernie, A. R. The Spatial Organization of Metabolism within the Plant Cell. *Annu Rev Plant Biol* **2013**, *64*, 723–746. <https://doi.org/10.1146/annurev-arplant-050312-120233>.
- (233) Winkel, B. S. J. Metabolic Channeling in Plants. *Annu Rev Plant Biol* **2004**, *55*, 85–107. <https://doi.org/10.1146/annurev.arplant.55.031903.141714>.
- (234) Winkel-Shirley, B. Evidence for Enzyme Complexes in the Phenylpropanoid and Flavonoid Pathways. *Physiologia Plantarum* **1999**, *107* (1), 142–149. <https://doi.org/10.1034/j.1399-3054.1999.100119.x>.
- (235) Earl, E.; Calabrese Barton, S. Simulation of Intermediate Transport in Nanoscale Scaffolds for Multistep Catalytic Reactions. *Phys. Chem. Chem. Phys.* **2017**, *19* (23), 15463–15470. <https://doi.org/10.1039/C7CP00239D>.
- (236) Idan, O.; Hess, H. Origins of Activity Enhancement in Enzyme Cascades on Scaffolds. *ACS Nano* **2013**, *7* (10), 8658–8665. <https://doi.org/10.1021/nn402823k>.
- (237) Bauler, P.; Huber, G.; Leyh, T.; McCammon, J. A. Channeling by Proximity: The Catalytic Advantages of Active Site Colocalization Using Brownian Dynamics. *Journal of Physical Chemistry Letters* **2010**, *1* (9), 1332–1335. <https://doi.org/10.1021/jz1002007>.
- (238) Primary Mauna Loa CO₂ Record | Scripps CO₂ Program https://scrippsco2.ucsd.edu/data/atmospheric_co2/primary_mlo_co2_record.html (accessed 2021 -10 -31).

- (239) Zhang, X.; Guo, S.-X.; Gandionco, K. A.; Bond, A. M.; Zhang, J. Electrocatalytic Carbon Dioxide Reduction: From Fundamental Principles to Catalyst Design. *Materials Today Advances* **2020**, 7, 100074. <https://doi.org/10.1016/j.mtadv.2020.100074>.
- (240) Bushuyev, O. S.; De Luna, P.; Dinh, C. T.; Tao, L.; Saur, G.; van de Lagemaat, J.; Kelley, S. O.; Sargent, E. H. What Should We Make with CO₂ and How Can We Make It? *Joule* **2018**, 2 (5), 825–832. <https://doi.org/10.1016/j.joule.2017.09.003>.
- (241) Kortlever, R.; Shen, J.; Schouten, K. J. P.; Calle-Vallejo, F.; Koper, M. T. M. Catalysts and Reaction Pathways for the Electrochemical Reduction of Carbon Dioxide. *J. Phys. Chem. Lett.* **2015**, 6 (20), 4073–4082. <https://doi.org/10.1021/acs.jpclett.5b01559>.
- (242) Bloom, A.; Townsend, A.; Palchak, D.; Novacheck, J.; King, J.; Barrows, C.; Ibanez, E.; O’Connell, M.; Jordan, G.; Roberts, B.; Draxl, C.; Gruchalla, K.; RePPAE LLC, Wexford, PA (United States); GE Energy, Denver, CO (United States). *Eastern Renewable Generation Integration Study*; NREL/TP--6A20-64472, 1318192; 2016; p NREL/TP--6A20-64472, 1318192. <https://doi.org/10.2172/1318192>.
- (243) GE Energy; National Renewable Energy Laboratory (NREL), Golden, CO. *Western Wind and Solar Integration Study*; NREL/SR-550-47434, 981991; 2010; p NREL/SR-550-47434, 981991. <https://doi.org/10.2172/981991>.
- (244) Denholm, P.; Clark, K.; O’Connell, M. On the Path to SunShot: Emerging Issues and Challenges in Integrating High Levels of Solar into the Electrical Generation and Transmission System. 68.
- (245) Hori, Y.; Wakebe, H.; Tsukamoto, T.; Koga, O. Electrocatalytic Process of CO Selectivity in Electrochemical Reduction of CO₂ at Metal Electrodes in Aqueous Media. *Electrochimica Acta* **1994**, 39 (11), 1833–1839. [https://doi.org/10.1016/0013-4686\(94\)85172-7](https://doi.org/10.1016/0013-4686(94)85172-7).
- (246) Bhargava, S. S.; Proietto, F.; Azmoodeh, D.; Cofell, E. R.; Henckel, D. A.; Verma, S.; Brooks, C. J.; Gewirth, A. A.; Kenis, P. J. A. System Design Rules for Intensifying the Electrochemical Reduction of CO₂ to CO on Ag Nanoparticles. *ChemElectroChem* **2020**, 7 (9), 2001–2011. <https://doi.org/10.1002/celec.202000089>.
- (247) Murata, A.; Hori, Y. Product Selectivity Affected by Cationic Species in Electrochemical Reduction of CO₂ and CO at a Cu Electrode. *BCSJ* **1991**, 64 (1), 123–127. <https://doi.org/10.1246/bcsj.64.123>.
- (248) Schizodimou, A.; Kyriacou, G. Acceleration of the Reduction of Carbon Dioxide in the Presence of Multivalent Cations. *Electrochimica Acta* **2012**, 78, 171–176. <https://doi.org/10.1016/j.electacta.2012.05.118>.
- (249) Chaplin, R. P. S.; Wragg, A. A. Effects of Process Conditions and Electrode Material on Reaction Pathways for Carbon Dioxide Electroreduction with Particular Reference to Formate Formation. *Journal of Applied Electrochemistry* **2003**, 33 (12), 1107–1123. <https://doi.org/10.1023/B:JACH.0000004018.57792.b8>.

- (250) Zhang, B. A.; Ozel, T.; Elias, J. S.; Costentin, C.; Nocera, D. G. Interplay of Homogeneous Reactions, Mass Transport, and Kinetics in Determining Selectivity of the Reduction of CO₂ on Gold Electrodes. *ACS Cent. Sci.* **2019**, *5* (6), 1097–1105. <https://doi.org/10/ggbvcs>.
- (251) Kuhl, K. P.; Hatsukade, T.; Cave, E. R.; Abram, D. N.; Kibsgaard, J.; Jaramillo, T. F. Electrocatalytic Conversion of Carbon Dioxide to Methane and Methanol on Transition Metal Surfaces. *J. Am. Chem. Soc.* **2014**, *136* (40), 14107–14113. <https://doi.org/10/gh66gw>.
- (252) Hatsukade, T.; Kuhl, K. P.; Cave, E. R.; Abram, D. N.; Jaramillo, T. F. Insights into the Electrocatalytic Reduction of CO₂ on Metallic Silver Surfaces. *Phys. Chem. Chem. Phys.* **2014**, *16* (27), 13814–13819. <https://doi.org/10.1039/C4CP00692E>.
- (253) Ayers, W. M. An Overview of Electrochemical Carbon Dioxide Reduction. In *Carbon Dioxide Chemistry*; Paul, J., Pradier, C.-M., Eds.; Woodhead Publishing, 1994; pp 365–374. <https://doi.org/10.1016/B978-1-85573-799-0.50045-5>.
- (254) Lee, J.; Tak, Y. Electrocatalytic Activity of Cu Electrode in Electroreduction of CO₂. *Electrochimica Acta* **2001**, *46* (19), 3015–3022. [https://doi.org/10.1016/S0013-4686\(01\)00527-8](https://doi.org/10.1016/S0013-4686(01)00527-8).
- (255) Summers, D. P.; Frese, K. W. The Electrochemical Reduction of Aqueous Carbon Monoxide and Methanol to Methane at Ruthenium Electrodes. *J. Electrochem. Soc.* **1988**, *135* (1), 264. <https://doi.org/10.1149/1.2095576>.
- (256) Vassiliev, Yu. B.; Bagotsky, V. S.; Osetrova, N. V.; Khazova, O. A.; Mayorova, N. A. Electroreduction of Carbon Dioxide: Part I. The Mechanism and Kinetics of Electroreduction of CO₂ in Aqueous Solutions on Metals with High and Moderate Hydrogen Overvoltages. *Journal of Electroanalytical Chemistry and Interfacial Electrochemistry* **1985**, *189* (2), 271–294. [https://doi.org/10.1016/0368-1874\(85\)80073-3](https://doi.org/10.1016/0368-1874(85)80073-3).
- (257) Udupa, K. S.; Subramanian, G. S.; Udupa, H. V. K. The Electrolytic Reduction of Carbon Dioxide to Formic Acid. *Electrochimica Acta* **1971**, *16* (9), 1593–1598. [https://doi.org/10.1016/0013-4686\(71\)80028-2](https://doi.org/10.1016/0013-4686(71)80028-2).
- (258) MIZUNO, T.; OHTA, K.; SASAKI, A.; AKAI, T.; HIRANO, M.; KAWABE, A. Effect of Temperature on Electrochemical Reduction of High-Pressure CO₂ with In, Sn, and Pb Electrodes. *Energy Sources* **1995**, *17* (5), 503–508. <https://doi.org/10.1080/00908319508946098>.
- (259) Delacourt, C.; Ridgway, P. L.; Kerr, J. B.; Newman, J. Design of an Electrochemical Cell Making Syngas (CO + H₂) from CO₂ and H₂O Reduction at Room Temperature. *J. Electrochem. Soc.* **2007**, *155* (1), B42. <https://doi.org/10.1149/1.2801871>.
- (260) Yang, K. D.; Lee, C. W.; Jang, J. H.; Ha, T. R.; Nam, K. T. Rise of Nano Effects in Electrode during Electrocatalytic CO₂ Conversion. *Nanotechnology* **2017**, *28* (35), 352001. <https://doi.org/10/gjtsnm>.

- (261) Gupta, N.; Gattrell, M.; MacDougall, B. Calculation for the Cathode Surface Concentrations in the Electrochemical Reduction of CO₂ in KHCO₃ Solutions. *J Appl Electrochem* **2006**, *36* (2), 161–172. <https://doi.org/10.1007/s10800-005-9058-y>.
- (262) Verma, S.; Hamasaki, Y.; Kim, C.; Huang, W.; Lu, S.; Jhong, H.-R. M.; Gewirth, A. A.; Fujigaya, T.; Nakashima, N.; Kenis, P. J. A. Insights into the Low Overpotential Electroreduction of CO₂ to CO on a Supported Gold Catalyst in an Alkaline Flow Electrolyzer. *ACS Energy Lett.* **2018**, *3* (1), 193–198. <https://doi.org/10.1021/acsenenergylett.7b01096>.
- (263) Li, C. W.; Kanan, M. W. CO₂ Reduction at Low Overpotential on Cu Electrodes Resulting from the Reduction of Thick Cu₂O Films. *J. Am. Chem. Soc.* **2012**, *134* (17), 7231–7234. <https://doi.org/10.1021/ja3010978>.
- (264) Varela, A. S.; Ju, W.; Reier, T.; Strasser, P. Tuning the Catalytic Activity and Selectivity of Cu for CO₂ Electroreduction in the Presence of Halides. *ACS Catal.* **2016**, *6* (4), 2136–2144. <https://doi.org/10.1021/acscatal.5b02550>.
- (265) Hori, Y.; Murata, A.; Takahashi, R. Formation of Hydrocarbons in the Electrochemical Reduction of Carbon Dioxide at a Copper Electrode in Aqueous Solution. *J. Chem. Soc., Faraday Trans. 1* **1989**, *85* (8), 2309–2326. <https://doi.org/10.1039/F19898502309>.
- (266) Hori, Y.; Takahashi, R.; Yoshinami, Y.; Murata, A. Electrochemical Reduction of CO at a Copper Electrode. *J. Phys. Chem. B* **1997**, *101* (36), 7075–7081. <https://doi.org/10.1021/jp970284i>.
- (267) Schouten, K. J. P.; Pérez Gallent, E.; Koper, M. T. M. The Influence of PH on the Reduction of CO and CO₂ to Hydrocarbons on Copper Electrodes. *Journal of Electroanalytical Chemistry* **2014**, *716*, 53–57. <https://doi.org/10.1016/j.jelechem.2013.08.033>.
- (268) White, J. L.; Baruch, M. F.; Pander, J. E.; Hu, Y.; Fortmeyer, I. C.; Park, J. E.; Zhang, T.; Liao, K.; Gu, J.; Yan, Y.; Shaw, T. W.; Abelev, E.; Bocarsly, A. B. Light-Driven Heterogeneous Reduction of Carbon Dioxide: Photocatalysts and Photoelectrodes. *Chem. Rev.* **2015**, *115* (23), 12888–12935. <https://doi.org/10.1021/acs.chemrev.5b00370>.
- (269) Feaster, J. T.; Shi, C.; Cave, E. R.; Hatsukade, T.; Abram, D. N.; Kuhl, K. P.; Hahn, C.; Nørskov, J. K.; Jaramillo, T. F. Understanding Selectivity for the Electrochemical Reduction of Carbon Dioxide to Formic Acid and Carbon Monoxide on Metal Electrodes. *ACS Catal.* **2017**, *7* (7), 4822–4827. <https://doi.org/10.1021/acscatal.7b00687>.
- (270) Chen, Y.; Kanan, M. W. Tin Oxide Dependence of the CO₂ Reduction Efficiency on Tin Electrodes and Enhanced Activity for Tin/Tin Oxide Thin-Film Catalysts. *J. Am. Chem. Soc.* **2012**, *134* (4), 1986–1989. <https://doi.org/10.1021/ja2108799>.
- (271) Chen, Y.; Li, C. W.; Kanan, M. W. Aqueous CO₂ Reduction at Very Low Overpotential on Oxide-Derived Au Nanoparticles. *J. Am. Chem. Soc.* **2012**, *134* (49), 19969–19972. <https://doi.org/10.1021/ja309317u>.

- (272) Kattel, S.; Liu, P.; Chen, J. G. Tuning Selectivity of CO₂ Hydrogenation Reactions at the Metal/Oxide Interface. *J. Am. Chem. Soc.* **2017**, *139* (29), 9739–9754. <https://doi.org/10.1021/jacs.7b05362>.
- (273) Daza, Y. A.; Kuhn, J. N. CO₂ Conversion by Reverse Water Gas Shift Catalysis: Comparison of Catalysts, Mechanisms and Their Consequences for CO₂ Conversion to Liquid Fuels. *RSC Adv.* **2016**, *6* (55), 49675–49691. <https://doi.org/10.1039/C6RA05414E>.
- (274) Asset, T.; Garcia, S. T.; Herrera, S.; Andersen, N.; Chen, Y.; Peterson, E. J.; Matanovic, I.; Artyushkova, K.; Lee, J.; Minter, S. D.; Dai, S.; Pan, X.; Chavan, K.; Calabrese Barton, S.; Atanassov, P. Investigating the Nature of the Active Sites for the CO₂ Reduction Reaction on Carbon-Based Electrocatalysts. *ACS Catal.* **2019**, *9* (9), 7668–7678. <https://doi.org/10.1021/acscatal.9b01513>.
- (275) Leonard, N.; Ju, W.; Sinev, I.; Steinberg, J.; Luo, F.; Varela, A. S.; Cuenya, B. R.; Strasser, P. The Chemical Identity, State and Structure of Catalytically Active Centers during the Electrochemical CO₂ Reduction on Porous Fe–Nitrogen–Carbon (Fe–N–C) Materials. *Chem. Sci.* **2018**, *9* (22), 5064–5073. <https://doi.org/10.1039/C8SC00491A>.
- (276) Takahashi, K.; Hiratsuka, K.; Sasaki, H.; Toshima, S. Electrocatalytic Behavior of Metal Porphyrins in the Reduction of Carbon Dioxide. *Chem. Lett.* **1979**, *8* (4), 305–308. <https://doi.org/10.1246/cl.1979.305>.
- (277) Hiratsuka, K.; Takahashi, K.; Sasaki, H.; Toshima, S. Electrocatalytic Behavior of Tetrasulfonated Metal Phthalocyanines in the Reduction of Carbon Dioxide. *Chem. Lett.* **1977**, *6* (10), 1137–1140. <https://doi.org/10.1246/cl.1977.1137>.
- (278) Hammouche, M.; Lexa, D.; Savéant, J. M.; Momenteau, M. Catalysis of the Electrochemical Reduction of Carbon Dioxide by Iron(“0”) Porphyrins. *Journal of Electroanalytical Chemistry and Interfacial Electrochemistry* **1988**, *249* (1), 347–351. [https://doi.org/10.1016/0022-0728\(88\)80372-3](https://doi.org/10.1016/0022-0728(88)80372-3).
- (279) Bhugun, I.; Lexa, D.; Savéant, J.-M. Catalysis of the Electrochemical Reduction of Carbon Dioxide by Iron(0) Porphyrins: Synergistic Effect of Weak Brönsted Acids. *J. Am. Chem. Soc.* **1996**, *118* (7), 1769–1776. <https://doi.org/10.1021/ja9534462>.
- (280) Lin, S.; Diercks, C. S.; Zhang, Y.-B.; Kornienko, N.; Nichols, E. M.; Zhao, Y.; Paris, A. R.; Kim, D.; Yang, P.; Yaghi, O. M.; Chang, C. J. Covalent Organic Frameworks Comprising Cobalt Porphyrins for Catalytic CO₂ Reduction in Water. *Science* **2015**, *349* (6253), 1208–1213. <https://doi.org/10.1126/science.aac8343>.
- (281) Leung, K.; Nielsen, I. M. B.; Sai, N.; Medforth, C.; Shelnutt, J. A. Cobalt–Porphyrin Catalyzed Electrochemical Reduction of Carbon Dioxide in Water. 2. Mechanism from First Principles. *J. Phys. Chem. A* **2010**, *114* (37), 10174–10184. <https://doi.org/10.1021/jp1012335>.
- (282) Varela, A. S.; Ranjbar Sahraie, N.; Steinberg, J.; Ju, W.; Oh, H.-S.; Strasser, P. Metal-Doped Nitrogenated Carbon as an Efficient Catalyst for Direct CO₂ Electroreduction to CO and

Hydrocarbons. *Angewandte Chemie International Edition* **2015**, *54* (37), 10758–10762. <https://doi.org/10.1002/anie.201502099>.

(283) Ju, W.; Bagger, A.; Hao, G.-P.; Varela, A. S.; Sinev, I.; Bon, V.; Roldan Cuenya, B.; Kaskel, S.; Rossmeisl, J.; Strasser, P. Understanding Activity and Selectivity of Metal-Nitrogen-Doped Carbon Catalysts for Electrochemical Reduction of CO₂. *Nat Commun* **2017**, *8* (1), 944. <https://doi.org/10.1038/s41467-017-01035-z>.

(284) Hori, Y.; Kikuchi, K.; Suzuki, S. Production of Co and CH₄ in Electrochemical Reduction of CO₂ at Metal Electrodes in Aqueous Hydrogencarbonate Solution. *Chem. Lett.* **1985**, *14* (11), 1695–1698. <https://doi.org/10.1246/cl.1985.1695>.

(285) Maier, C. U.; Bandi, A.; Specht, M. Influence of Polarization Time and Temperature on the Adsorption of Carbon Dioxide on Platinum. *J. Electrochem. Soc.* **1994**, *141* (1), L4. <https://doi.org/10.1149/1.2054719>.

(286) Kudo, A.; Nakagawa, S.; Tsuneta, A.; Sakata, T. Electrochemical Reduction of High Pressure CO₂ on Ni Electrodes.

(287) Kas, R.; Kortlever, R.; Milbrat, A.; M. Koper, M. T.; Mul, G.; Baltrusaitis, J. Electrochemical CO₂ Reduction on Cu₂O-Derived Copper Nanoparticles: Controlling the Catalytic Selectivity of Hydrocarbons. *Physical Chemistry Chemical Physics* **2014**, *16* (24), 12194–12201. <https://doi.org/10.1039/C4CP01520G>.

(288) Yang, K.; Kas, R.; Smith, W. A. In Situ Infrared Spectroscopy Reveals Persistent Alkalinity near Electrode Surfaces during CO₂ Electroreduction. *J. Am. Chem. Soc.* **2019**, *141* (40), 15891–15900. <https://doi.org/10.1021/jacs.9b07000>.

(289) Ayemoba, O.; Cuesta, A. Spectroscopic Evidence of Size-Dependent Buffering of Interfacial pH by Cation Hydrolysis during CO₂ Electroreduction. *ACS Appl. Mater. Interfaces* **2017**, *9* (33), 27377–27382. <https://doi.org/10.1021/acsami.7b07351>.

(290) Zhang, Z.; Melo, L.; Jansonius, R. P.; Habibzadeh, F.; Grant, E. R.; Berlinguette, C. P. pH Matters When Reducing CO₂ in an Electrochemical Flow Cell. *ACS Energy Lett.* **2020**, *5* (10), 3101–3107. <https://doi.org/10.1021/acsenenergylett.0c01606>.

(291) Monteiro, M. C. O.; Jacobse, L.; Koper, M. T. M. Understanding the Voltammetry of Bulk CO Electrooxidation in Neutral Media through Combined SECM Measurements. *The Journal of Physical Chemistry Letters* **2020**, *11* (22), 9708–9713. <https://doi.org/10.1021/acs.jpcllett.0c02779>.

(292) García, G. Correlation between CO Oxidation and H Adsorption/Desorption on Pt Surfaces in a Wide pH Range: The Role of Alkali Cations. *ChemElectroChem* **2017**, *4* (3), 459–462. <https://doi.org/10.1002/celec.201600731>.

(293) Gisbert, R.; García, G.; Koper, M. T. M. Oxidation of Carbon Monoxide on Poly-Oriented and Single-Crystalline Platinum Electrodes over a Wide Range of pH. *Electrochimica Acta* **2011**, *56* (5), 2443–2449. <https://doi.org/10.1016/j.electacta.2010.11.032>.

- (294) Billy, J. T.; Co, A. C. Experimental Parameters Influencing Hydrocarbon Selectivity during the Electrochemical Conversion of CO₂. *ACS Catal.* **2017**, 7 (12), 8467–8479. <https://doi.org/10.1021/acscatal.7b02373>.
- (295) Singh, M. R.; Kwon, Y.; Lum, Y.; Ager, J. W.; Bell, A. T. Hydrolysis of Electrolyte Cations Enhances the Electrochemical Reduction of CO₂ over Ag and Cu. *J. Am. Chem. Soc.* **2016**, 138 (39), 13006–13012. <https://doi.org/10.1021/jacs.6b07612>.
- (296) Ringe, S.; Clark, E. L.; Resasco, J.; Walton, A.; Seger, B.; Bell, A. T.; Chan, K. Understanding Cation Effects in Electrochemical CO₂ Reduction. *Energy & Environmental Science* **2019**, 12 (10), 3001–3014. <https://doi.org/10/c8t5>.
- (297) El-Giar, E. E.-D. M.; Wipf, D. O. Microparticle-Based Iridium Oxide Ultramicroelectrodes for PH Sensing and Imaging. *Journal of Electroanalytical Chemistry* **2007**, 609 (2), 147–154. <https://doi.org/10.1016/j.jelechem.2007.06.022>.
- (298) Mohan, S.; Vellakkat, M.; Aravind, A.; U, R. Hydrothermal Synthesis and Characterization of Zinc Oxide Nanoparticles of Various Shapes under Different Reaction Conditions. *Nano Express* **2020**, 1 (3), 030028. <https://doi.org/10.1088/2632-959X/abc813>.
- (299) Polcari, D.; Dauphin-Ducharme, P.; Mauzeroll, J. Scanning Electrochemical Microscopy: A Comprehensive Review of Experimental Parameters from 1989 to 2015. *Chemical Reviews* **2016**, 116 (22). <https://doi.org/10.1021/acs.chemrev.6b00067>.
- (300) Kettler, P. B. Platinum Group Metals in Catalysis: Fabrication of Catalysts and Catalyst Precursors. *Org. Process Res. Dev.* **2003**, 7 (3), 342–354. <https://doi.org/10.1021/op034017o>.
- (301) Jacobse, L.; J. Raaijman, S.; M. Koper, M. T. The Reactivity of Platinum Microelectrodes. *Physical Chemistry Chemical Physics* **2016**, 18 (41), 28451–28457. <https://doi.org/10.1039/C6CP05361K>.
- (302) Anson, F. C.; Lingane, J. J. Chemical Evidence for Oxide Films on Platinum Electrometric Electrodes. *J. Am. Chem. Soc.* **1957**, 79 (18), 4901–4904. <https://doi.org/10.1021/ja01575a019>.
- (303) Unwin, P. R.; Bard, A. J. Scanning Electrochemical Microscopy. 9. Theory and Application of the Feedback Mode to the Measurement of Following Chemical Reaction Rates in Electrode Processes. *Journal of Physical Chemistry* **1991**, 95 (20), 7814–7824. <https://doi.org/10.1021/j100173a049>.
- (304) Sun, P.; Mirkin, M. V. Kinetics of Electron-Transfer Reactions at Nanoelectrodes. *Analytical Chemistry* **2006**, 78 (18), 6526–6534. <https://doi.org/10.1021/ac060924q>.
- (305) Izquierdo, J.; Knittel, P.; Kranz, C. Scanning Electrochemical Microscopy: An Analytical Perspective. *Analytical and Bioanalytical Chemistry*. Springer Berlin Heidelberg January 6, 2018, pp 307–324. <https://doi.org/10.1007/s00216-017-0742-7>.

- (306) Monteiro, M. C. O.; Jacobse, L.; Touzalin, T.; Koper, M. T. M. Mediator-Free SECM for Probing the Diffusion Layer PH with Functionalized Gold Ultramicroelectrodes. *Analytical Chemistry* **2020**, 92 (2), 2237–2243. <https://doi.org/10/gg77vg>.
- (307) Lefrou, C.; Cornut, R. Analytical Expressions for Quantitative Scanning Electrochemical Microscopy (SECM). *ChemPhysChem* **2010**, 11 (3), 547–556. <https://doi.org/10.1002/cphc.200900600>.
- (308) Sun, P.; Laforge, F. O.; Mirkin, M. V. Scanning Electrochemical Microscopy in the 21st Century. **2007**, 9 (7), 802–823.
- (309) Sklyar, O.; Kueng, A.; Kranz, C.; Mizaikoff, B.; Lugstein, A.; Bertagnolli, E.; Wittstock, G. Numerical Simulation of Scanning Electrochemical Microscopy Experiments with Frame-Shaped Integrated Atomic Force Microscopy-SECM Probes Using the Boundary Element Method. *Analytical Chemistry* **2005**, 77 (3), 764–771. <https://doi.org/10.1021/ac048732n>.
- (310) Pust, S. E.; Salomo, M.; Oesterschulze, E.; Wittstock, G. Influence of Electrode Size and Geometry on Electrochemical Experiments with Combined SECM–SFM Probes. *Nanotechnology* **2010**, 21 (10), 105709. <https://doi.org/10.1088/0957-4484/21/10/105709>.
- (311) Eifert, A.; Mizaikoff, B.; Kranz, C. Advanced Fabrication Process for Combined Atomic Force-Scanning Electrochemical Microscopy (AFM-SECM) Probes. *Micron* **2015**, 68, 27–35. <https://doi.org/10.1016/j.micron.2014.08.008>.
- (312) Velmurugan, J.; Agrawal, A.; An, S.; Choudhary, E.; Szalai, V. A. Fabrication of Scanning Electrochemical Microscopy-Atomic Force Microscopy Probes to Image Surface Topography and Reactivity at the Nanoscale. *Analytical Chemistry* **2017**, 89 (5), 2687–2691. <https://doi.org/10.1021/acs.analchem.7b00210>.
- (313) Abbou, J.; Demaille, C.; Druet, M.; Moiroux, J. Fabrication of Submicrometer-Sized Gold Electrodes of Controlled Geometry for Scanning Electrochemical-Atomic Force Microscopy. *Analytical Chemistry* **2002**, 74 (24), 6355–6363. <https://doi.org/10.1021/ac020385z>.
- (314) Huang, Z.; Wolf, P. De; Poddar, R.; Li, C.; Mark, A.; Nellist, M. R.; Chen, Y.; Jiang, J.; Papastavrou, G.; Boettcher, S. W.; Xiang, C.; Brunschwig, B. S. PeakForce Scanning Electrochemical Microscopy with Nanoelectrode Probes. *Microsc. Today* **2016**, 24 (November), 18–25. <https://doi.org/10.1017/S1551929516000882>.
- (315) Leonhardt, K.; Avdic, A.; Lugstein, A.; Pobelov, I.; Wandlowski, T.; Wu, M.; Gollas, B.; Denuault, G. Atomic Force Microscopy-Scanning Electrochemical Microscopy: Influence of Tip Geometry and Insulation Defects on Diffusion Controlled Currents at Conical Electrodes. *Analytical Chemistry* **2011**, 83 (8), 2971–2977. <https://doi.org/10.1021/ac103083y>.
- (316) Leonhardt, K.; Avdic, A.; Lugstein, A.; Pobelov, I.; Wandlowski, T.; Gollas, B.; Denuault, G. Scanning Electrochemical Microscopy: Diffusion Controlled Approach Curves for Conical AFM-SECM Tips. *Electrochemistry Communications* **2013**, 27, 29–33. <https://doi.org/10.1016/j.elecom.2012.10.034>.

- (317) O'Connell, M. A.; Wain, A. J. Combined Electrochemical-Topographical Imaging: A Critical Review. *Analytical Methods* **2015**, *7* (17), 6983–6999. <https://doi.org/10.1039/C5AY00557D>.
- (318) Bard, A. J.; Denuault, Guy.; Friesner, R. A.; Dornblaser, B. C.; Tuckerman, L. S. Scanning Electrochemical Microscopy: Theory and Application of the Transient (Chronoamperometric) SECM Response. *Analytical chemistry* **1991**, *63* (13), 1282–1288. <https://doi.org/10.1021/ac00013a019>.
- (319) Arca, M.; Bard, A. J.; Horrocks, B. R.; Richards, T. C.; Treichel, D. A. Advances in Scanning Electrochemical Microscopy. Plenary Lecture. *The Analyst* **1994**, *119* (5), 719. <https://doi.org/10.1039/an9941900719>.
- (320) Burt, D. P.; Wilson, N. R.; Janus, U.; Macpherson, J. V; Unwin, P. R. In-Situ Atomic Force Microscopy (AFM) Imaging: Influence of AFM Probe Geometry on Diffusion to Microscopic Surfaces. *Langmuir* **2008**, *24* (22), 12867–12876. <https://doi.org/10.1021/la8003323>.
- (321) Shi, X.; Qing, W.; Marhaba, T.; Zhang, W. Atomic Force Microscopy - Scanning Electrochemical Microscopy (AFM-SECM) for Nanoscale Topographical and Electrochemical Characterization: Principles, Applications and Perspectives. *Electrochimica Acta* **2020**, *332*, 135472. <https://doi.org/10.1016/j.electacta.2019.135472>.
- (322) Nogala, W.; Velmurugan, J.; Mirkin, M. V. Atomic Force Microscopy of Electrochemical Nanoelectrodes. *Analytical Chemistry* **2012**, *84* (12), 5192–5197. <https://doi.org/10.1021/ac300744t>.
- (323) Voigtländer, B. Static Atomic Force Microscopy. *NanoScience and Technology* **2015**, *69*, 177–186. https://doi.org/10.1007/978-3-662-45240-0_13.
- (324) Mahotas: Open source software for scriptable computer vision <https://openresearchsoftware.metajnl.com/articles/10.5334/jors.ac/> (accessed 2021 -08 -05).
- (325) Amphlett, J. L.; Denuault, G. Scanning Electrochemical Microscopy (SECM): An Investigation of the Effects of Tip Geometry on Amperometric Tip Response. *The Journal of Physical Chemistry B* **1998**, *102* (49), 9946–9951. <https://doi.org/10.1021/jp982829u>.
- (326) Mirabal, A.; Calabrese Barton, S. SECM-FEM <https://github.com/scbgroup/SECM-FEM>.
- (327) Liu, B.; Bard, A. J. Scanning Electrochemical Microscopy. 45. Study of the Kinetics of Oxygen Reduction on Platinum with Potential Programming of the Tip. *Journal of Physical Chemistry B* **2002**, *106* (49), 12801–12806. <https://doi.org/10.1021/jp026824f>.
- (328) Wang, J.; Swain, G. M. Fabrication and Evaluation of Platinum/Diamond Composite Electrodes for Electrocatalysis. *Journal of The Electrochemical Society* **2003**, *150* (1), E24. <https://doi.org/10.1149/1.1524612>.

- (329) Beucher, S.; Meyer, F. The Morphological Approach to Segmentation: The Watershed Transformation. *Mathematical Morphology in Image Processing* **1993**, 433–481. <https://doi.org/Export> Date 6 May 2013.
- (330) Nioradze, N.; Chen, R.; Kurapati, N.; Khvataeva-Domanov, A.; Mabic, S.; Amemiya, S. Organic Contamination of Highly Oriented Pyrolytic Graphite As Studied by Scanning Electrochemical Microscopy. *Anal. Chem.* **2015**, 87 (9), 4836–4843. <https://doi.org/10.1021/acs.analchem.5b00213>.
- (331) Nellist, M. R.; Laskowski, F. A. L.; Qiu, J.; Hajibabaei, H.; Sivula, K.; Hamann, T. W.; Boettcher, S. W. Potential-Sensing Electrochemical Atomic Force Microscopy for in Operando Analysis of Water-Splitting Catalysts and Interfaces. *Nature Energy* **2018**, 3 (1), 46–52. <https://doi.org/10.1038/s41560-017-0048-1>.
- (332) Goyal, A.; Marcandalli, G.; Mints, V. A.; Koper, M. T. M. Competition between CO₂ Reduction and Hydrogen Evolution on a Gold Electrode under Well-Defined Mass Transport Conditions. *J Am Chem Soc* **2020**, 142 (9), 4154–4161. <https://doi.org/10/gg84dq>.
- (333) Wuttig, A.; Yoon, Y.; Ryu, J.; Surendranath, Y. Bicarbonate Is Not a General Acid in Au-Catalyzed CO₂ Electroreduction. *Journal of the American Chemical Society* **2017**, 139 (47), 17109–17113. <https://doi.org/10.1021/jacs.7b08345>.
- (334) Keene, R. F.; Sullivan, B. P.; Krist, K.; Guard, H. E. *Electrochemical and Electrocatalytic Reactions of Carbon Dioxide - 1st Edition*; Elsevier, 1993.
- (335) Singh, M. R.; Goodpaster, J. D.; Weber, A. Z.; Head-Gordon, M.; Bell, A. T. Mechanistic Insights into Electrochemical Reduction of CO₂ over Ag Using Density Functional Theory and Transport Models. *Proceedings of the National Academy of Sciences* **2017**, 114 (42), E8812--E8821. <https://doi.org/10/gcgx3h>.
- (336) Bohra, D.; Chaudhry, J. H.; Burdyny, T.; Pidko, E. A.; Smith, W. A. Modeling the Electrical Double Layer to Understand the Reaction Environment in a CO₂ Electrocatalytic System. *Energy & Environmental Science* **2019**, 12 (11), 3380–3389. <https://doi.org/10.1039/C9EE02485A>.
- (337) Adamczyk, K.; Prémont-Schwarz, M.; Pines, D.; Pines, E.; Nibbering, E. T. J. Real-Time Observation of Carbonic Acid Formation in Aqueous Solution. *Science* **2009**, 326 (5960), 1690–1694. <https://doi.org/10.1126/science.1180060>.
- (338) Monteiro, M. C. O.; Jacobse, L.; Touzalin, T.; Koper, M. T. M. Mediator-Free SECM for Probing the Diffusion Layer PH with Functionalized Gold Ultramicroelectrodes. *Analytical Chemistry* **2020**, 92 (2), 2237–2243. <https://doi.org/10.1021/acs.analchem.9b04952>.
- (339) Shinagawa, T.; Garcia-Esparza, A. T.; Takanabe, K. Insight on Tafel Slopes from a Microkinetic Analysis of Aqueous Electrocatalysis for Energy Conversion. *Scientific Reports* **2015**, 5 (1), 13801. <https://doi.org/10.1038/srep13801>.

- (340) Carneiro-Neto, E. B.; Lopes, M. C.; Pereira, E. C. Simulation of Interfacial PH Changes during Hydrogen Evolution Reaction. *Journal of Electroanalytical Chemistry* **2016**, 765, 92–99. <https://doi.org/10.1016/j.jelechem.2015.09.029>.
- (341) Monteiro, M. C. O.; Mirabal, A.; Jacobse, L.; Doblhoff-Dier, K.; Barton, S. C.; Koper, M. T. M. Time-Resolved Local PH Measurements during CO₂ Reduction Using Scanning Electrochemical Microscopy: Buffering and Tip Effects. *JACS Au* **2021**. <https://doi.org/10.1021/jacsau.1c00289>.
- (342) Monteiro, M. C. O.; Dattila, F.; Hagedoorn, B.; García-Muelas, R.; López, N.; Koper, M. T. M. Absence of CO₂ Electroreduction on Copper, Gold and Silver Electrodes without Metal Cations in Solution. *Nat Catal* **2021**, 4 (8), 654–662. <https://doi.org/10.1038/s41929-021-00655-5>.
- (343) Hamelin, A.; Weaver, M. J. Dependence of the Kinetics of Proton Reduction at Gold Electrodes on the Surface Crystallographic Orientation. *Journal of Electroanalytical Chemistry and Interfacial Electrochemistry* **1987**, 223 (1), 171–184. <https://doi.org/10/dghw2r>.
- (344) Brug, G. J.; Sluyters-Rehbach, M.; Sluyters, J. H.; Hemelin, A. The Kinetics of the Reduction of Protons at Polycrystalline and Monocrystalline Gold Electrodes. *Journal of Electroanalytical Chemistry and Interfacial Electrochemistry* **1984**, 181 (1), 245–266. <https://doi.org/10/fjnrzm>.
- (345) Perez, J.; Gonzalez, E. R.; Villullas, H. M. Hydrogen Evolution Reaction on Gold Single-Crystal Electrodes in Acid Solutions. *The Journal of Physical Chemistry B* **1998**, 102 (52), 10931–10935. <https://doi.org/10.1021/jp9831987>.
- (346) Dubouis, N.; Grimaud, A. The Hydrogen Evolution Reaction: From Material to Interfacial Descriptors. *Chemical Science* **2019**, 10 (40), 9165–9181. <https://doi.org/10/gg6rkp>.
- (347) Lee, S. H.; Rasaiah, J. C. Proton Transfer and the Mobilities of the H⁺ and OH[–] Ions from Studies of a Dissociating Model for Water. *The Journal of Chemical Physics* **2011**, 135 (12), 124505. <https://doi.org/10.1063/1.3632990>.
- (348) Green, D. W.; Perry, R. H. *Perry's Chemical Engineers' Handbook*, 8th ed.; McGraw Hill Professional, 2007.
- (349) Mills, R. Self-Diffusion in Normal and Heavy Water in the Range 1–45.Deg. *The Journal of Physical Chemistry* **1973**, 77 (5), 685–688. <https://doi.org/10.1021/j100624a025>.
- (350) Banerjee, P.; Bagchi, B. Ions' Motion in Water. *The Journal of Chemical Physics* **2019**, 150 (19), 190901. <https://doi.org/10.1063/1.5090765>.
- (351) Keene, R. F.; Sullivan, B. P.; Krist, K.; Guard, H. E. *Electrochemical and Electrocatalytic Reactions of Carbon Dioxide*, 1st ed.; Elsevier, 1993.

- (352) Gupta, N.; Gattrell, M.; MacDougall, B. Calculation for the Cathode Surface Concentrations in the Electrochemical Reduction of CO₂ in KHCO₃ Solutions. *Journal of Applied Electrochemistry* **2006**, *36* (2), 161–172. <https://doi.org/10.1007/s10800-005-9058-y>.
- (353) Schulz, K. G.; Riebesell, U.; Rost, B.; Thoms, S.; Zeebe, R. E. Determination of the Rate Constants for the Carbon Dioxide to Bicarbonate Inter-Conversion in PH-Buffered Seawater Systems. *Marine Chemistry* **2006**, *100* (1–2), 53–65. <https://doi.org/10.1016/j.marchem.2005.11.001>.
- (354) Critelli, R. A. J.; Bertotti, M.; Torresi, R. M. Probe Effects on Concentration Profiles in the Diffusion Layer : Computational Modeling and near-Surface PH Measurements Using Microelectrodes. *Electrochimica Acta* **2018**, *292*, 511–521. <https://doi.org/10.1016/j.electacta.2018.09.157>.
- (355) Henckel, D. A.; Counihan, M. J.; Holmes, H. E.; Chen, X.; Nwabara, U. O.; Verma, S.; Rodríguez-López, J.; Kenis, P. J. A.; Gewirth, A. A. Potential Dependence of the Local PH in a CO₂ Reduction Electrolyzer. *ACS Catal.* **2021**, *11* (1), 255–263. <https://doi.org/10/gmtzfm>.
- (356) Monteiro, M. C. O.; Mirabal, A.; Jacobse, L.; Doblhoff-Dier, K.; Barton, S. C.; Koper, M. T. M. Time-Resolved Local PH Measurements during CO₂ Reduction Using Scanning Electrochemical Microscopy: Buffering and Tip Effects. *JACS Au* **2021**, *1* (11), 1915–1924. <https://doi.org/10.1021/jacsau.1c00289>.
- (357) Weisenberger, S.; Schumpe, A. Estimation of Gas Solubilities in Salt Solutions at Temperatures from 273 K to 363 K. *AIChE Journal* **1996**, *42* (1), 298–300. <https://doi.org/10.1002/aic.690420130>.
- (358) Burdyny, T.; Graham, P. J.; Pang, Y.; Dinh, C.-T.; Liu, M.; Sargent, E. H.; Sinton, D. Nanomorphology-Enhanced Gas-Evolution Intensifies CO₂ Reduction Electrochemistry. *ACS Sustainable Chem. Eng.* **2017**, *5* (5), 4031–4040. <https://doi.org/10.1021/acssuschemeng.7b00023>.
- (359) Wuttig, A.; Yoon, Y.; Ryu, J.; Surendranath, Y. Bicarbonate Is Not a General Acid in Au-Catalyzed CO₂ Electroreduction. *J. Am. Chem. Soc.* **2017**, *139* (47), 17109–17113. <https://doi.org/10.1021/jacs.7b08345>.
- (360) Verma, S.; Lu, X.; Ma, S.; Masel, R. I.; Kenis, P. J. A. The Effect of Electrolyte Composition on the Electroreduction of CO₂ to CO on Ag Based Gas Diffusion Electrodes. *Phys. Chem. Chem. Phys.* **2016**, *18* (10), 7075–7084. <https://doi.org/10.1039/C5CP05665A>.
- (361) Sun, K.; Wu, L.; Qin, W.; Zhou, J.; Hu, Y.; Jiang, Z.; Shen, B.; Wang, Z. Enhanced Electrochemical Reduction of CO₂ to CO on Ag Electrocatalysts with Increased Unoccupied Density of States. *J. Mater. Chem. A* **2016**, *4* (32), 12616–12623. <https://doi.org/10/gmz7pb>.
- (362) Rosen, J.; Hutchings, G. S.; Lu, Q.; Rivera, S.; Zhou, Y.; Vlachos, D. G.; Jiao, F. Mechanistic Insights into the Electrochemical Reduction of CO₂ to CO on Nanostructured Ag Surfaces. *ACS Catal.* **2015**, *5* (7), 4293–4299. <https://doi.org/10.1021/acscatal.5b00840>.

- (363) Weng, L.-C.; Bell, A. T.; Weber, A. Z. Towards Membrane-Electrode Assembly Systems for CO₂ Reduction: A Modeling Study. *Energy Environ. Sci.* **2019**, *12* (6), 1950–1968. <https://doi.org/10/gf2s6w>.
- (364) Varela, A. S.; Kroschel, M.; Leonard, N. D.; Ju, W.; Steinberg, J.; Bagger, A.; Rossmeisl, J.; Strasser, P. PH Effects on the Selectivity of the Electrocatalytic CO₂ Reduction on Graphene-Embedded Fe–N–C Motifs: Bridging Concepts between Molecular Homogeneous and Solid-State Heterogeneous Catalysis. *ACS Energy Lett.* **2018**, *3* (4), 812–817. <https://doi.org/10.1021/acsenergylett.8b00273>.
- (365) Hexaamine Ruthenium (II) Chloride <https://www.colonialmetals.com/wp-content/uploads/2016/12/8013-Hexaammine-Ruthenium-II-Chloride.pdf> (accessed 2021 -11 -27).
- (366) van Deventer, J. S. J.; van der Merwe, P. F. The Effect of Temperature on the Desorption of Gold Cyanide from Activated Carbon. *Thermochimica Acta* **1993**, *221* (1), 99–113. [https://doi.org/10.1016/0040-6031\(93\)80527-H](https://doi.org/10.1016/0040-6031(93)80527-H).
- (367) Goldstein, E. L.; Van de Mark, M. R. Electrode Cleaning and Anion Effects on K₃Fe(CN)₆ couple. *Electrochimica Acta* **1982**, *27* (8), 1079–1085. [https://doi.org/10.1016/0013-4686\(82\)80113-8](https://doi.org/10.1016/0013-4686(82)80113-8).
- (368) Sun, T.; Blanchard, P. Y.; Mirkin, M. V. Cleaning Nanoelectrodes with Air Plasma. *Analytical Chemistry* **2015**, *87* (8), 4092–4095. <https://doi.org/10.1021/acs.analchem.5b00488>.
- (369) Ward, M. D.; White, J. R.; Bard, A. J. Electrochemical Investigation of the Energetics of Particulate Titanium Dioxide Photocatalysts. The Methyl Viologen-Acetate System. *J. Am. Chem. Soc.* **1983**, *105* (1), 27–31. <https://doi.org/10.1021/ja00339a007>.
- (370) Zoski, C. G. Nanoscale Scanning Electrochemical Microscopy: Emerging Advances in Applications and Theory. *Current Opinion in Electrochemistry* **2017**, *1* (1). <https://doi.org/10.1016/j.coelec.2017.01.002>.
- (371) Yu, Y.; Sun, T.; Mirkin, M. V. Toward More Reliable Measurements of Electron-Transfer Kinetics at Nanoelectrodes: Next Approximation. *Analytical Chemistry* **2016**, *88* (23). <https://doi.org/10.1021/acs.analchem.6b03392>.